8-2016

Actinium-225 Production via Proton Irradiation of Thorium-232

Justin Reed Griswold
University of Tennessee, Knoxville, jgriswo1@vols.utk.edu

To the Graduate Council:

I am submitting herewith a dissertation written by Justin Reed Griswold entitled "Actinium-225 Production via Proton Irradiation of Thorium-232." I have examined the final electronic copy of this dissertation for form and content and recommend that it be accepted in partial fulfillment of the requirements for the degree of Doctor of Philosophy, with a major in Nuclear Engineering.

Lawrence Heilbronn, Major Professor

We have read this dissertation and recommend its acceptance:

Saed Mirzadeh, Howard L. Hall, Laurence F. Miller, Robert M. Counce

Accepted for the Council:

Carolyn R. Hodges

Vice Provost and Dean of the Graduate School

(Original signatures are on file with official student records.)

Actinium-225 Production via
Proton Irradiation of Thorium-232

A Dissertation Presented for the
Doctor of Philosophy
Degree
The University of Tennessee, Knoxville

Justin Reed Griswold
August 2016

Abstract

High energy proton spallation reactions on natural thorium metal targets have been utilized to produce multi mCi [milliCurie] quantities of Actinium-225. Theoretical cross sections for actinium and thorium isotopes as well as for a select number of the fission products produced in these reactions were generated by the Monte Carlo radiation transport code PHITS to simulate the experimental data obtained from sixteen irradiations of thorium metal targets with 25-210 µA [microampere] proton beams ranging in energies from 77 to 192 MeV. Irradiations were conducted at Brookhaven National Laboratory (BNL) and Los Alamos National Laboratory (LANL), while target dissolution and processing was carried out at Oak Ridge National Laboratory (ORNL). At ORNL, a series of ion exchange columns was employed to isolate actinium from dissolved thorium, protactinium, radium, and numerous fission products. PHITS simulated cross sections for the production of Actinium-225 range from 7.8 to 28.2 mb [millibarn] in the incident proton energy range of 77 to 192 MeV [mega-electron volt]. The experimental cumulative cross sections for Actinium-225 are less than the simulated values by approximately a factor of two and vary from 3.6 to 16.7 mb over the same energy range. Based on these data, production of curie quantities of Actinium-225 is possible by irradiating ~80 grams of Thorium-232 target (5.0 g cm^{-2} [grams per square centimeter]) for 10 days at either BNL or LANL proton irradiation facilities. Thorough analysis of two Actinium-225/Bismuth-213 generators produced by this process and used by nuclear medicine researchers was performed. It was demonstrated that the generators are free of any long-lived radiocontaminants with the exception of the known contaminant Actinium-227 and its decay products.

Table of Contents

List of Tables

List of Figures

1 Introduction

1.1 Scope

In this work, the effective cross section and yield measurements for large-scale production of ^{225}Ac through the high-energy proton bombardment of ^{232}Th are reported. Also reported are the cross sections for several other radioisotopes including: ^{226}Ac, ^{227}Ac, ^{227}Th, ^{228}Th, ^{99}Mo, ^{140}Ba, ^{139}Ce, ^{141}Ce, ^{143}Ce, and ^{144}Ce. Measurement of yield of the other actinium isotopes relative to ^{225}Ac is crucial since the coproduced actinium isotopes cannot be chemically separated and, hence, they constitute major impurities. The effective cross sections and yields of the other radioisotopes are included due to their effect on chemical processing and purity of the ^{225}Ac product, among the most important are isotopes of lanthanum (^{140}Ba decays to ^{140}La) and cerium due to their very close chemical resemblance to actinium. The finer details of the chemical isolation of actinium from fission products and actinides coproduced in the high-energy proton irradiation of natural thorium are beyond the scope of this document.

When referring to the experimental cross sections measured in this work, the term "effective cross section" will be used to reflect the following: (a) in 77-192 MeV proton energy range, there may be a number of nuclear pathways to a specific radionuclide; (b) the targets used in these studies are not considered "thin" targets, and consequently some loss of proton energy occurred in the target; (c) in a few instances, the irradiation time was much longer than the half-life of the radionuclide; (d) burn-up of the target, due to long irradiation time and high proton intensity. General notation of type ^{232}Th[p,x]^{225}Ac was used to highlight the multiple reaction pathways; in this specific case, ^{232}Th[p,α4n]^{225}Ac and ^{232}Th[p,αp3n]^{225}Ra(β-, 14.9 d)→^{225}Ac. From this point forward, the term "measured cross section" or "experimental cross section" refers to the

"effective cross section." It is also important to note that the term "simulated cross section" will refer to any cross section calculated using the PHITS Monte Carlo code system described in Section 2.4.

The determination of any unknown long-lived contaminants of ^{225}Ac/^{213}Bi generators produced through the high-energy proton irradiation of ^{232}Th is also a focus of this dissertation. From the early stages of this project, it has always been well known that one of the main impurities of accelerator produced ^{225}Ac would be the long-lived ^{227}Ac. However, it is crucial to determine if any other impurities, specifically elements other than actinium, bypass the chemical separation process and reach the ^{225}Ac/^{213}Bi generator stage.

1.2   Direct Contribution to Tri-lab Initiative to Produce ^{225}Ac

My contribution to this project was collecting, analyzing, and summarizing all of the nuclear data involved with the tri-lab initiative to produce ^{225}Ac. I used this data to calculate the effective cross sections for various radionuclides in each irradiation. This information was then shared with the rest of the team to plan for the next experiment by modifying parameters such as irradiation times, incident proton energy, and target mass. I used gamma-ray spectroscopy exclusively for analysis of the samples, and analyzed approximately 20 samples per irradiation. My responsibility also included maintaining, calibrating, and measuring the absolute efficiency curves for the three high purity germanium gamma ray detector systems used in these studies. Further, I used the Monte Carlo simulation code PHITS to predict the same excitation functions in support of the experimental data. Finally, through ion exchange chromatography and subsequent gamma-ray spectroscopy, I analyzed decayed ^{225}Ac/^{213}Bi generators to qualify the presence of any unknown radiocontaminants in the accelerator-produced ^{225}Ac.

In summary, I reported the experimental excitation functions of eleven nuclear reactions at seven independent proton energies in this project. I am the first author of a manuscript accepted by *Applied Radiation and Isotopes* that summarizes the experimental aspects of the research described in this thesis.

1.3 Targeted-Alpha Radioimmunotherapy with Actinium-225

The scientific community has produced many new diagnostic and therapeutic applications for the field of nuclear medicine over the last few decades. Of these therapeutic applications, targeted alpha radioimmunotherapy (targeted alpha therapy or TAT), is one of the most promising and effective new methods of treating various forms of oncologic diseases [1]. This technique involves transporting select alpha-emitting radionuclides to cancerous sites within the body. The high linear energy transfer (~100 keV/µm) of alpha particles in human tissue can induce double strand breaks in DNA and ultimately cell death. In addition, the short range of alpha particles (<100 µm) limits damage to nearby healthy cells while maximizing damage to local cancerous tissue [2].

Several different delivery vectors for alpha-emitting radionuclides have been studied including biological carriers such as engineered peptides or monoclonal antibodies that selectively seek out cancerous tissue [3, 4]. Based on their chemical properties, some radionuclides can be systematically targeted to specific tumor sites without attachment to biological carriers. Radium-223 ($t_{1/2}$ = 11.43d) treatment of bone metastases serves as a good example of systematic biological targeting [5].

A few alpha emitting radioisotopes identified as possible candidates for targeted alpha therapy include ^{149}Tb ($t_{1/2}$ = 4.12h), ^{211}At ($t_{1/2}$ = 7.21h), ^{212}Bi ($t_{1/2}$ = 60.55m), ^{212}Pb ($t_{1/2}$ =

10.64h), ^{213}Bi ($t_{1/2} = 45.59$m), ^{225}Ac ($t_{1/2} = 9.92$d), and ^{227}Th ($t_{1/2} = 18.68$d) [6]. Due to the ratio of their half-lives, pairs of radionuclides such as ^{212}Pb/^{212}Bi and ^{225}Ac/^{213}Bi can be used in a generator mode, where the longer-lived parent isotope is loaded on an ion exchange column and the daughter isotope is allowed to grow in. This approach allows for multiple elutions of the daughter isotope at the point of administration. Results of clinical trials with ^{213}Bi eluted from a generator have shown progress in treating several different types of malignant diseases including acute myeloid leukemia [7].

In addition to the generator mode, there have been some investigations into the direct *in vivo* administration of ^{225}Ac itself [8]. In theory, the four α-emission decay chain of ^{225}Ac can deliver up to 1000 times the integrated dose of an equivalent quantity of ^{213}Bi, which only decays with a single α-emission [9]. Despite the certain complications associated with the decay products leaving the tumor volume and damaging healthy tissue, this mode of therapy utilizing ^{225}Ac remains attractive due to its potency. There is a continuous effort to develop approaches designed to overcome this issue [4, 10]. Whether used via the direct application or as a generator for ^{213}Bi, the efficacy in early clinical trials has greatly increased the demand for ^{225}Ac.

Currently, the most common method of generating ^{225}Ac for clinical studies is through the decay of the long-lived ^{229}Th ($t_{1/2} = 7880$ y). Using this technique, ^{225}Ac and its direct parent ^{225}Ra ($t_{1/2} = 14.9$d) are routinely "milked" from the "cow" (^{229}Th) every few weeks. Three main sources of ^{229}Th worldwide are large enough to produce relevant quantities of ^{225}Ac. Each of these sources has been chemically separated from the fissile precursor ^{233}U, whose decay chain is shown in Figure 1. Since 1997, Oak Ridge National Lab (ORNL) has been supplying up to 720 mCi per year of high purity ^{225}Ac. A similar quantity is available from the Institute of Physics and Power Engineering IPPE, in Obninsk, Russia. The Institute for Transuranium Elements

4
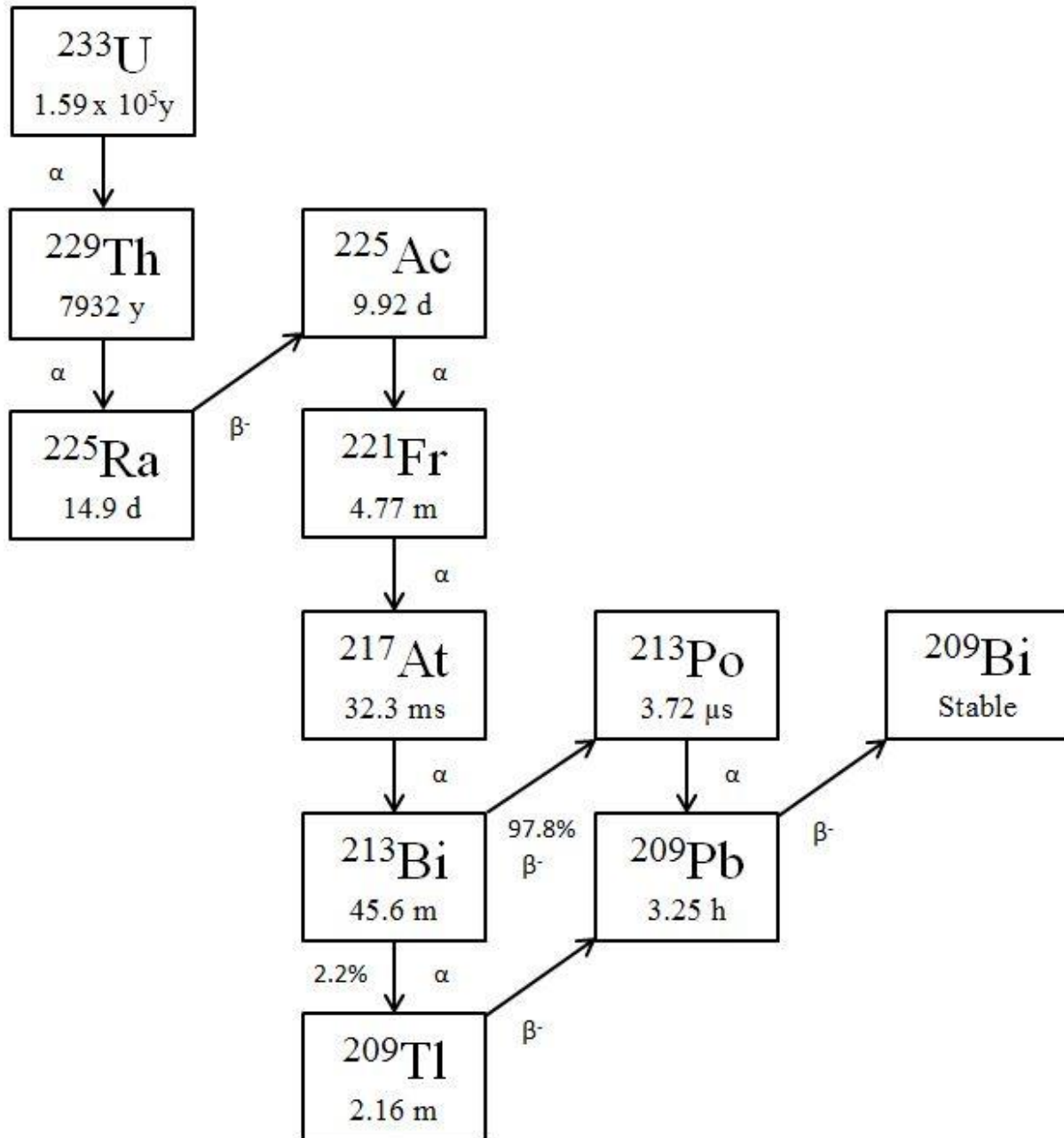
Figure 1. Uranium-233 Decay Chain.

(ITU) in Karlsruhe, Germany maintains a smaller ^{229}Th source that is capable of producing up to 350 mCi of ^{225}Ac per year [11].

Studies have been conducted to investigate different means of increasing the available supply of either the ^{229}Th parent or ^{225}Ac itself. Producing relevant quantities of ^{229}Th is challenging due to its extremely long half-life. Cross section measurements for the ^{232}Th[p,4n]^{229}Pa reaction at proton energies below 40 MeV have shown that dedicated accelerator production of ^{229}Th is currently not viable due to long irradiation times and high currents required to produce a substantial activity of ^{229}Th [12]. A substantial ^{229}Th source could be generated if ^{232}Th were used as a beam stop for several years at any high-current proton accelerator facility. Reactor production of ^{229}Th is possible through the neutron irradiation of ^{226}Ra ($t_{1/2}$ = 1600y), but almost one thousand times more ^{228}Th ($t_{1/2}$ = 697.15d) activity is produced due to the shorter half-life and one less neutron capture [13]. Similar to accelerator production of ^{229}Th, a long irradiation time is necessary to produce useful quantities of ^{229}Th in a reactor [14]. Proton irradiation of ^{226}Ra targets has been carried out at ITU resulting in cross section data for the ^{226}Ra[p,2n]^{225}Ac reaction for the energy range of 8.8 to 24.8 MeV, with a maximum cross section of 710 mb at 16.8 MeV [15]. A feasibility study of the ^{226}Ra[γ,n]^{225}Ra reaction for producing the ^{225}Ra, the parent to ^{225}Ac, has revealed that ^{225}Ra yields are insufficient for practical use [16].

Instead of producing a larger quantity of ^{229}Th and allowing it to decay to ^{225}Ac, ^{225}Ac can be produced directly via high-energy proton (~70-200 MeV) spallation of ^{232}Th. Our studies have shown that it is possible to produce up to Curie quantities of ^{225}Ac using protons in the energy range of 70-200 MeV and in the intensity range of 100 to 250 μA. Up to this point, the highest yield produced using this technique is about 150 mCi of ^{225}Ac at the end of

bombardment. Sixteen irradiations have been conducted in a joint effort of Brookhaven National Lab (BNL), Los Alamos National Lab (LANL), and Oak Ridge National Lab (ORNL). The natural thorium foil targets are irradiated at either the Brookhaven Linac Isotope Producer (BLIP) or the Los Alamos Isotope Production Facility (IPF). Post-irradiation, the targets are shipped to ORNL for chemical processing within a hot cell. Depending on the total activity at end of bombardment, sometimes the targets are allowed to decay for several days before shipping in to limit radiation dose to workers.

1.4   Nuclear Physics Discussion

Nuclear transmutation reactions can either absorb or release energy depending on the difference in mass of the products and the reactants. The energy that is released or absorbed is frequently referred to as the Q value of the reaction, and is calculated by subtracting the mass of the products from the mass of the reactants (typically with the units of MeV). A positive Q value refers to a nuclear reaction that releases excess energy while a negative Q value refers to a nuclear reaction that requires a minimum incident particle kinetic energy. The minimum energy that is required for a nuclear reaction to occur is called the threshold energy. Threshold energy for proton-induced nuclear reactions can be approximated using Equation 1 below where Q is the Q value, M_p is mass of a proton, and M_T is mass of the target nucleus:

$$E_t = Q \left(\frac{M_p + M_T}{M_T} \right) \qquad \qquad \textit{Equation 1.}$$

It is important to note, that as the mass of the target nucleus increases, $E_T \approx Q$.

For charged particles, it is necessary to consider the Coulomb repulsion of the charged particles in the nucleus upon the incident particle, referred to as the Coulomb Barrier. The

Coulomb Barrier for a charged particle reaction is calculated using Equation 2 where Z_a is the number of protons in the incident particle, Z_A is the number of protons in the target nucleus, e is the charge of a proton in coulombs, and R is the radius of the target nucleus:

$$V_c = \frac{Z_a Z_A e^2}{R}$$
Equation 2.

The radius of the nucleus (in meters) can be estimated using Equation 3, where A is the atomic number.

$$R = 1.2 \ x \ 10^{-15} A^{1/3}$$
Equation 3.

At higher energies, the Coulomb Barrier is much more significant for particles exiting the nucleus in nuclear reactions than particles incident upon the target nucleus. As Z of the target nucleus increases, neutron emission becomes favorable over charged particle emission.

The term nuclear cross section refers to the probability of a nuclear process occurring and is usually given in the units of cm^2 or barns (b), where one barn is equal to $1 \ x \ 10^{-24} \ cm^2$. Expressing cross sections in the dimensions of an area originates from the simple concept that the probability for the reaction between a target nucleus and an incident particle is proportional to the cross-sectional target area presented by the target nucleus. Of course this is a generalization and true reaction cross sections are dependent on many other factors. One of these factors is incident particle energy and the relationship between cross section and incident particle energy for a specific reaction is often referred to as an excitation function. The shape of the excitation function for each reaction is dependent on a number of aspects including but not limited to reaction pathway and nuclear structure.

Several models are used to describe and predict nuclear reactions and nuclear reaction cross sections. The optical model, the compound nucleus model, and the direct interaction model will all be briefly discussed, with the direct-interaction model being the most relevant for this work involving high-energy proton cross sections. Each of these models has strengths and weaknesses, and each requires that certain assumptions be incorporated in order for the model to be valid. Depending on the incident particle energy, it is often useful to combine two or more of these models to predict the behavior of certain nuclear interactions accurately. The earliest of the models listed above, the optical model simplified the interactions of the incident particle with the nucleons of a target nucleus by instead visualizing an incident particle reacting with a potential energy well. This model is effective in determining elastic scattering and total reaction cross sections, but is unable to predict the probability of specific reactions occurring after an incident particle has been absorbed in the target nucleus.

Introduced by Niels Bohr in 1936, the compound-nucleus model involves two distinct phases: the formation of a compound nucleus and the evaporation of particles from the excited compound nucleus. According to this model, a compound nucleus is formed when an incident particle is absorbed by a target nucleus. The kinetic energy of the incident particle is shared randomly with the other nucleons within the compound nucleus. The excitation energy of the excited nucleus is given in Equation 4 below where M_A is the atomic mass of the target, M_a is the atomic mass of the incident particle, T_a is the kinetic energy of the incident particle, and S_a is the binding energy of the incident particle in the compound nucleus:

$$U = \frac{M_A}{M_A + M_a} T_a + S_a \qquad\qquad \textit{Equation 4.}$$

9

The compound-nucleus model assumes that if a compound nucleus can be produced through more than one reaction channel, its decay, or evaporation, into reaction products is independent of its formation pathway. This assumption has been confirmed through many experiments, the first of which was performed by S. N. Ghoshal in 1950. The term evaporation is used due to the similarities between this process and the emission of hot molecules from a hot liquid. Reaction products emitted from the nucleus in this manner are much lower in energy than the incident particle and are emitted isotropically. Ghoshal discovered that the various excitation functions for the production and instantaneous decay of the ^{64}Zn compound nucleus were the same whether produced through the ^{63}Cu[p,xn]Zn reaction or the ^{60}Ni[α,xn]Zn reaction [17]. Although it is somewhat accurate for lower-energy charged particle and neutron interactions, the compound-nucleus model by itself is largely ineffective for incident particle energies greater than 20 MeV. However, the evaporation step of this model is combined with a portion of the direct-interaction model to form the intranuclear cascade/evaporation model that is highly effective in the 100-2000 MeV incident particle energy region.

The direct-interaction model is a more useful model for higher-energy nuclear reactions. Unlike the compound-nucleus model, it does not assume that an incident particle distributes its energy randomly among all nucleons within the target nucleus. Instead, it is assumed that the incident particle strikes one or a small number of nucleons within the target nucleus directly and ejects them. In this process, the ejected particles are expected have a much higher kinetic energy than those that are evaporated from a compound nucleus event. Specific direct interaction events such as stripping and pickup reactions can occur where only a portion of incident particles interact with nucleons in the target nucleus. These types of interactions are significant, especially when considering heavy-ion interactions with matter [18].

Nuclear interactions referred to as spallation are usually described with a model that is similar to a combination of the compound nucleus and the direct interaction models. Although this type of nuclear reaction occurs within a fraction of a second, it can be described as a two-step process. In the first step, the incident particle reacts with nucleons within the target nucleus. This creates an intranuclear cascade of high energy (>20 MeV) nucleons that can escape as secondary particles if their kinetic energy is large enough. Other excited nucleons deposit their kinetic energy within the target nucleus, promoting it to an excited state. This leads to the second step of the spallation process, the nuclear de-excitation referred to as evaporation where lower energy (<20 MeV) neutrons, protons, alpha particles, and sometimes even larger nuclei are emitted from the nucleus. In the evaporation process, the majority of the emitted particles are neutrons [19].

1.5   Gamma-Ray Spectroscopy

Semiconductors have proven to be extremely useful in the field of radiation detection. As shown in Figure 2, the small energy bandgap between the conduction band and the valence band for semiconductors allows for charged particles traversing the semiconductor medium to promote electrons to the conduction band through Coulomb effects. Semiconductors are usually defined as having a bandgap energy of around 1eV. When a bias voltage is applied to the semiconductor, the promoted electrons can be collected. The collected charge is proportional to the energy of the incident charged particle. In the case of neutral radiation such neutrons or protons, the secondary charged particles produced by nuclear reactions within the semiconductor medium are able to excite electrons to the conduction band where they are collected by an applied bias voltage.
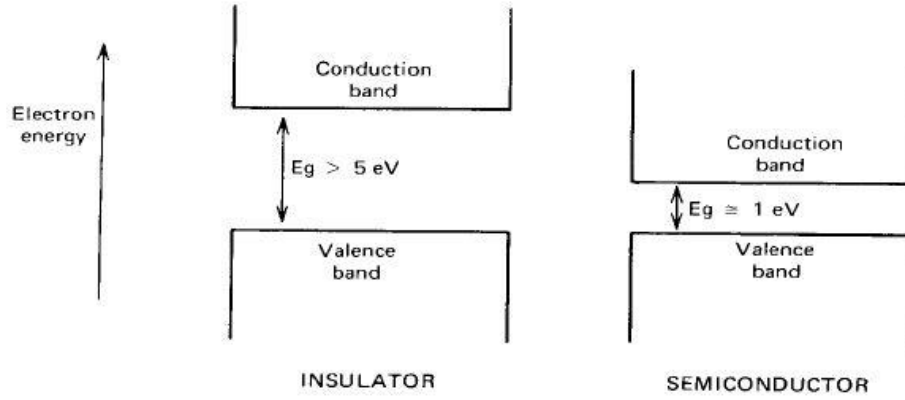
Figure 2. Bandgap energy of insulator and semiconductor [20].

High purity germanium semiconductor detectors (HPGE) are considered the gold standard in semiconductor detection of γ-rays. The energy resolution of these detectors at 1-2 keV is an order of magnitude better than the resolution of scintillation detectors like sodium iodide. However, sodium iodide detectors are more efficient than HPGe detectors. Further, it is possible for electrons within an HPGe crystal to be excited to the conduction band by thermal energy. The probability of such an event occurring is given in Equation 5 where T is absolute temperature in Kelvin, E_g is the bandgap energy, k is the Boltzmann constant, and C is the proportionality constant of the material.

$$p(T) = CT^{3/2}e^{-\frac{E_g}{2kT}}$$
  Equation 5.

In order to combat this effect, liquid nitrogen is used to cool the HPGe crystal during operation.

HPGe detectors can have either planar or coaxial geometry. Coaxial detectors are usually favored for γ-ray spectroscopy due to the larger volume of crystal. In a coaxial detector, the core of the crystal is removed and an electrical contact is placed over the inner cylindrical surface.

12

Another electrode is placed on the outer surface of the coaxial detector. The germanium crystals can be made to have substantial length in the axial direction. This can allow for detector volumes of up to 800 cm^3 be produced. Since coaxial detectors have a smaller inner diameter than planar detectors, they can be created with a lower capacitance [20].

2 Materials and Methods

2.1 Target Irradiations

In this work, sixteen irradiations were carried out over a span of two years. Three irradiations were performed at the Isotope Production Facility (IPF) at Los Alamos National Lab (LANL) and thirteen irradiations were performed at the Brookhaven Linac Isotope Producer (BLIP) at Brookhaven National Lab (BNL). Irradiation parameters such as incident proton energy, irradiation period, and target thickness were adjusted to meet the specific goals of each experiment. The parameters for each irradiation at BLIP and LANL are summarized in Table 1. Overnight irradiations were designed to measure cross sections for the short-lived impurities such as ^{226}Ac ($t_{1/2}$ = 29.37 h) and ^{143}Ce ($t_{1/2}$ = 33.04 h). Longer irradiations were carried out to achieve three primary objectives: (a) to produce useful quantities of ^{225}Ac for evaluation in nuclear medicine applications, (b) to develop the remote chemical process adaptable to large-scale production of ^{225}Ac, and (c) to resolve the often-challenging logistical issues associated with the shipment of highly radioactive targets containing alpha emitting radionuclides.

Table 1. Irradiation Parameters. Irradiations 1-3 occurred at IPF and 4-16 occurred at BLIP.

Number	Target Thickness (mg cm^{-2})	Energy (MeV)	Irradiation Period (h)	Average Current (µA)
1	637.6	76.5	24.2	207.1
2	637.6	89.9	24.1	208.3
3	585.0	89.9	91.5	159.5
4	166.0	127.8	3.6	87.2
5	519.5	127.8	17.0	54.1
6	157.4	127.8	107.4	45.1
*7a	164.5	127.8	137.6	36.6
*7b	168.5	127.8	137.6	36.6
8	366.3	127.8	190.3	50.8
9	146.3	127.8	16.0	23.6
10	146.3	152.5	16.0	30.7
11	146.3	173.6	16.0	29.9
12	592.8	191.7	218.2	108.5
13	579.2	191.7	222.0	116.4
14	438.8	191.7	215.3	93.1
15	146.3	192.1	16.8	65.2
16	527.2	191.7	191.4	86.0

*Targets 7a and 7b consisted of two thorium foils that were irradiated together but processed separately.

2.1.1 Irradiations at LANL-IPF

IPF is one of five primary facilities that combine to make up the Los Alamos Neutron Science Center (LANSCE). LANSCE is capable of simultaneously accelerating H+ or H- ions up to 800 MeV for a variety of applications (Figure 3). Initially, protons are generated at LANSCE by a duoplasmatron ion source and accelerated with a Cockroft-Walton generator to 750 keV. From there, proton beams are focused and bunched through a low-energy beam transport area before reaching the first section of the linac. The first section of the linac is considered a drift tube linac based on the design by Alvarez from 1946 [21]. An average proton beam current of up to 250 μA exits the drift tube linac at 100 MeV where and enters a transition region. As shown in Figure 4, a kicker magnet located within the transition region extracts a portion of the 100 MeV protons and bends them towards the IPF beam line. The remaining protons continue into a side-coupled cavity linac where they are accelerated to 800 MeV for use in the other LANSCE research facilities [22].
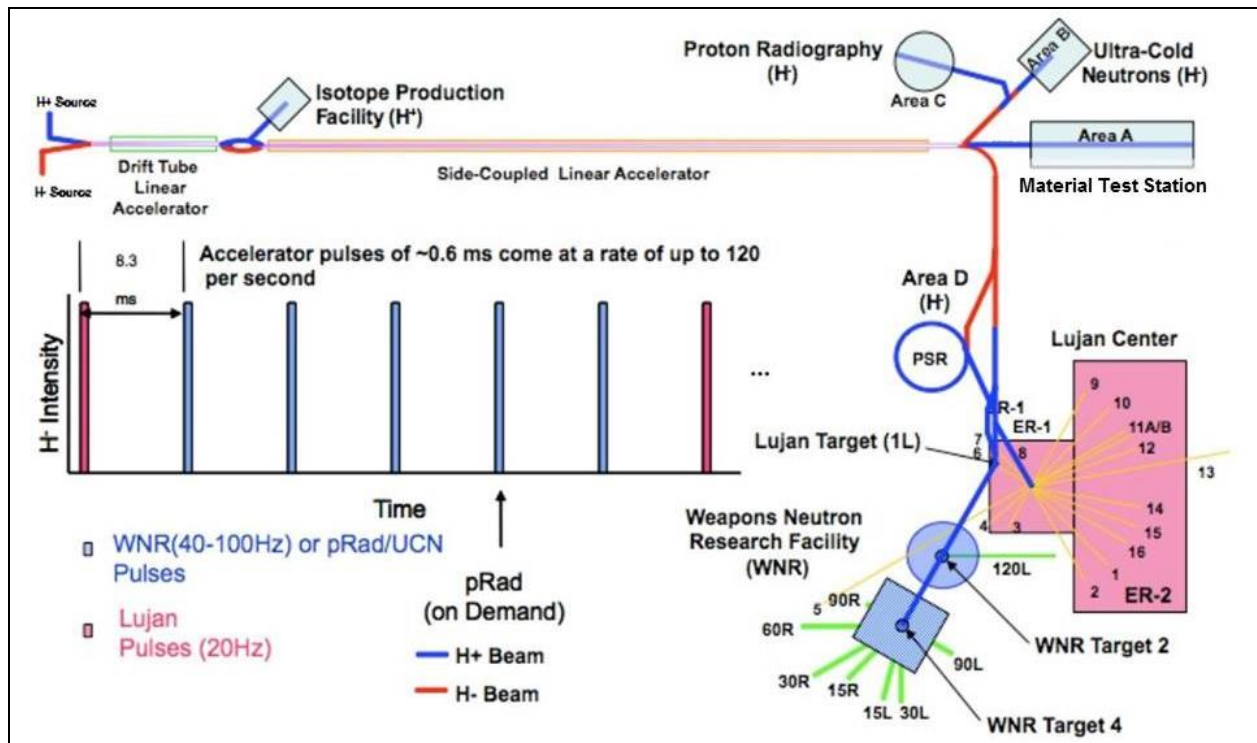
Figure 3. Schematic of LANSCE.
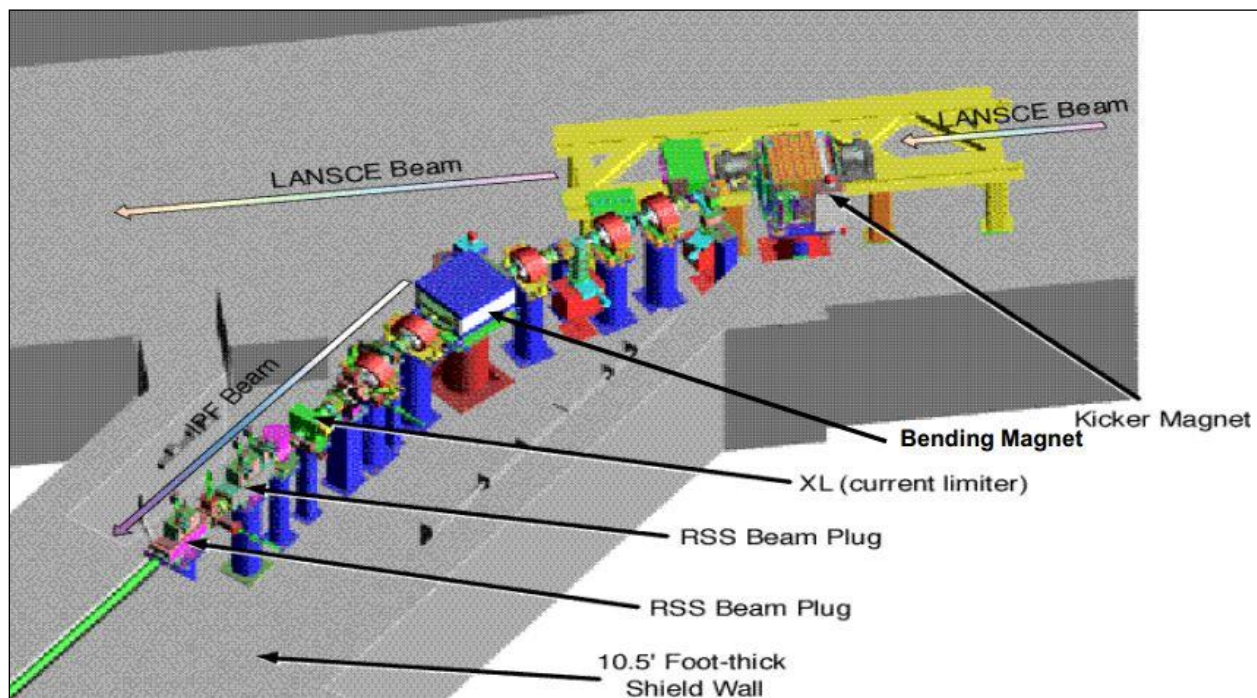
Figure 4. Diagram of IPF where the kicker magnet bends the LANSCE proton beam towards the IPF target station.

Targets irradiated at IPF were composed of arc-melted thorium metal that was rolled to the thickness of the finished target and trimmed to its final dimensions. X-ray fluorescence spectroscopy of the thorium stock confirmed a composition ≥ 99.6%. These thorium discs were electron-beam welded into machined Inconel capsules (Figure 5). During irradiations at IPF, instantaneous beam intensities were monitored and logged at one and ten second intervals by two inductive current monitors. In the past, recorded beam histories have been compared with integrated fluences measured by established monitor reactions [23] and found to be accurate within 5%.
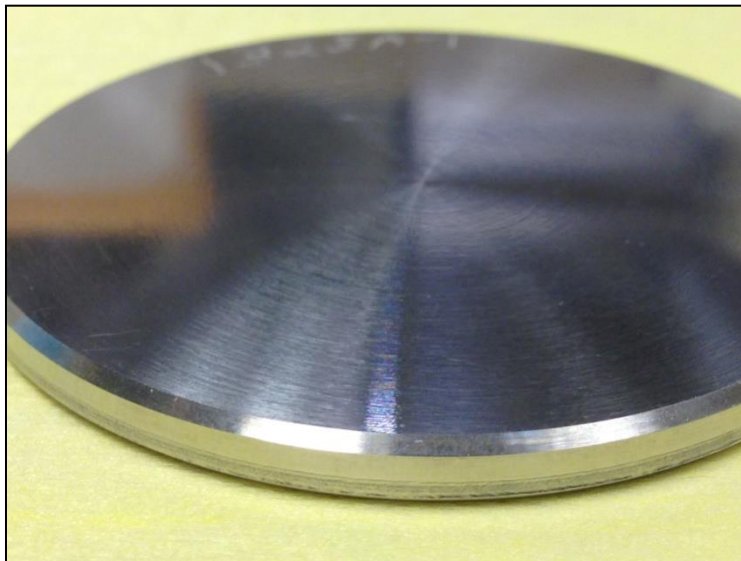
Figure 5. Inconel-encapsulated thorium disk before irradiation at IPF.

After irradiation, targets were allowed to decay at IPF to U.S. Department of Transportation (DOT) Type A quantities and then moved to the processing facility where the Inconel encapsulation was cut open. The irradiated thorium was then removed from the Inconel cladding, repackaged in a glass vial, and shipped to ORNL for chemical processing.

2.1.2   Irradiations at BNL-BLIP

As shown in Figure 6, BLIP is part of a system accelerators referred to as the BNL

Accelerator Complex that is involved in a variety of high-energy physics research applications.

Similar to IPF, the preinjector system at BLIP begins with a duoplasmatron ion source and a 750

keV Cockroft-Walton generator. From there, protons are transported the 8 m distance to the linac

via the Low Energy Beam Transport system. After being accelerated up to 200 MeV, a portion of

the proton beam is bent by three magnets a total of 30° towards the BLIP target station [24].
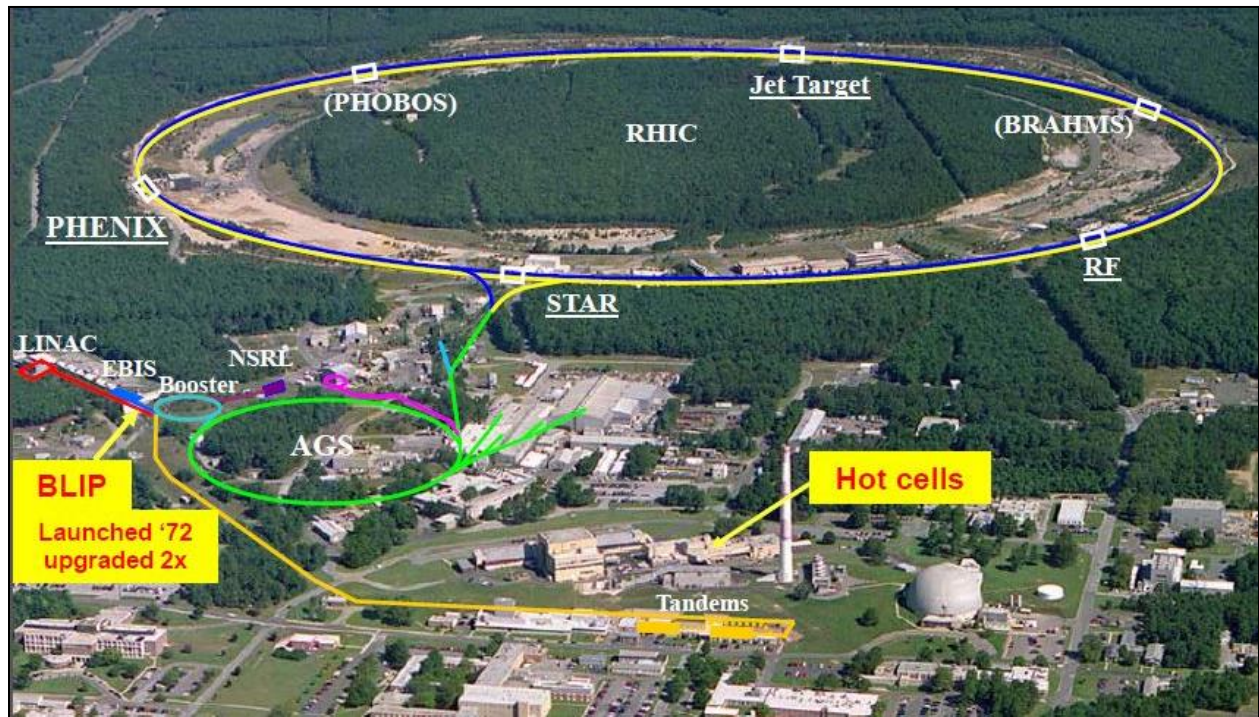
Figure 6. BNL Accelerator Complex.

BLIP is capable of accelerating 115 µA proton beams up to 200 MeV in a Gaussian

geometry. The maximum current is controlled by an administrative limit that allows for proper

target cooling to avoid target failure or melting. By definition, a Gaussian beam profile

concentrates accelerated protons in the center of a radial distribution with a decreasing current

density with increasing radial distance from the center of the beam. In a recent upgrade to BLIP, a raster system was installed to increase the maximum average current to 150 μA while improving the uniformity of the current density. However, all of the irradiations performed at BLIP for this study employed a Gaussian beam profile like the one shown in Figure 7.
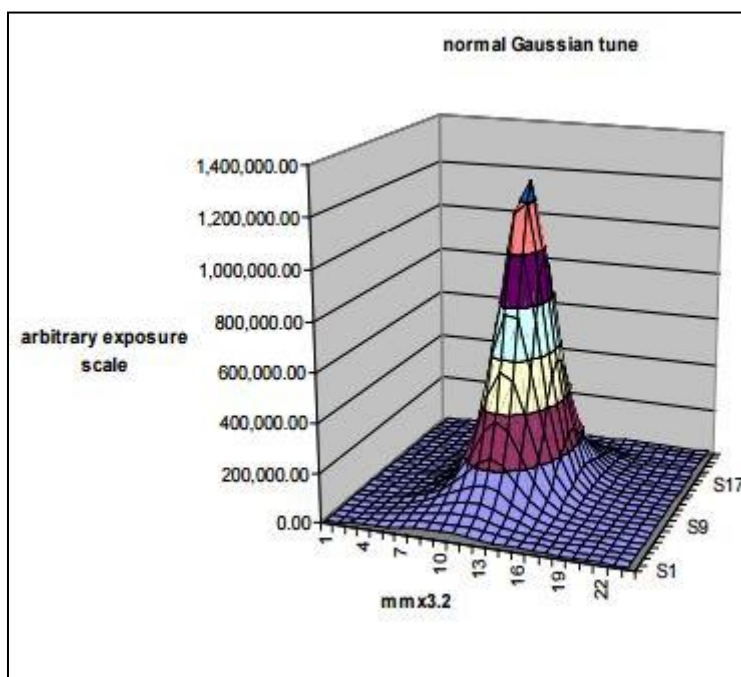
Figure 7. Typical Gaussian beam profile recorded at BLIP. The x and y axes are in mm and the z-axis in arbitrary units of exposure to compare the relative spatial proton current.

For the irradiations at BLIP, thorium foils (0.125 mm, 99.5% purity) were purchased from Goodfellow Corporation (Coraopolis, Penn., USA). For a typical irradiation, a ~27.9 mm circle was cut from the foil and wrapped in 0.025 mm Al metal foil to prevent contamination spread during target opening and packaging for shipment. A single foil was irradiated in the shorter irradiations while three sandwiched foils were irradiated in the longer ones. The beam current was monitored using 0.127 mm Al foil (99.99%, Atlantic Metals and Alloys, LLC) whose area mimicked that of the thorium foils. Since BLIP targets are cooled by water, in all experiments the foils and Al monitor foil were isolated in a bolted aluminum target capsule described

20

previously [25]. The well of the target capsule was machined to the size of the thorium and aluminum foil stack to ensure close fit for good thermal conductivity (Figure 8, Figure 9). After irradiation, the aluminum monitor foil was dissolved in a mixture of HCl and HNO_3, and the resulting solution was assayed for ^{22}Na ($t_{1/2}$ = 2.6 y) using γ-ray spectroscopy. Finally, beam current was determined using cross section data from Steyn et al. [26].
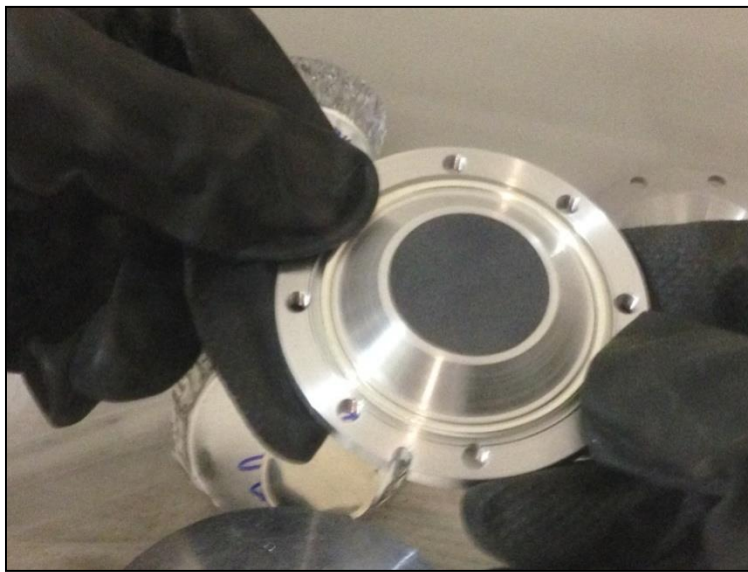
Figure 8. Aluminum target holder with thorium disk before irradiation at BLIP.

Before shipment of the more radioactive targets, each target was allowed to decay for seven days to reduce the dose and radioimpurities to levels that met transportation and radiological facility requirements. The foils were packaged and shipped individually in DOT Type A containers.

2.1.3 TRIM Calculations

Incident proton energy for each irradiation and target package geometry was determined using the computer code TRIM (transport of ions in matter). TRIM is a Monte Carlo based code

that follows a user-specified (usually very large) number of particle histories in a user-created

target. As implied by the name, TRIM only models the transport of heavy charged particles and

is not applicable to the transport of γ-rays, electrons, positrons, or neutrons. Particle energy is

lost through nuclear or electronic collisions, and the particle history ends when the particle

reaches a minimum energy or is scattered outside of the target. The applicable range of ion

energies is from 0.1 keV/u to "several" MeV/u [27]. When compared to other programs utilizing

the Monte Carlo technique, one of the main advantages TRIM provides is the ability to cut down

computing time by up to 50 times over other programs. However, with this increased speed,

some assumptions must be made such as neglecting nuclear reactions, relativistic effects, and

directional properties of the crystal lattice of the target material.
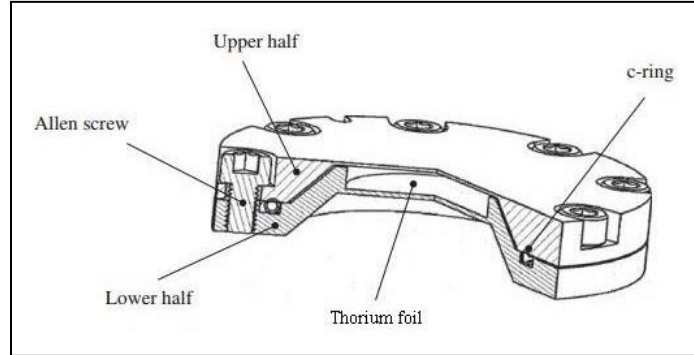
Figure 9. Aluminum target holder used for thorium irradiations at BLIP.

The results of the TRIM calculation for the six different energy single foil irradiations and

the 192 MeV three-foil irradiations are shown in Table 2 and Table 3 respectively. A nominal

10,000 incident protons were used for each simulation to limit computation time. For good

measure, one simulation was performed with 100,000 incident protons and resulted in a similar

value for uncertainty. In this case the uncertainty values are dependent not on number of incident

particles simulated but largely upon range straggling effects. Fractional tabulated uncertainties

are simply the standard deviation divided by the mean proton energy as shown in Equation 6

below.

$$\sqrt{\frac{\sum(E_i-\bar{E})^2}{n-1}}$$
Equation 6.

Table 2. TRIM calculated energies for single foil irradiations at BLIP and IPF.

Incident (MeV)	Exit (MeV)	Average (MeV)	Uncertainty (%)	Uncertainty (MeV)
77.7	75.3	76.5	1.0	0.8
91.0	88.8	89.9	0.5	0.4
128.0	127.6	127.8	0.4	0.5
152.7	152.3	152.5	0.3	0.5
173.8	173.4	173.6	0.3	0.5
192.2	191.9	192.1	0.2	0.5

Table 3. TRIM calculated energies for three foil irradiations at BLIP.

Incident (MeV)	Exit (MeV)	Average (MeV)	Uncertainty (%)	Uncertainty (MeV)
191.5	191.2	191.4	0.3	0.5
191.9	191.6	191.7	0.3	0.5
192.2	191.9	192.1	0.2	0.5

2.2   Target Dissolution and Processing at ORNL

After arrival at ORNL, the targets were transferred into a hot cell for remote processing. The

radiation dose measured on contact with the target foils was usually greater than 60 mSv/h (6

rem/hr). Each foil was dissolved in 10 M optima grade HCl with a few drops of 2 M HF. Gentle

23

heating was applied to aid the dissolution. After dissolution, the supernatant solution was separated from residual solids by decantation, and a 50 µL aliquot was taken from each dissolved sample and diluted to $5–10 \times 10^4$ times to reduce the sample activity enough for γ-ray spectroscopy analysis. Activities of all radioisotopes reported in this work except for ^{227}Ac ($t_{1/2} = 21.77$ y) were determined from this target solution aliquot.

Since ^{227}Ac does not emit abundant γ-rays, its activity was determined by measuring the activity of its daughter, ^{227}Th, after it reached secular equilibrium with ^{227}Ac. Two approaches were used: In the first approach, an aliquot of target solution was allowed to decay for at least 180 days and then it was assayed for ^{227}Th. The second approach was used in later experiments as it facilitated faster results; the Ac fraction was chemically separated from thorium and ^{227}Th was then allowed to grow in the purified ^{227}Ac fraction. The resulting ^{227}Ac activity was corrected taking into account chemical yield of the actinium fraction that was monitored through the detection of ^{225}Ac.

Ion exchange and extraction chromatography were used to separate actinium from the thorium target, isotopes of protactinium and radium, and the large number of fission products generated in each irradiation. Although a detailed explanation of the chemical purification is beyond the scope of this thesis, a brief description is useful to outline the measures required to determine the chemical yield of actinium, specifically ^{227}Ac.

Chemical processing varied slightly for each target, as new methods and process optimization were implemented after each irradiation. The most commonly used procedure employed a series of anion exchange columns for bulk thorium removal [28] followed by a lanthanide/actinium separation (Figure 10). Typically, chemical processing consisted of five ion
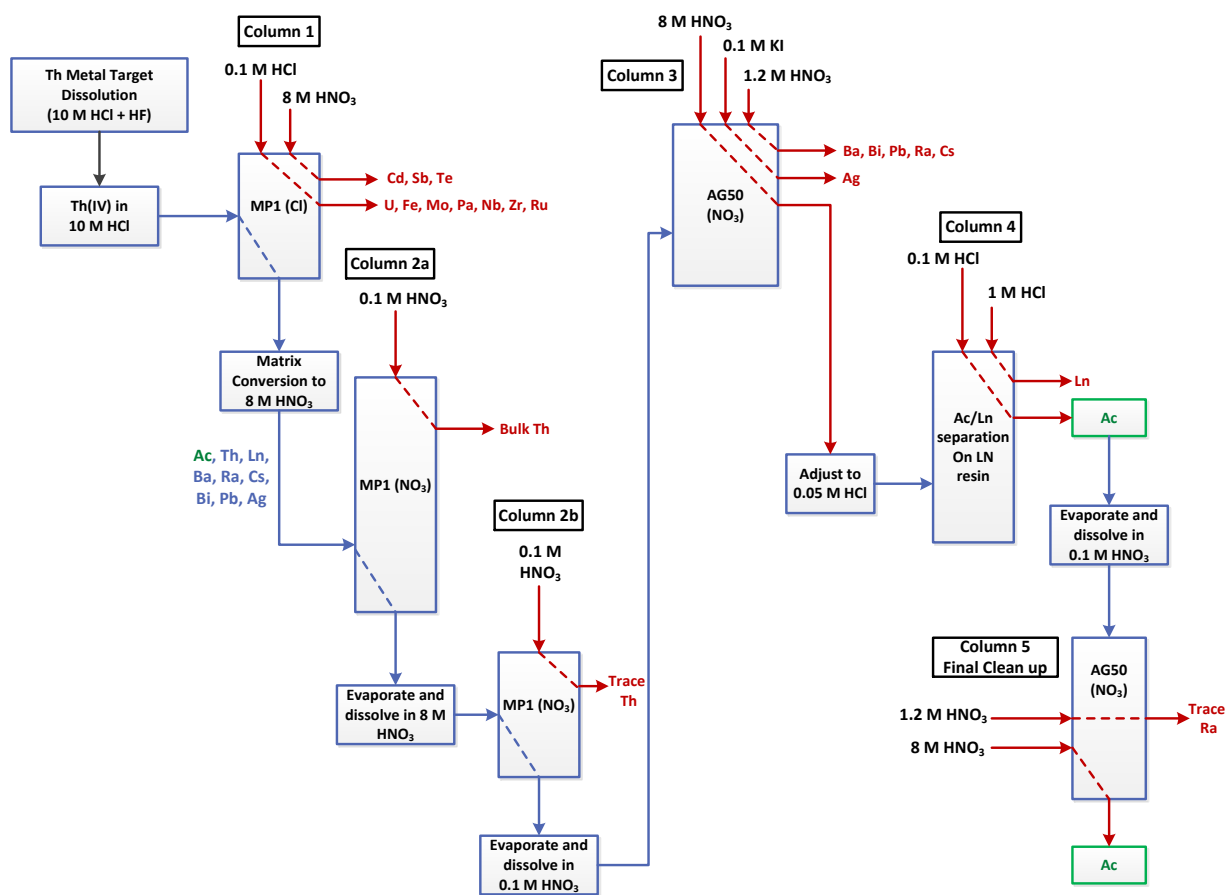
Figure 10. Ion-exchange chromatography process to purify actinium.

exchange columns. Briefly, the first anion exchange column was used in 10 M HCl media to facilitate separation of actinium from protactinium isotopes and most of the higher-activity non-lanthanide fission products, such as molybdenum and silver. The second and third anion exchange columns used 8 M HNO_3 media to separate the large quantity of thorium still present in the dissolved target solution. Next, a cation exchange column was used to separate the divalent alkali earth metals (calcium, strontium, barium, and radium) from the actinium (1.2 M HNO_3) and to eliminate trace amounts of silver that leaked from the first column. This was followed by an actinium/lanthanide separation column using extraction chromatography, such as Eichrom Ln resin [29] or DGA resin [30]. This aspect of the separation is highly sensitive as the lanthanide (III) and actinium (III) cations exhibit very similar chemical properties. All fractions of each ion exchange column were collected for analysis and diluted as necessary for γ-ray spectroscopy.

2.3 Gamma Ray Spectroscopy and Effective Cross Section Measurements

Radioactivity measurements were conducted using a well-shielded, Canberra Model GC2020 High-Purity Germanium detector with a relative efficiency of 20%. A PC-based multichannel analyzer utilizing Canberra Genie 2000 software was coupled to the detector. The measured resolution of the detector was 2.0 keV at 1.33 MeV. Energy and efficiency calibrations were completed using a γ-ray source traceable to the National Institute of Standards and Technology (NIST). Spectra collection times varied from one-hour counts for initial sample dilutions to 36-hour counts for severely decayed samples. Sample to detector geometry was varied to reduce the detector dead time below 5%.

Each peak in the γ-ray spectra was fitted using the non-linear least squares fit method [31]. In this method, the net area in a single peak is calculated using Equation 7 below where G is the

26

sum of the gross counts in the peak region of interest (ROI) and B is the area of the background/Compton continuum.

$$S = G - B \qquad\qquad \textit{Equation 7.}$$

The background/Compton continuum was calculated using the linear continuum equation (Equation 8) where N is the number of channels in the peak ROI, n is the number of continuum channels on each side, B_1 is the sum of counts in the continuum region to the left of the peak, and B_2 is the sum of the counts in the continuum region to the right of the peak.

$$B = \left(\frac{N}{2n}\right)(B_1 + B_2) \qquad\qquad \textit{Equation 8.}$$

Uncertainty of the net peak area is calculated by propagating the uncertainty for the area of the background/Compton continuum and the uncertainty of the gross counts in the peak. Since both B and G shown in Equation 7 above are Poisson distributed quantities, the propagated uncertainty for the net peak area (S) is given simply by Equation 9 below.

$$\sigma_S = \sqrt{\sigma_G^2 + \sigma_B^2} = \sqrt{G + \left(\frac{N}{2n}\right)^2 (B_1 + B_2)} \qquad\qquad \textit{Equation 9.}$$

Equation 7 – Equation 9 were all performed automatically within the framework of the Genie 2000 software while Equation 10 – Equation 19 (below) were applied through a series of Microsoft Excel spreadsheets. After each count, Genie 2000 automatically divides the net peak area by the total count time to report a value of counts per second (CPS) along with a fractional uncertainty in percentage (σ_s/S). However, for short lived isotopes and longer count times, it is necessary to correct for the decay during the count as shown in Equation 10 where CPS_u is the

27

uncorrected CPS, t is time (s), and λ_i is the decay constant (s^{-1}) for the radionuclide that corresponds to that γ- ray emission.

$$CPS_{E,i} = \frac{CPS_u \times t \times \lambda_i}{1 - e^{-\lambda_i t}} \qquad \textit{Equation 10.}$$

The decay constant is calculated simply as follows where $t_{1/2}$ corresponds to the published half-life for the nuclide of interest in seconds:

$$\lambda_i = \frac{ln(2)}{t_{1/2}} \qquad \textit{Equation 11.}$$

Activity in becquerels (Bq) for each sample for radionuclide (i) based on γ-ray energy (E) is given in Equation 12 where ε_E is the fractional absolute efficiency of the detector at E and I_γ is the fractional intensity of the γ- ray emission.

$$A_{E,i} = \frac{CPS_{E,i}}{\varepsilon_E \times I_\gamma} \qquad \textit{Equation 12.}$$

Fractional uncertainty in activity calculated using a single γ-ray emission is given in Equation 13 below where σ_s is the fractional uncertainty in the net peak area as given by Equation 9 and $\sigma_{I\gamma}$ is the uncertainty in the γ-ray intensity as reported by the Nuclear Data Sheets [32-43].

$$\sigma_{E,i} = \sqrt{\sigma_s^2 + \sigma_{I_\gamma}^2} \qquad \textit{Equation 13.}$$

When possible, multiple γ-ray peaks were used to quantify the activity at end of bombardment (EOB) for each radioisotope through a weighted average method. The weighted average of the activity of a specific sample at the time of count ($A_{i,TOC}$) is calculated using

Equation 14 and the values calculated in Equation 12 and Equation 13, summed for all relevant

γ-ray emissions for each radionuclide.

$$A_{i,TOC} = \sum A_{E,i} \times \sigma_{E,i}^{-2}$$ *Equation 14.*

Equation 15 corrects the weighted mean activity at time of count back to weighted mean activity

at end of bombardment ($A_{i,EOB}$).

$$A_{i,EOB} = \frac{A_{i,TOC}}{e^{-\lambda t}}$$ *Equation 15.*

By summing the fractional uncertainties of all γ-rays used in the activity measurement for a

specific isotope, Equation 16 gives the absolute fractional uncertainty of the weighted mean

activity for each radionuclide.

$$\sigma_A = \sqrt{\frac{1}{\sum \sigma_{E,i}^2}}$$ *Equation 16.*

Since each sample was heavily diluted to reduce detector dead time, each sample was

multiplied by its dilution factor. The dilution factor is calculated in Equation 17 where V_i is the

initial sample volume, and V_f is the final sample volume after the addition of inert solvent.

$$DF = \frac{V_f}{V_i}$$ *Equation 17.*

Often, three or fewer γ-rays from each radionuclide were used due to the complicated

spectrum generated from hundreds of fission products and a number of isotopes of protactinium,

thorium, actinium, radium, and several decay daughters of these chains. Two examples of spectra

collected over the course of this project are shown below. The top half of Figure 11 shows a
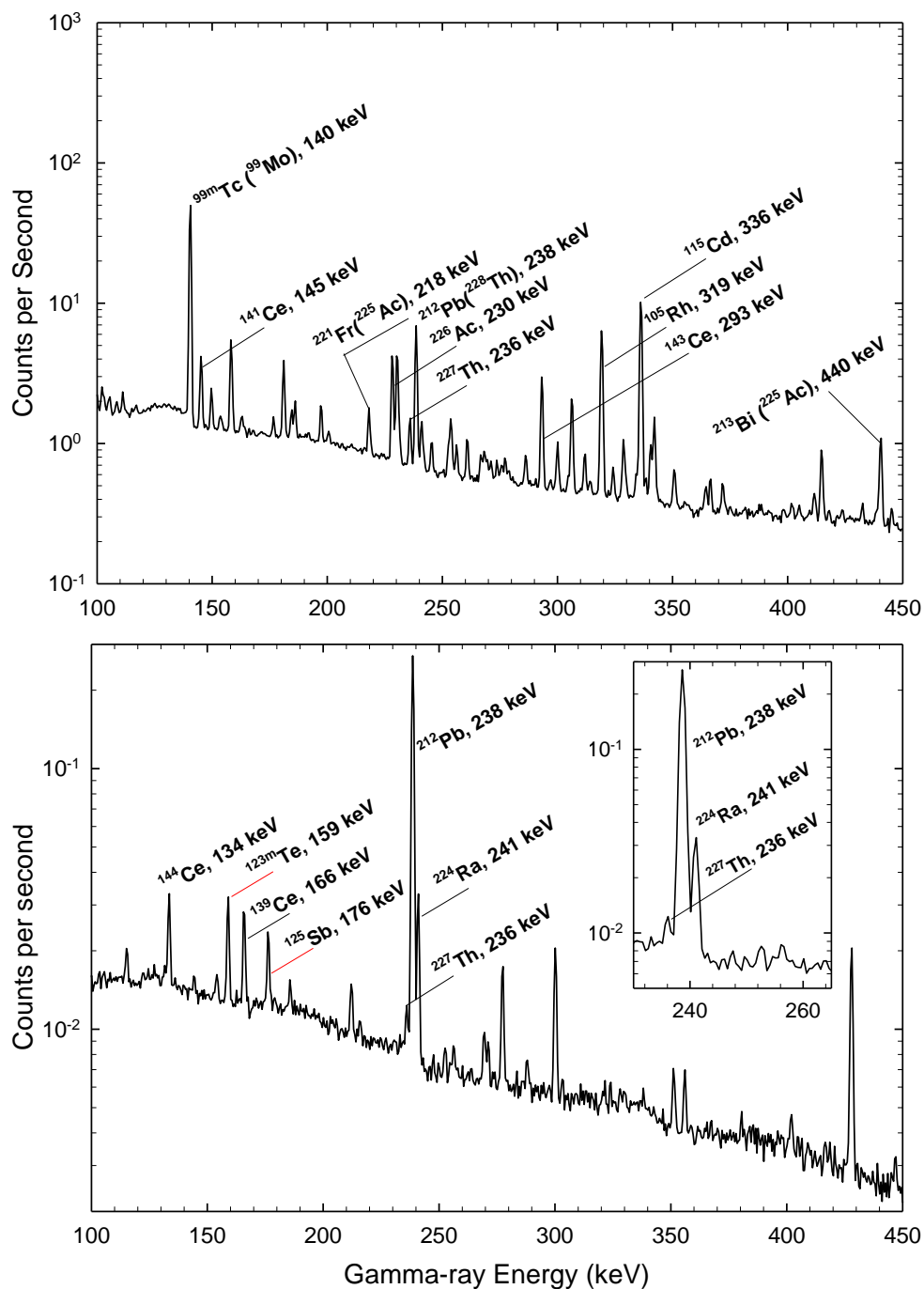
Figure 11. Gamma-ray spectra of a sample of target solution taken ~57 hours post EOB (TOP), and after ~17 months of decay (BOTTOM). As indicated in the expanded view, the 236 keV γ-ray peak from ^{227}Th ($t_{1/2}$ = 18.7 d) is visible after 16 months of decay — an indication of presence of the ^{227}Ac ($t_{1/2}$ = 21.8 y) predecessor in the sample.

γ-ray spectrum of a dissolved foil sample within one day of dissolution and within three days of EOB, and the bottom half of Figure 11 shows the same sample spectrum after ~16 months of decay.

The principal γ-ray energies, intensities, and appropriate branching ratios (if necessary) used in this study (Table 4) were acquired from the Nuclear Data Sheets [32-43]. Cross sections were calculated by using the activation equation shown below (Equation 18) where $A_{i,EOB}$ is activity at end of bombardment (Bq) as calculated in Equation 15, N is area density (atoms · cm^{-2}) of the target, and φ is the current or proton flux (protons · s^{-1})

$$\sigma_{tot} = \frac{A_{i,EOB}}{N*\varphi}$$
Equation 18.

Cross section uncertainties were calculated using a simple error propagation of the calculated fractional uncertainty of activity given in Equation 16 and the estimated fractional uncertainties for target mass (6.7–11.9%), beam intensity (7–10%), and sampling and detector efficiency (5%). Equation 19 gives the final fractional uncertainty for each experimentally measured cross section where σ_A/A is the fractional uncertainty in the activity at EOB, σ_m/m is the fractional uncertainty in target mass, $\sigma_\varepsilon/\varepsilon$ is the fractional uncertainty in sampling and detector efficiency, and σ_φ/φ is the fractional uncertainty in the beam intensity.

$$uncertainty\ in\ \sigma_{tot} = \sqrt{\left(\frac{\sigma_A}{A}\right)^2 + \left(\frac{\sigma_m}{m}\right)^2 + \left(\frac{\sigma_\varepsilon}{\varepsilon}\right)^2 + \left(\frac{\sigma_\varphi}{\varphi}\right)^2}$$
Equation 19.

Table 4. Principal γ-ray emissions used for assay of radionuclides produced in high energy-proton irradiation of ^{232}Th.

Radionuclide	Half-life	Eγ (keV)	Iγ (%)	Cool-Off Period Required?	Possible Reaction Pathways	Comments
^{99}Mo	66.0 h	739.5	12.3	No	^{232}Th[p,f]	
^{140}Ba	12.8 d	537.3	24.4	No	^{232}Th[p,f]	
^{139}Ce	137.6 d	165.9	80.0	Yes	^{232}Th[p,f]	
^{141}Ce	32.5 d	145.4	48.3	Yes	^{232}Th[p,f]	
^{143}Ce	33.0 h	293.3	42.8	No	^{232}Th[p,f]	
^{144}Ce	284.9 d	133.5	11.1	Yes	^{232}Th[p,f]	
^{225}Ac	9.92 d	440.5 (^{213}Bi)	25.9	No	^{232}Th[p,α4n]^{225}Ac ^{232}Th[p,αp3n]^{225}Ra[β-,14.9d]→^{225}Ac ^{232}Th[p,p7n]^{225}Th[EC, 8.8m]→^{225}Ac	Assayed from ^{213}Bi daughter
^{226}Ac	29.4 h	230.0	26.9	No	^{232}Th[p,α3n]^{226}Ac	
^{227}Ac	21.8 y	236.0 (^{227}Th)	12.9	Yes	^{232}Th[p,α2n]^{227}Ac ^{232}Th[p,αpn]^{227}Ra(β-,42.2m)→^{227}Ac	See text for assay method.
^{227}Th	18.7 d	236.0	12.9	No	^{232}Th[p,p5n]^{227}Th ^{232}Th[p,6n]^{227}Pa(EC,38.3m)→^{227}Th	Also used to quantify ^{227}Ac after Th separation and decay
^{228}Th	1.91 y	238.6 (^{212}Pb)	43.6	Yes	^{232}Th[p,p4n]^{228}Th ^{232}Th[p,5n]^{228}Pa(EC,22.4h)→^{228}Th ^{232}Th[p,αn]^{228}Ac(β-,6.2h)→^{228}Th	Assayed from ^{212}Pb daughter

2.4   PHITS Monte Carlo Calculations

Theoretical calculations of the cross sections measured for this experiment were performed using PHITS (Particle and Heavy Ion Transport code System). PHITS is a Monte Carlo based particle transport simulation code managed by the Japan Atomic Energy Agency that is able to process the transport of particles as well as the collisions of particles with target nuclei. PHITS is capable of calculating the transport of nuclei, nucleons, photons, electrons, and mesons. The continuous-slowing down approximation is applied to charged particle transport using the computer code SPAR [44]. The physical models that can be applied with the PHITS code are shown in Figure 12 [45]. For these calculations, PHITS Version 2.64 was employed through a combination of the intra-nuclear cascade (INCL 4.6) and evaporation (GEM) models to determine the proton reaction cross sections of the irradiations occurring in the 70-200 MeV incident proton energy range [46].

Figure 12. Recommended physics models for PHITS.
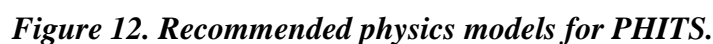
In order to decrease the overall simulation time but still achieve the desired accuracy, the geometry of the model was simplified significantly. A simple sketch of the model is shown in Figure 13. The thorium foil was modeled as a simple cylinder with a diameter and thickness equal to that of the thorium foils irradiated at BLIP or IPF. The proton beam was modeled as a cylindrical source with a 0.5 cm radius incident upon the center of the thorium foil's face. Due to range straggling and multiple Coulomb scattering, the incident proton beams from BLIP and IPF have a small deviation in energy by the time they reach the target thorium foil. However, for the ease of simulation, a monoenergetic proton beam of the mean energy from the TRIM calculations listed in Table 2 was used for the PHITS calculations.
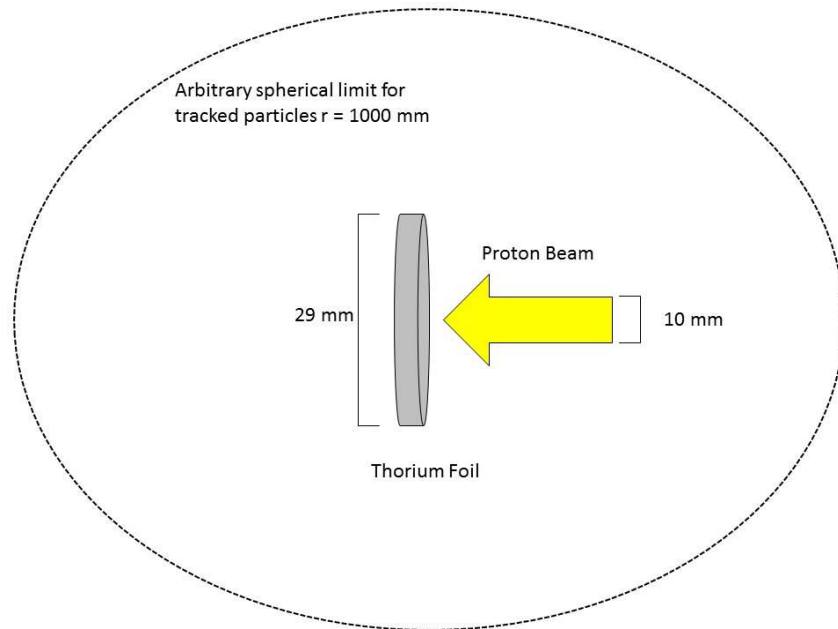
Figure 13. Simplified geometry in PHITS calculation.

Computation time varied from 4-7 hours by changing the number of particles in each simulation. Since the IPF foils had approximately three times the areal density of the BLIP foils

and the incident proton energy was much lower, each simulated proton had a much higher chance of interacting with target nuclei. This led to an increased computation time per particle for the IPF irradiations vs. the BLIP irradiations. For this reason, 250 million particles per run were tracked for the IPF irradiations (77 and 90 MeV) and 500 million particles were tracked for the BLIP irradiations (128, 153, 174, and 192 MeV). The PHITS tally *T-Product* was used to track the production of radionuclides through spallation reactions and fission. Six isotopes each of radium, actinium, thorium, and protactinium were tallied. In order to be thorough, six isobars of fission products from A = 82 to A = 168 were also tallied. Unfortunately, PHITS limits the number of *T-Product* tallies that can be used per simulation to twenty, and further limits each *T-product* tally to six reaction products each. For each of the seven irradiation energies, five simulations were performed, equaling a total of 35 simulations.

Each *T-Product* tally generates its own output text file with a list of the product nuclei tallied for each simulation. Each output text file, some of which containing several thousand lines of reaction products, required dissection in order to organize all relevant data. A Microsoft Excel Visual Basic Macro was developed to help tabulate cross section data from the PHITS generated text files. This allowed for a faster processing time and limited the possibility of human error that can occur through the monotonous copying and pasting of hundreds of text files.

Excel was also used to calculate each independent cross section by summing the total number of nuclei produced (N_f) and dividing by the total number of protons simulated (N_p) and the target density (n_t) in atoms·cm^{-2} as shown in Equation 20.

$$\sigma_I = \frac{N_f}{N_p \cdot n_t} \hspace{4cm} \textbf{\textit{Equation 20}}$$

35

It is important to note that the PHITS output includes only radionuclides produced independent of decay whereas, experimental effective cross sections that are reported in this work are considered cumulative. However, for the fission products tallied in the PHITS simulation, it is not useful to calculate the independent production cross sections because high-energy proton fission of heavy radionuclides such as ^{232}Th tends to favor short-lived, neutron-rich fission products. Therefore, for the PHITS calculated reaction cross sections of the six fission products presented in this work, a cumulative cross section was calculated by summing two to six of the associated isobars.

Uncertainty for each PHITS calculated cross section was assumed to be governed by Poisson statistics. Therefore, Equation 21 was used to determine the fractional uncertainty of a PHITS generated cross section where N was the total number of product nuclei generated in each simulation.

$$fractional\ uncertainty\ of\ \sigma_I = \frac{\sqrt{N}}{N} \qquad\qquad \textit{Equation 21}$$

2.5 Analysis of Decayed ^{225}Ac/^{213}Bi Generators

Although there have been several clinical studies surrounding the direct use of ^{225}Ac in the body, the majority of clinical studies involve the use of ^{225}Ac/^{213}Bi generators. Primarily, these generators are manufactured with ^{225}Ac obtained through the decay of the long-lived ^{229}Th as mentioned in Section 1.3. Taking advantage of this decay chain (Figure 1), ^{225}Ac can be routinely chemically separated from ^{229}Th and ^{225}Ra through an ion exchange chromatographic system [28]. However, when produced through the spallation of ^{232}Th, ^{225}Ac is accompanied by the production of isotopes of protactinium, thorium, radium, other isotopes of actinium, and hundreds of fission products. These coproduced radionuclides have a wide range of half-lives

from less than a second to several years. As outlined in Section 2.2 above, it is crucial to separate the longer-lived nuclides from the actinium as quickly and efficiently as possible.

Isotopes of protactinium, radium, thorium, and fission products can be separated from ^{225}Ac chemically, however isotopes of actinium (i.e. ^{226}Ac and ^{227}Ac) cannot be separated chemically and remain with the actinium fraction. Fortunately, due to its short half-life, ^{226}Ac has little to no effect on the use of accelerator produced ^{225}Ac as a ^{213}Bi generator or on the use of ^{225}Ac directly. However, the effect of the presence of the long-lived ^{227}Ac on clinical trials employing ^{225}Ac directly is currently being researched, specifically on the effect of its longer-lived daughter products ^{227}Th and ^{223}Ra ($t_{1/2}$ = 11.43d). The entire ^{227}Ac decay chain is shown in Figure 14.
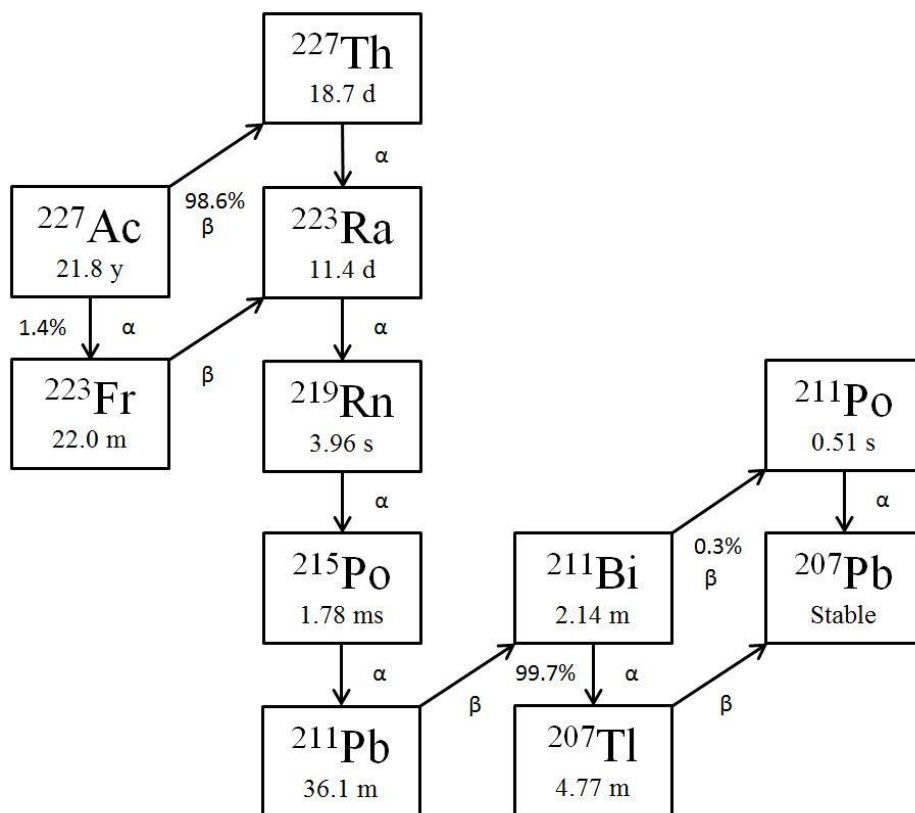
Figure 14. Actinium-227 Decay Chain.

At the time of shipment, ^{225}Ac/^{213}Bi shipped as generators produced through the spallation process usually contain 1-20 mCi of ^{225}Ac and γ-ray spectroscopy analysis of the purified actinium fraction reveals only the presence of ^{225}Ac and its daughter products ^{221}Fr and ^{213}Bi. All possible contaminants would be overwhelmed by the background Compton continuum created by the γ-ray emissions from the ^{225}Ac decay chain. However, after the generator has surpassed its operational lifetime (1-2 months), it can be returned to ORNL for further analysis.

One of the main objectives this work was to determine if any long-lived contaminants, other than ^{227}Ac ($t_{1/2} = 21.8$y) and its associated decay products, followed ^{225}Ac to the ^{225}Ac/^{213}Bi generator stage. Two separate generators used by nuclear medicine researchers from Johns Hopkins University (JHU) and Yeshiva University (YU) were analyzed. The generators were originally constructed using a small bed volume (<0.5 mL) of AGMP-50 cation exchange resin in a small quartz column, as shown in Figure 15.
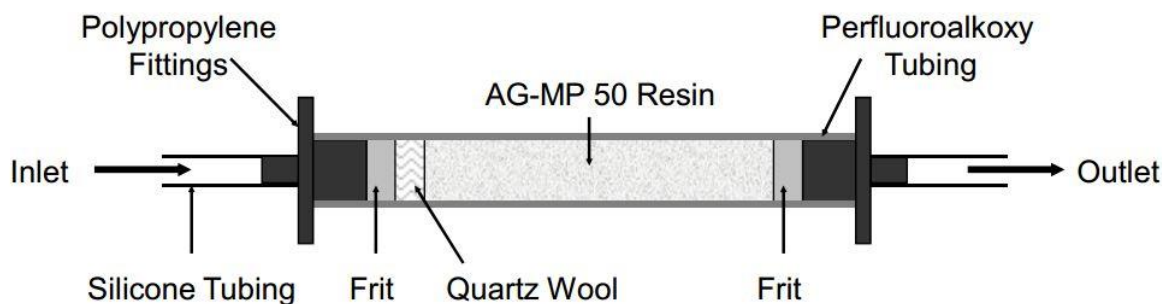
Figure 15. Typical ^{225}Ac/^{213}Bi generator [2].

Two independent methods were used in the analysis of the two generators in an attempt to detect longer-lived contaminants unassociated with the ^{227}Ac decay chain. First, the ^{225}Ac/^{213}Bi generator originally from JHU was eluted according to a commonly used method reported in

literature [47]. In a small adaptation of this technique, 0.15M KI/0.1M HCl was used for the elution of bismuth instead of 0.15M NaI/0.1M HCl since KI was readily available in the lab where this experiment was performed. Since the both alkali salts readily dissolve in 0.1 M HCl, KI can be used interchangeably with NaI. A procedure outlining the original operation for the generator was provided by researchers at JHU [48]. In this procedure, the generator was eluted with 6 fractions of 0.5 mL 0.15M NaI/0.1M HCl. Mimicking this procedure, the generator was eluted using 0.15M KI/0.1M HCl, and all fractions were collected in a single 10 mL glass septum vial. The vial was then immediately assayed via γ-ray spectroscopy for 10 x 10 minute counts. An overnight count of this sample was then performed two weeks later; after the short-lived decay products, primarily ^{211}Pb ($t_{1/2} = 36.1$ m) had entirely decayed away.

The second method used to reveal any unknown long-lived radio-contaminants was applied to the generator returned to ORNL by YU. Instead of attempting to elute any unknown contaminants off the generator, the relatively longer lived ($t_{1/2} > 30$ min) daughter products of the ^{227}Ac chain other than ^{227}Th (^{223}Ra, and ^{211}Pb) were selectively eluted. In this technique, 5 mL of 6 M HNO_3 was passed through the generator. This fraction of 6 M HNO_3 was collected in a 10 mL glass septum vial. Then the generator itself was assayed through γ-ray spectroscopy.

3 Results and Discussion

  Measured cross sections of the isotopes of interest are given in Table 5 and Table 7 and depicted in Figure 16 − Figure 27. The PHITS simulated cross sections are shown in Table 6 and Table 8. The ratios of the PHITS simulated cross sections to the experimentally measured effective cross sections are given in Table 9. As mentioned before, PHITS simulated cross sections for the actinium and thorium isotopes are independent cross sections that do not include any contributions from decay of precursors. However, for useful comparisons, simulated cross sections for the selected fission products are displayed as independent and cumulative cross sections. The radionuclides that contribute to the reported simulated cumulative cross sections are listed in Section 3.4. Additional simulated cross sections are tabulated in Appendix B. Measured cross sections at 90, 128, and 192 MeV are given as averages with propagated uncertainty since two irradiations at IPF occurred at 90 MeV, six irradiations at BLIP occurred at 128 MeV, and five additional irradiations at BLIP occurred at 192 MeV. As shown in Figure 16 − Figure 27, the cross sections measured in this work mimic the energy dependence shown by cross sections reported previously [23, 49-56].

Table 5. Effective production cross sections (in mb) of ^{225}Ac and other radioisotopes from ^{232}Th target irradiated with 77-90 MeV protons at IPF.

Isotope	Half-life	76.5 ± 0.8 MeV	89.9 ± 0.4 MeV
^{225}Ac	9.92 d	3.6 ± 0.5	6.6 ± 0.9
^{226}Ac	29.37 h	N/M	N/M
^{227}Ac	21.77 y	4.5 ± 0.7	6.3 ± 1.0
^{227}Th	18.72 d	37.2 ± 5.0	35.8 ± 4.9
^{228}Th	697.15 d	56.7 ± 7.2	47.6 ± 6.1
^{99}Mo	65.98 h	32.7 ± 4.2	35.9 ± 4.6
^{140}Ba	12.75 d	14.2 ± 1.8	11.7 ± 1.7
^{139}Ce	137.64 d	0.4 ± 0.1	0.6 ± 0.1
^{141}Ce	32.50 d	N/M	15.8 ± 2.0
^{143}Ce	33.04 h	16.5 ± 2.1	N/M
^{144}Ce	285.00 d	12.6 ± 1.6	8.7 ± 1.4

[*]N/M = Not measured

Table 6. PHITS simulated production cross sections (in mb) of ^{225}Ac and other radioisotopes from ^{232}Th target irradiated with 77-90 MeV protons at IPF.

Isotope	Half-life	76.5 ± 0.8 MeV	89.9 ± 0.4 MeV
^{225}Ac	9.92 d	7.8 ± 0.1	11.8 ± 0.1
^{226}Ac	29.37 h	7.4 ± 0.1	12.6 ± 0.1
^{227}Ac	21.77 y	12.2 ± 0.2	17.1 ± 0.1
^{227}Th	18.72 d	37.6 ± 0.3	31.5 ± 0.2
^{228}Th	697.15 d	80.3 ± 0.4	65.9 ± 0.3
^{99}Mo*	65.98 h	32.8 ± 0.6	32.5 ± 0.4
^{140}Ba*	12.75 d	21.6 ± 0.4	20.4 ± 0.3
^{139}Ce*	137.64 d	0.32 ± 0.03	0.32 ± 0.03
^{141}Ce*	32.50 d	21.1 ± 0.3	19.3 ± 0.3
^{143}Ce*	33.04 h	17.4 ± 0.4	16.5 ± 0.3
^{144}Ce*	285.00 d	15.4 ± 0.4	14.4 ± 0.3

*Given as cumulative cross section of several radionuclides. See text for explanation

Table 7. Effective production cross sections (in mb) of ^{225}Ac and other radioisotopes from ^{232}Th target irradiated with 128-192 MeV protons at BLIP.

Isotope	Half-life	127.8 ± 0.5 MeV	152.5 ± 0.5 MeV	173.6 ± 0.5 MeV	192.1 ± 0.5 MeV
^{225}Ac	9.92 d	10.8 ± 1.5	13.0 ± 1.3	16.7 ± 1.6	14.0 ± 1.6
^{226}Ac	29.37 h	8.1 ± 1.0	11.4 ± 1.3	13.0 ± 1.5	14.7 ± 1.7
^{227}Ac	21.77 y	26.5 ± 3.5	18.6 ± 2.8	14.0 ± 1.9	16.2 ± 2.7
^{227}Th	18.72 d	26.3 ± 4.0	26.0 ± 2.9	24.3 ± 2.7	25.8 ± 3.4
^{228}Th	697.15 d	42.5 ± 4.0	46.7 ± 4.5	41.8 ± 3.9	37.1 ± 3.1
^{99}Mo	65.98 h	29.6 ± 4.2	34.9 ± 3.4	36.3 ± 3.4	25.8 ± 3.0
^{140}Ba	12.75 d	10.9 ± 1.5	13.4 ± 1.4	14.0 ± 1.7	5.2 ± 1.1
^{139}Ce	137.64 d	3.6 ± 0.5	1.4 ± 0.2	1.6 ± 0.2	1.5 ± 0.2
^{141}Ce	32.50 d	11.5 ± 1.6	N/M	N/M	9.4 ± 1.1
^{143}Ce	33.04 h	7.0 ± 1.0	8.1 ± 0.8	7.9 ± 0.7	7.2 ± 0.7
^{144}Ce	285.00 d	10.0 ± 1.5	6.9 ± 0.7	6.3 ± 0.6	6.4 ± 0.8

[*]N/M = Not measured

Table 8. PHITS simulated cross sections (in mb) of ^{225}Ac and other radioisotopes from ^{232}Th target irradiated with 128-192 MeV protons at BLIP.

Isotope	Half-life	127.8 ± 0.5 MeV	152.5 ± 0.5 MeV	173.6 ± 0.5 MeV	192.1 ± 0.5 MeV
^{225}Ac	9.92 d	26.0 ± 0.3	28.4 ± 0.3	28.2 ± 0.4	28.2 ± 0.4
^{226}Ac	29.37 h	21.8 ± 0.2	23.0 ± 0.2	22.8 ± 0.3	22.9 ± 0.3
^{227}Ac	21.77 y	25.6 ± 0.3	26.2 ± 0.3	26.3 ± 0.4	25.3 ± 0.4
^{227}Th	18.72 d	25.6 ± 0.3	22.1 ± 0.2	19.6 ± 0.3	18.1 ± 0.3
^{228}Th	697.15 d	51.9 ± 0.4	44.7 ± 0.3	39.8 ± 0.5	37.2 ± 0.4
^{99}Mo*	65.98 h	31.5 ± 0.8	30.5 ± 0.8	31.0 ± 0.8	31.5 ± 0.8
^{140}Ba*	12.75 d	15.9 ± 0.5	13.8 ± 0.5	12.8 ± 0.3	11.5 ± 0.5
^{139}Ce*	137.64 d	0.58 ± 0.07	0.72 ± 0.08	0.71 ± 0.06	0.80 ± 0.09
^{141}Ce*	32.50 d	15.2 ± 0.6	13.4 ± 0.5	12.9 ± 0.3	12.2 ± 0.5
^{143}Ce*	33.04 h	12.4 ± 0.4	11.0 ± 0.5	10.3 ± 0.4	9.7 ± 0.4
^{144}Ce*	285.00 d	11.0 ± 0.3	9.9 ± 0.4	9.1 ± 0.4	8.5 ± 0.4

*Given as cumulative cross section of several radionuclides. See text for explanation

Table 9. Ratio of PHITS Simulated Cross Section to Experimentally Measured Effective Cross Section.

Isotope	Half-life	76.5 ± 0.8 MeV	89.9 ± 0.4 MeV	127.8 ± 0.5 MeV	152.5 ± 0.5 MeV	173.6 ± 0.5 MeV	192.1 ± 0.5 MeV
^{225}Ac	9.92 d	2.17	2.15	2.41	2.18	1.69	2.01
^{226}Ac	29.37 h	N/M	N/M	2.69	2.02	1.75	1.56
^{227}Ac	21.77 y	2.71	3.05	0.97	1.41	1.88	1.56
^{227}Th	18.72 d	1.01	0.85	0.97	0.85	0.81	0.70
^{228}Th	697.15 d	1.42	1.64	1.22	0.96	0.95	1.00
^{99}Mo	65.98 h	1.00	0.91	1.06	0.87	0.85	1.22
^{140}Ba	12.75 d	1.52	1.49	1.46	1.03	0.91	2.21
^{139}Ce	137.64 d	0.80	0.80	0.16	0.51	0.44	0.53
^{141}Ce	32.50 d	N/M	1.43	1.32	N/M	N/M	1.30
^{143}Ce	33.04 h	1.05	6.60	1.77	1.36	1.30	1.35
^{144}Ce	285.00 d	1.22	2.15	1.10	1.43	1.44	1.33

[*]N/M = Not measured

3.1 ^{232}Th[p,x]Ac reactions

The measured cross sections for the ^{232}Th[p,x]^{225}Ac reaction in the 20–200 MeV energy range are plotted together with literature values in Figure 16. As can be shown, cross sections for ^{225}Ac increase rather linearly from 3.6 ± 0.5 mb at $E_p = 77$ MeV to 16.7 ± 1.6 mb at $E_p = 174$ MeV and then decreases to 14.0 ± 1.6 mb at 192 MeV (Figure 16). PHITS simulated cross sections for this reaction are generally a factor of two higher in overall magnitude than the experimentally measured cross sections. However, the general shapes of the experimental excitation function and the simulated excitation function are similar with each excitation function approximately doubling in magnitude from 77 to 90 MeV and remaining constant with increasing proton energy from 128 to 192 MeV.

The experimental data for the ^{232}Th[p,x]^{225}Ac reaction is in close agreement with literature values at $E_p < 170$ MeV but ~25% lower than literature values at $E_p = 192$ MeV (Figure 16). Note that the cross section for this reaction includes a contribution from the β^- decay of ^{225}Ra, as well as a contribution from the electron capture decay (~10%) of ^{225}Th ($t_{1/2} = 8.75$ m). Earlier measurements showed that the cross section for the ^{232}Th[p,x]^{225}Ra reaction over this energy range is smaller than the ^{232}Th[p,x]^{225}Ac reaction cross section by a factor of 5–10 [23, 57]. Therefore, the contribution from ^{225}Ra decay will not be significant. However, efforts are in progress to quantify the ^{225}Ra yield for this set of experiments, as the ^{232}Th[p,x]^{225}Ra(β^-)^{225}Ac route will provide ^{225}Ac free from ^{227}Ac contamination. Presently, the effect of ^{227}Ac contamination on the performance of the ^{225}Ac/^{213}Bi generator and its effect on *in vivo* toxicity of accelerator produced ^{225}Ac are unknown but studies are currently under way to determine its effect. PHITS simulated cross sections for the ^{232}Th[p,x]^{225}Ac reaction are independent cross sections and are not affected by the coproduction and subsequent decay of ^{225}Ra; slightly
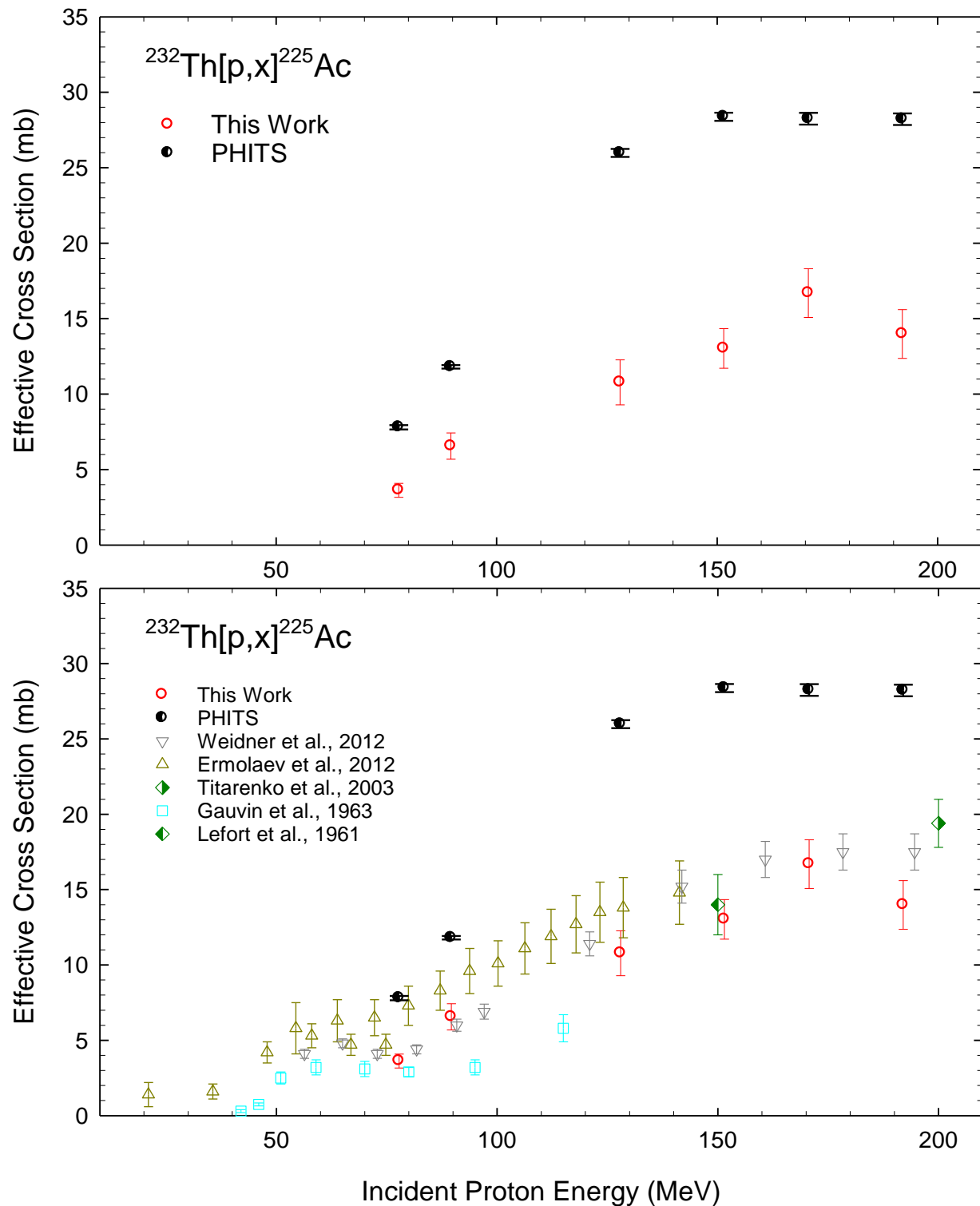
Figure 16. Experimental effective cross sections and cross sections computed with PHITS for the $^{232}Th[p,x]^{225}Ac$ reaction from 77 to 192 MeV (upper plot). Literature values for the same reaction are shown as a comparison in the lower plot.

increasing the discrepancy between the experimentally measured cross sections and the simulated cross sections even further.

Cross sections measured for the ^{232}Th[p,x]^{226}Ac reaction in the 128–200 MeV incident proton energy range together with literature values (E$_p$ = 20–200 MeV) are shown in Figure 17. Cross sections for this reaction also increase linearly from 8.1 ± 1.0 mb to 14.7 ± 1.7 mb at energies of 128 to 192 MeV, respectively. PHITS simulated cross sections for this reaction displayed an altogether different pattern with a slight increase from 7.4 ± 0.1 mb to 12.6 ± 0.1 mb at 77 and 90 MeV respectively. At the energies corresponding to the BLIP irradiations (128-192 MeV), the simulated cross sections are relatively constant with increasing energy. Similar to the ^{232}Th[p,x]^{225}Ac reaction excitation function, the experimental cross sections for the ^{232}Th[p,x]^{226}Ac reaction are also about a factor of two lower than the simulated cross sections.

The relatively short half-life of ^{226}Ac (29.4 h) limits accurate detection of this radionuclide because of the long delay between the end of bombardment and target assay. However, measurement of the production cross section of ^{226}Ac was possible in the overnight irradiations at BLIP followed by next day shipment. This enabled target assay approximately three days after EOB. The cross section values presented here are slightly lower than the previous measurements by Lefort *et al.* [52] and Engle *et al.* [53]. Actinium-226 is also fed through α-decay of ^{230}Pa, produced via the ^{232}Th[p,3n] reaction. No decay contributions were considered for this reaction since the α-branching ratio of ^{230}Pa is < 0.1%.

Figure 17. Experimental effective cross sections and cross sections computed with PHITS for the ^{232}Th[p,x]^{226}Ac reaction from 77 to 192 MeV (upper plot). Literature values for the same reaction are shown as a comparison in the lower plot.

As with the other isotopes of Ac, the cross sections for the ^{232}Th[p,x]^{227}Ac reaction increases from 4.5 ± 0.7 mb at 77 MeV to 6.3 ± 1.0 mb at 90 MeV (Figure 18). At 128 MeV, the cross section increases to 26.5 ± 3.5 mb, which differs by as much as a factor of three from literature values. Surprisingly, the data point at 128 MeV is in very close agreement with the PHITS simulated cross section at the same incident proton energy. However, like the ^{232}Th[p,x]^{225}Ac and ^{232}Th[p,x]^{226}Ac reaction excitation functions, the simulated excitation function for the ^{232}Th[p,x]^{227}Ac reaction is roughly a factor of two or more higher in magnitude than the experimentally measured excitation function. As a result, it is feasible to consider the experimentally measured data point at 128 MeV an extreme outlier. The reason for the large discrepancy from literature values and the overall shape of the excitation function may be due to complexities in the quantification of the long-lived ^{227}Ac radionuclide from the process described in Chapter 2, such as low count rate and dilution inaccuracies; but the true source is currently unknown.

In addition to direct formation, ^{227}Ac activity is fed by the decays of ^{227}Ra ($t_{1/2} = 42.2$ m) and ^{231}Pa ($t_{1/2} = 32{,}760$ y), but this effect is insignificant. The cross section for ^{227}Ra is likely much lower than for ^{227}Ac due to the ejection of an additional proton. At the same time, α-decay of ^{231}Pa has a negligible effect on the cumulative cross section because of its long half-life. As pointed out earlier, an accurate quantification of ^{227}Ac sometimes required chemical isolation of the actinium fraction. The weak γ-ray emissions of ^{227}Ac combined with the complex γ-ray spectra associated with the irradiated thorium foils caused the direct measurement of this long-lived radioisotope to be challenging. However, the activity of the daughter nuclei of ^{227}Ac, ^{227}Th ($t_{1/2} = 18.72$ d), was determined through the detection of the 236 keV (12.9%) γ-ray, and in a few instances it was possible to re-assay a sample of the target solution (dissolved foil) 12 to
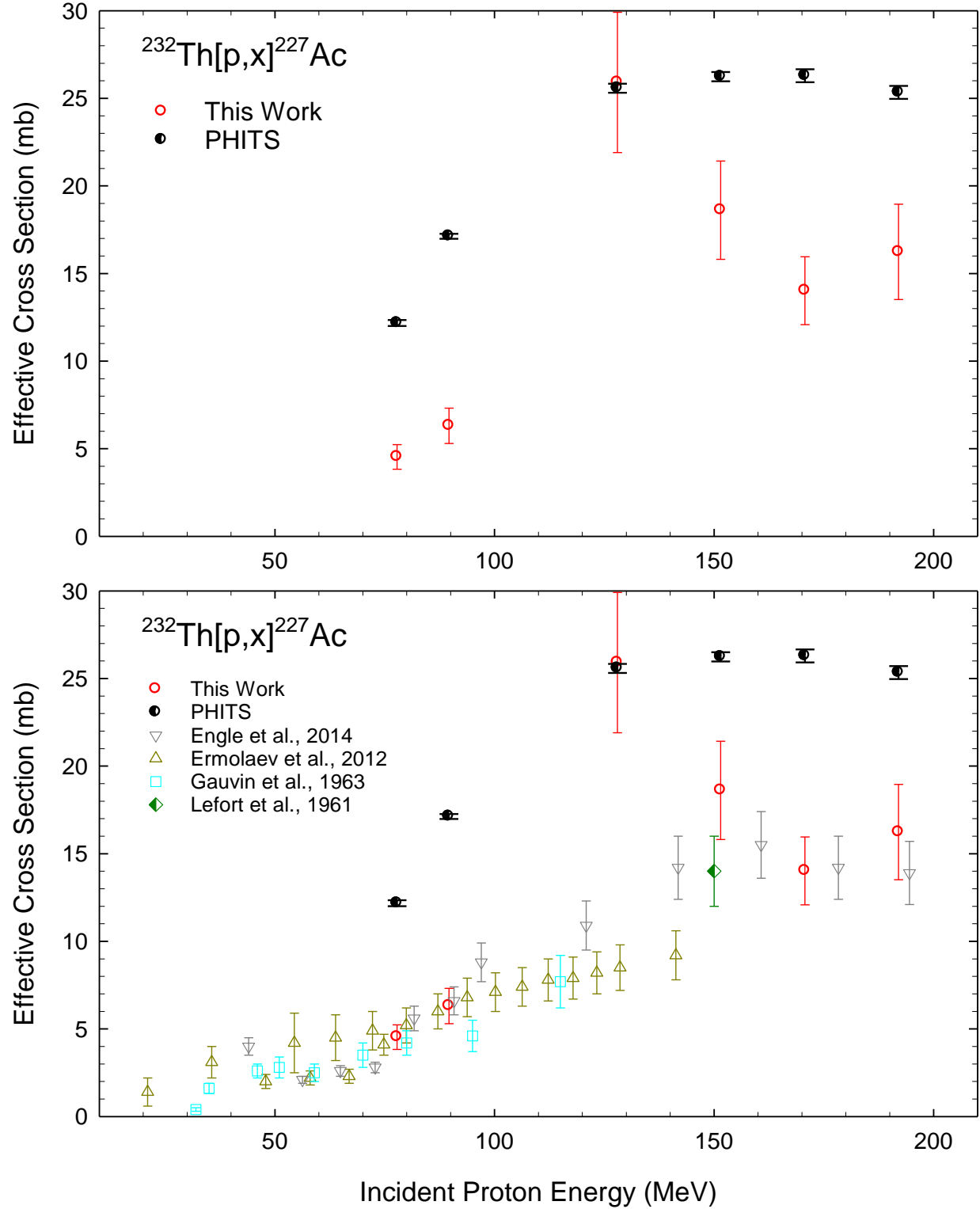
Figure 18. Experimental effective cross sections and cross sections computed with PHITS for the $^{232}Th[p,x]^{227}Ac$ reaction from 77 to 192 MeV (upper plot). Literature values for the same reaction are shown as a comparison in the lower plot.

18 months post EOB. This allowed ^{227}Th to reach secular equilibrium with ^{227}Ac while directly produced ^{227}Th decayed below the limit of detection. Further, decay of a number of longer-lived fission products such as ^{103}Ru ($t_{1/2}$ = 39.2 d) and ^{95}Zr ($t_{1/2}$ = 64.0 d) during this period resulted in a net reduction of the overall Compton continuum and hence an improvement in detection sensitivity. This is clearly demonstrated in the examples of spectra shown in Figure 11.

In the case of the later irradiations, ^{227}Ac activity was derived from the purified Ac fraction. After chemical separation, an aliquot of the Ac fraction was assayed by γ-ray spectroscopy to determine the activity of ^{227}Ac and ^{227}Th. Comparison of ^{225}Ac activity values in the target solution and in the Ac fraction provided an overall chemical yield. Thorium-227 was then allowed to grow into full secular equilibrium in the above sample (for >180 days) and then re-assayed, providing an accurate measure of the ^{227}Ac which was then corrected by taking into account chemical yield. The cross sections for the ^{232}Th[p,x]^{227}Ac reaction measured in this work agree with literature values with the exception of the aforementioned data point at 128 MeV.

3.2 ^{227}Ac/^{225}Ac Ratio

An important quantity for determining the purity of the ^{225}Ac that is produced through the high-energy proton irradiation of ^{232}Th is the ^{227}Ac/^{225}Ac ratio. Figure 19 and Table 10 compare the ^{227}Ac/^{225}Ac ratio as a function of energy. The y-axis for the top half of the figure is the cross section ratio: simply the experimentally measured cross section at a specific energy for the ^{232}Th[p,x]^{227}Ac reaction divided by the experimentally measured cross section for the ^{232}Th[p,x]^{225}Ac reaction. While this value is helpful from a nuclear data standpoint, it is often not very useful when comparing the ^{227}Ac activity to the ^{225}Ac activity at the end of bombardment, a value that is extremely useful for the application of ^{225}Ac/^{213}Bi in nuclear medicine. For comparison purposes, it is beneficial to multiply the cross section ratio by the ratio of the each of
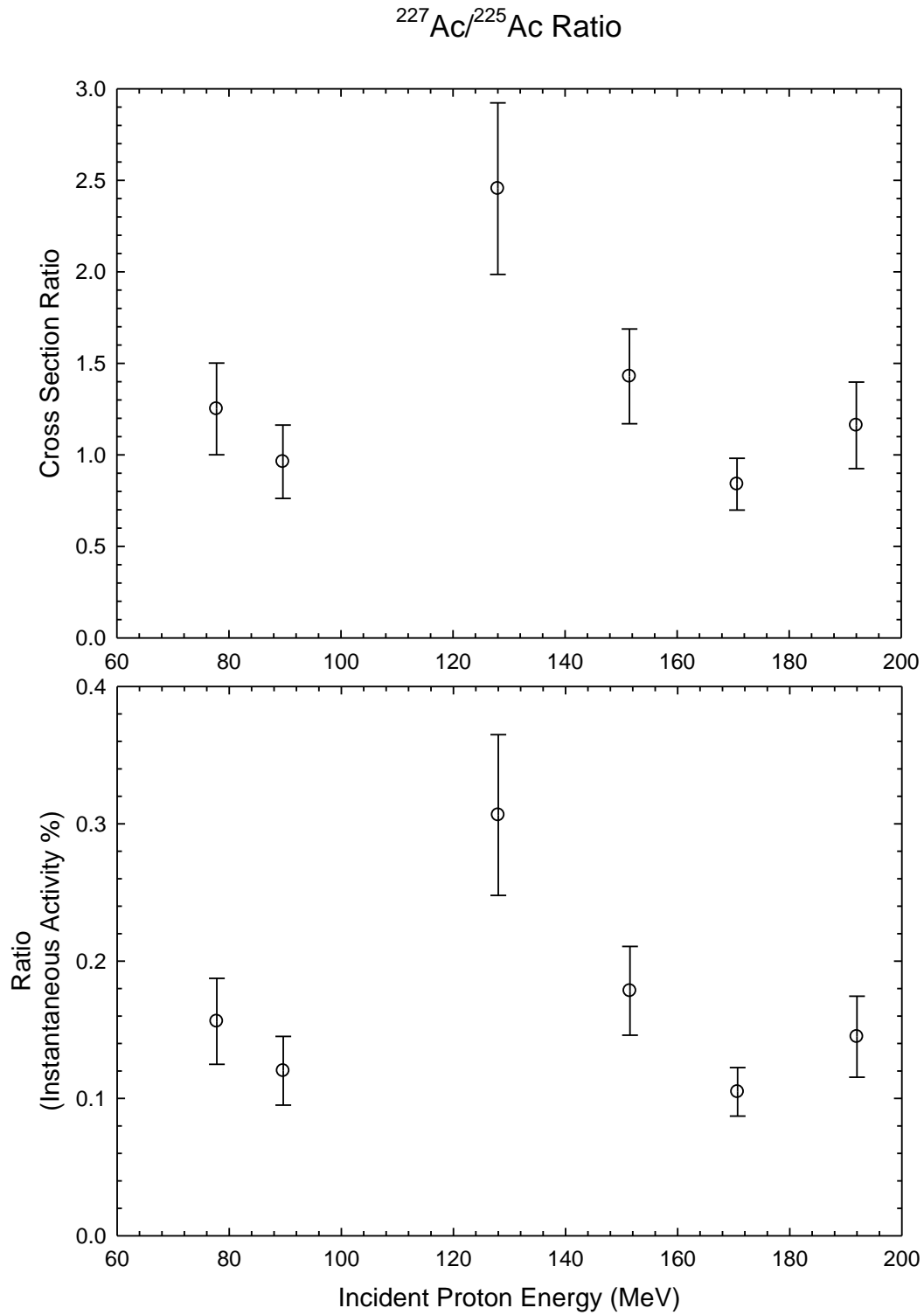
Figure 19. *[227]Ac/[225]Ac ratio based on cross section (upper plot) and the instantaneous activity percentage described in the text (lower plot).*

the decay constants (Equation 11) to obtain the activity ratio. This value is independent of

parameters such as irradiation time, proton current, and target thickness. In Table 10, this ratio is

given as a percentage.

Table 10. ^{227}Ac/^{225}Ac Ratio.

Proton Energy (MeV)	Ac-225 Cross Section (mb)	Ac-227 Cross Section (mb)	Cross Section Ratio	Activity Ratio (%)
76.5 ± 0.8	3.6 ± 0.5	4.5 ± 0.7	1.3 ± 0.3	0.16 ± 0.03
89.9 ± 0.4	6.6 ± 0.9	6.3 ± 1.0	1.0 ± 0.2	0.12 ± 0.02
127.8 ± 0.5	10.8 ± 1.5	26.5 ± 3.5	2.5 ± 0.5	0.31 ± 0.06
152.5 ± 0.5	13.0 ± 1.3	18.6 ± 2.8	1.4 ± 0.3	0.18 ± 0.03
173.6 ± 0.5	16.7 ± 1.6	14.0 ± 1.9	0.8 ± 0.1	0.10 ± 0.02
192.1 ± 0.5	14.0 ± 1.6	16.2 ± 2.7	1.2 ± 0.2	0.14 ± 0.03

Since the half-life of ^{227}Ac ($t_{1/2}$ = 21.8 y) is significantly longer than the half-life of ^{225}Ac

($t_{1/2}$ = 9.92 d), the ^{227}Ac/^{225}Ac ratio is always decreasing as a function of irradiation time.

However, it is crucial to determine the incident proton energy at which the ^{227}Ac/^{225}Ac ratio is

the smallest. As shown in Figure 19, the lowest ^{227}Ac/^{225}Ac ratio measured for the lower energy

IPF irradiations is at 90 MeV while the lowest ^{227}Ac/^{225}Ac ratio measured at BNL occurred at

174 MeV.

3.3 ^{232}Th[p,x]Th reactions

Although several other isotopes of thorium are generated in these irradiations, only the cross

sections for the ^{232}Th[p,x]^{227}Th and ^{232}Th[p,x]^{228}Th reactions are presented here in Figure 20 and

Figure 21. For the ^{232}Th[p,x]^{227}Th reaction, cross sections exhibit a maximum of 37.2 ± 5.0 mb

at 77 MeV followed by a slight decrease to a minimum value of 24.3 ± 2.7 mb at 174 MeV. The
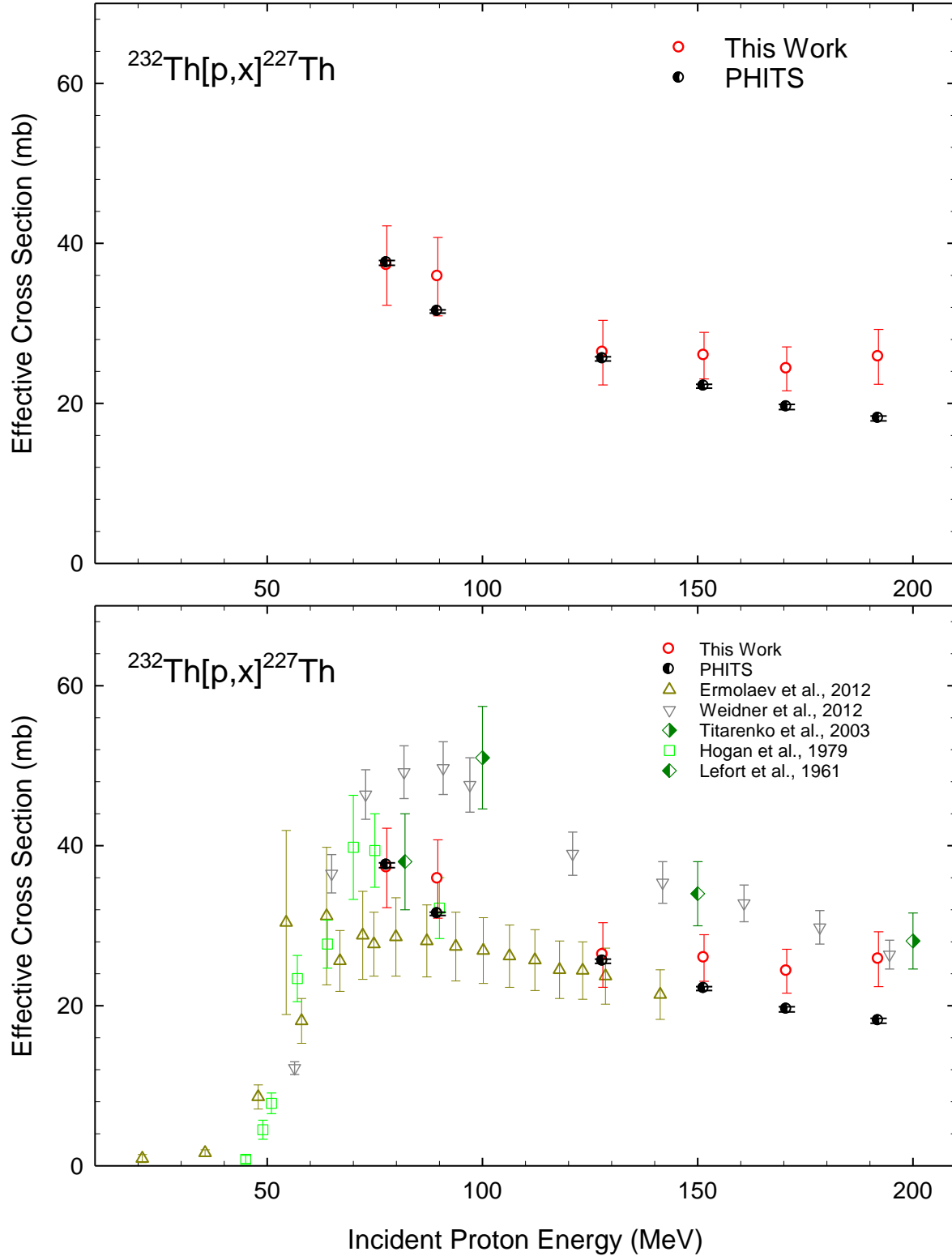
Figure 20. Experimental effective cross sections and cross sections computed with PHITS for the ^{232}Th[p,x]^{227}Th reaction from 77 to 192 MeV (upper plot). Literature values for the same reaction are shown as a comparison in the lower plot.
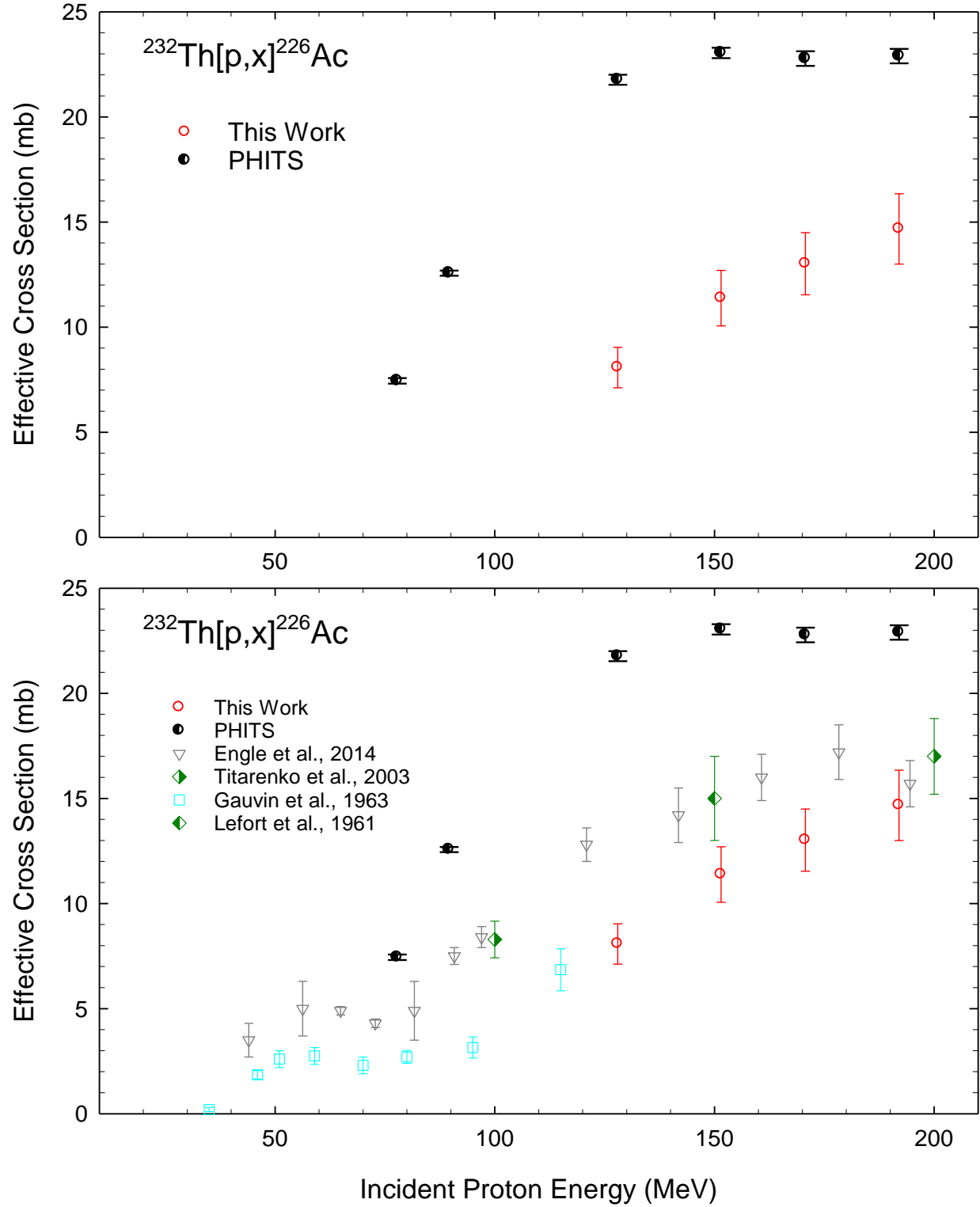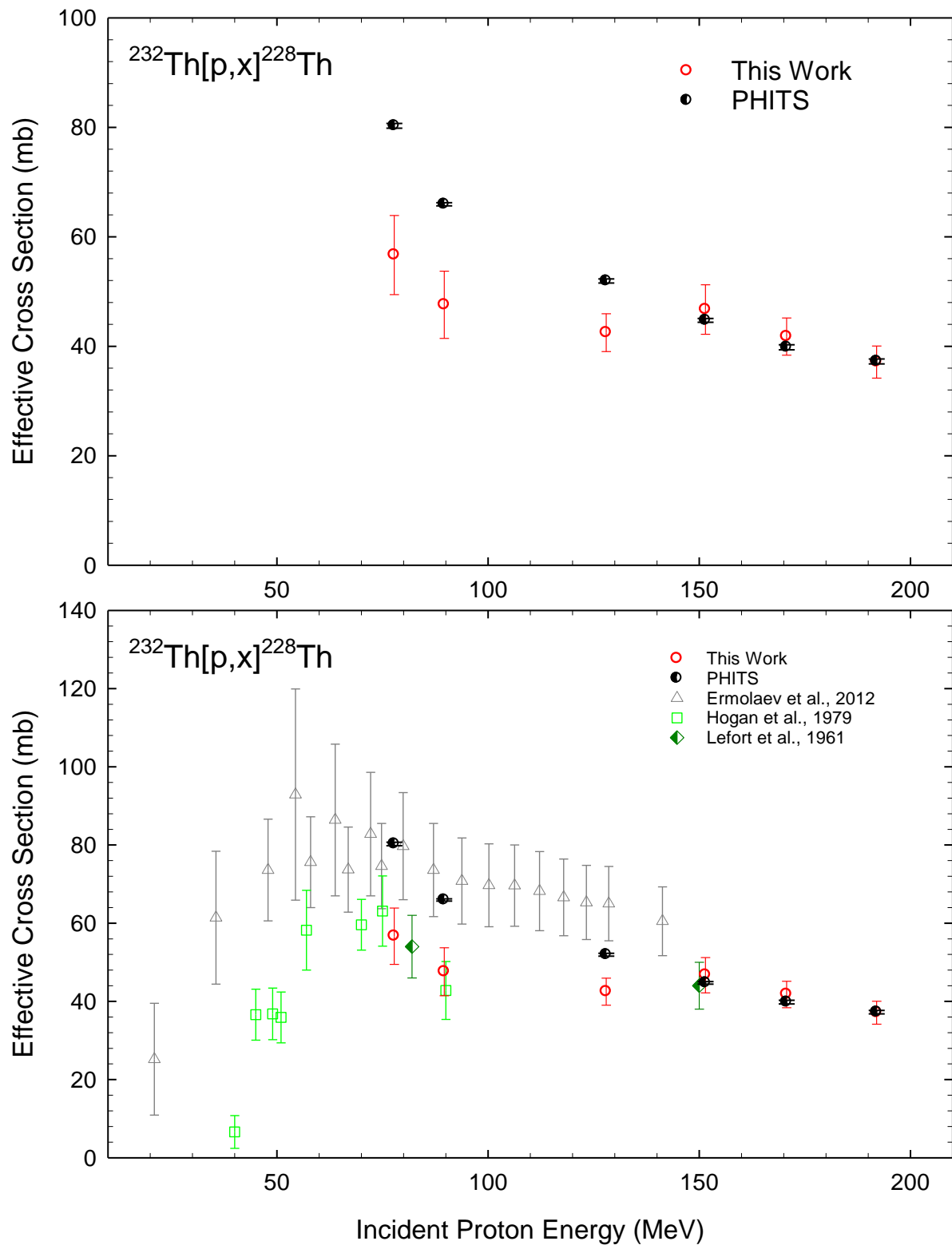
Figure 21. Experimental effective cross sections and cross sections computed with PHITS for the ^{232}Th[p,x]^{228}Th reaction from 77 to 192 MeV (upper plot). Literature values for the same reaction are shown as a comparison in the lower plot.

measured cross section values for this reaction are mirrored almost exactly by the PHITS simulated cross sections with the simulated cross sections only dipping slightly at the higher energies.

Cross sections measured here for the ^{232}Th[p,x]^{227}Th reaction agree with the data reported by Lefort *et al.* [52] and Hogan *et al.* [54] at lower energies (below 100 MeV, Figure 20). Weidner *et al.*[23] reported a slightly higher value at the lower energies, while Ermolaev *et al.* [49] reported a marginally lower value. Comparable to the cross sections reported in this work, it is important to note that the cross sections reported by Ermolaev *et al.* [49] do not represent "thin target" cross sections as the target thickness was ~50 mg cm^{-2} in this experiment. Cross sections reported here are slightly lower than literature values in the 125 to 180 MeV range. The contribution of ^{227}Ac decay to the cumulative cross section of ^{227}Th in the reaction is negligible due to the substantial difference in half-lives of these radionuclei. However, the decay of ^{227}Pa (EC = 15%, $t_{1/2}$ = 38.3 m) does add to the cumulative cross section.

The cross section for the ^{232}Th[p,x]^{228}Th reaction decreases from 56.7 ± 7.2 mb to 37.1 ± 3.1 mb at 77 and 192 MeV respectively. Simulated cross sections for this reaction are in relatively good agreement but tend to have a closer agreement at the higher energies (E_p > 153 MeV).

As shown in Figure 21, data sets of previous cross section measurements for the ^{232}Th[p,x]^{228}Th reaction in the displayed energy range vary substantially — especially in the energy range of this work (70 to 200 MeV). Similar to the quantification of ^{227}Ac, ^{228}Th required a cool-off period to be accurately quantified in the target solution. Thorium-228 emits only weak γ-rays; therefore, the daughter products ^{224}Ra ($t_{1/2}$ = 3.63 d) and ^{212}Pb ($t_{1/2}$ = 10.6 h) must be

utilized to accurately measure the activity of ^{228}Th. Since some ^{224}Ra was generated directly in the target, a sample of the target solution was allowed to decay for >30 days post EOB before assay for ^{224}Ra/^{212}Bi activity. In practice, the decay period was often longer than 30 days to facilitate the detection of other long-lived isotopes such as ^{227}Ac and ^{144}Ce ($t_{1/2}$ = 285.0 d). The cross sections measured in this work for the ^{232}Th[p,x]^{228}Th reaction are in good agreement with the literature values (Figure 21). This cumulative reaction cross section includes significant contributions from the decays of ^{228}Pa (EC = 98.15%, $t_{1/2}$ = 22.4 h) and ^{228}Ac (β^- = 98.15%, $t_{1/2}$ = 6.15 h). A comparison of the cross-sections of ^{232}Th[p,x]^{228}Th and ^{232}Th[p,x]^{227}Th reactions (Figure 20 and Figure 21), clearly indicates the effect of ejecting one additional nucleon from the target nucleus as the threshold energy for the ^{232}Th[p,x]^{228}Th reaction is ~10 MeV lower than the threshold for the ^{232}Th[p,x]^{227}Th reaction. Further, the magnitude of the cross section for the ^{232}Th[p,x]^{228}Th reaction is higher by about a factor of two. This effect is not, however, apparent for the series of ^{232}Th[p,x]^{225,226,227}Ac reactions (Figure 16-Figure 18).

Of the other thorium isotopes produced in these experiments but not reported here, only ^{231}Th is realistically detectable via γ-ray spectroscopy. Unfortunately, the principal γ-ray emission for ^{231}Th is a low-energy, low-intensity photon in the X-ray region (84.2 keV, 6.6%). Because of the complex γ-ray spectra generated by the irradiated foil, distinguishing this emission from background was not possible. Very small quantities of ^{229}Th ($t_{1/2}$ = 7932 y) and ^{230}Th ($t_{1/2}$ = 75,400 y) are also likely generated in these irradiations, but their long half-lives and hence small irradiation yields make quantification by γ-ray spectroscopy impractical.

Overall agreement between the PHITS simulated cross sections and the experimental cross sections for the ^{232}Th[p,x]^{228}Th and the ^{232}Th[p,x]^{228}Th reactions is clear. This strongly contrasts when comparing the relative agreement between measured and simulated cross sections for the

^{232}Th[p,x]^{225,226,227}Ac reactions. Although the current PHITS simulation does not provide the exact nuclear reaction channel for each radionuclide produced, it is likely that the reported thorium isotopes were generated primarily in the ^{232}Th[p,6n]^{227}Pa(EC,38.3m)→^{227}Th and the ^{232}Th[p,5n]^{228}Pa(EC,22.4h)→^{228}Th reactions. However, for the ^{232}Th[p,x]^{225,226,227}Ac reactions, the preferred reaction pathway at these incident proton energies is not well known. For reference, possible reaction pathways are included in Table 4. This may contribute to the otherwise unexplained discrepancies between the PHITS simulated cross sections and the experimentally measured cross sections for these reactions.

3.4   Selected Fission Products: ^{232}Th[p,f]^{99}Mo, ^{140}Ba, and ^{139,141,143,144}Ce reactions

Experimentally measured cross sections, PHITS simulated cross sections, and the relevant literature comparisons are shown in Figure 22-Figure 27 for proton-induced fission of Th. Reported cross sections include: ^{232}Th[p,f]^{99}Mo, ^{232}Th[p,f]^{140}Ba, and ^{232}Th[p,f]^{139,141,143,144}Ce reactions.

The excitation function for the ^{232}Th[p,f]^{99}Mo reaction remains relatively constant and varies only within uncertainty limits ranging from 36.3 ± 3.4 mb to 25.8 ± 3.4 mb (Figure 22). The cross sections for this reaction in the 77 to 92 and 120 to 180 MeV energy range are reported for the first time (Figure 22). The PHITS simulated cumulative cross section for ^{99}Mo closely agrees with the measured cross sections and includes the following contributions from the β^- decay of the A = 99 isobars: ^{99}Rb ($t_{1/2}$ = 54 ms), ^{99}Sr ($t_{1/2}$ = 0.27 s), ^{99}Y ($t_{1/2}$ = 1.5 s), ^{99}Zr ($t_{1/2}$ = 2.1 s), and ^{99}Nb ($t_{1/2}$ = 15.0 s).

The measured cross sections for the ^{232}Th[p,f]^{140}Ba reaction decrease continuously from a maximum value of 14.2 ± 1.8 mb at E_p = 77 MeV to 5.2 ± 1.1 mb at E_p = 192 MeV (Figure 23).
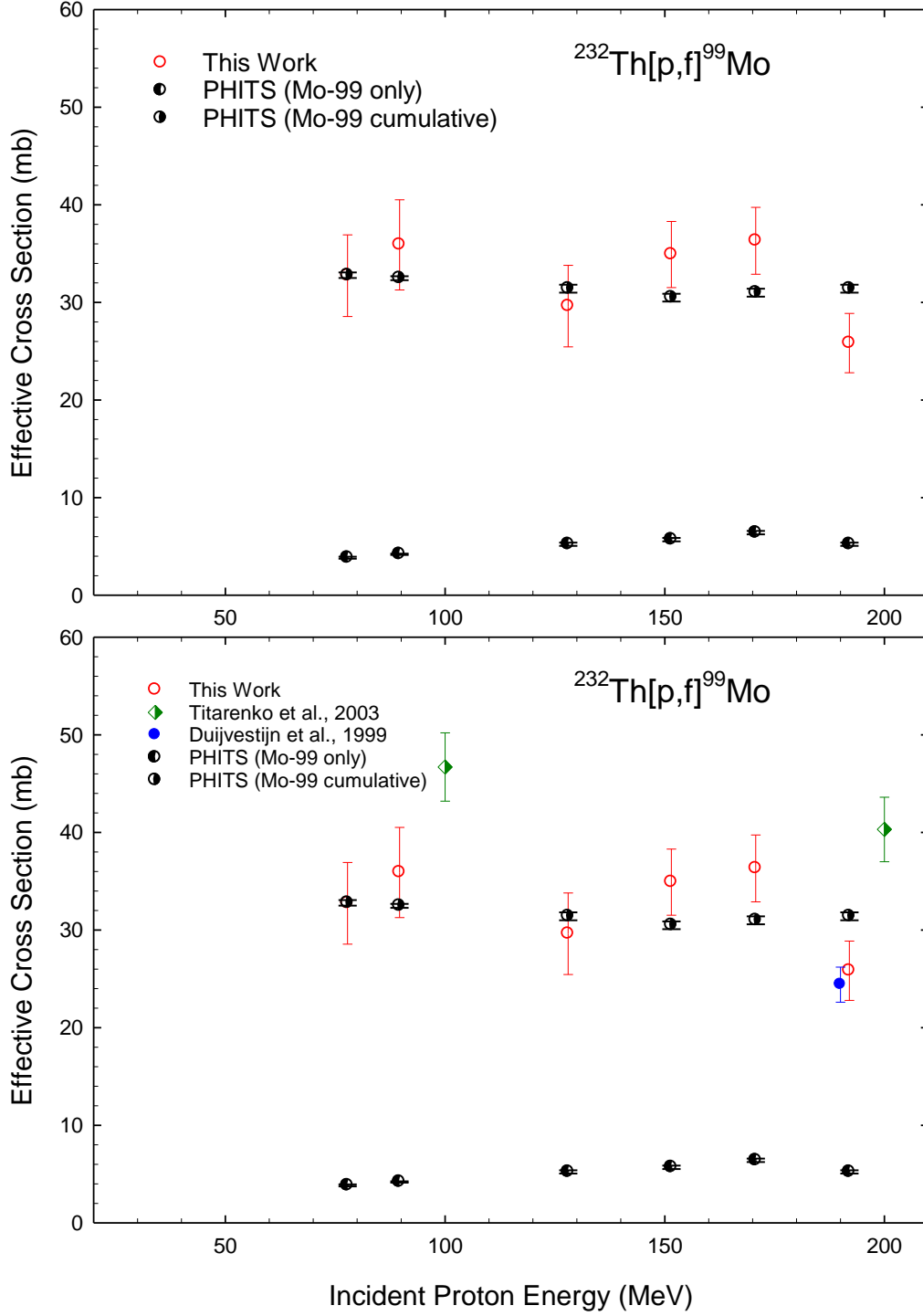
Figure 22. Experimental effective cross sections and cross sections computed with PHITS for the $^{232}Th[p,f]^{99}Mo$ reaction from 77 to 192 MeV (upper plot). The plotted PHITS cross sections include the independent and cumulative cross sections. Literature values for the same reaction are shown as a comparison in the lower plot.
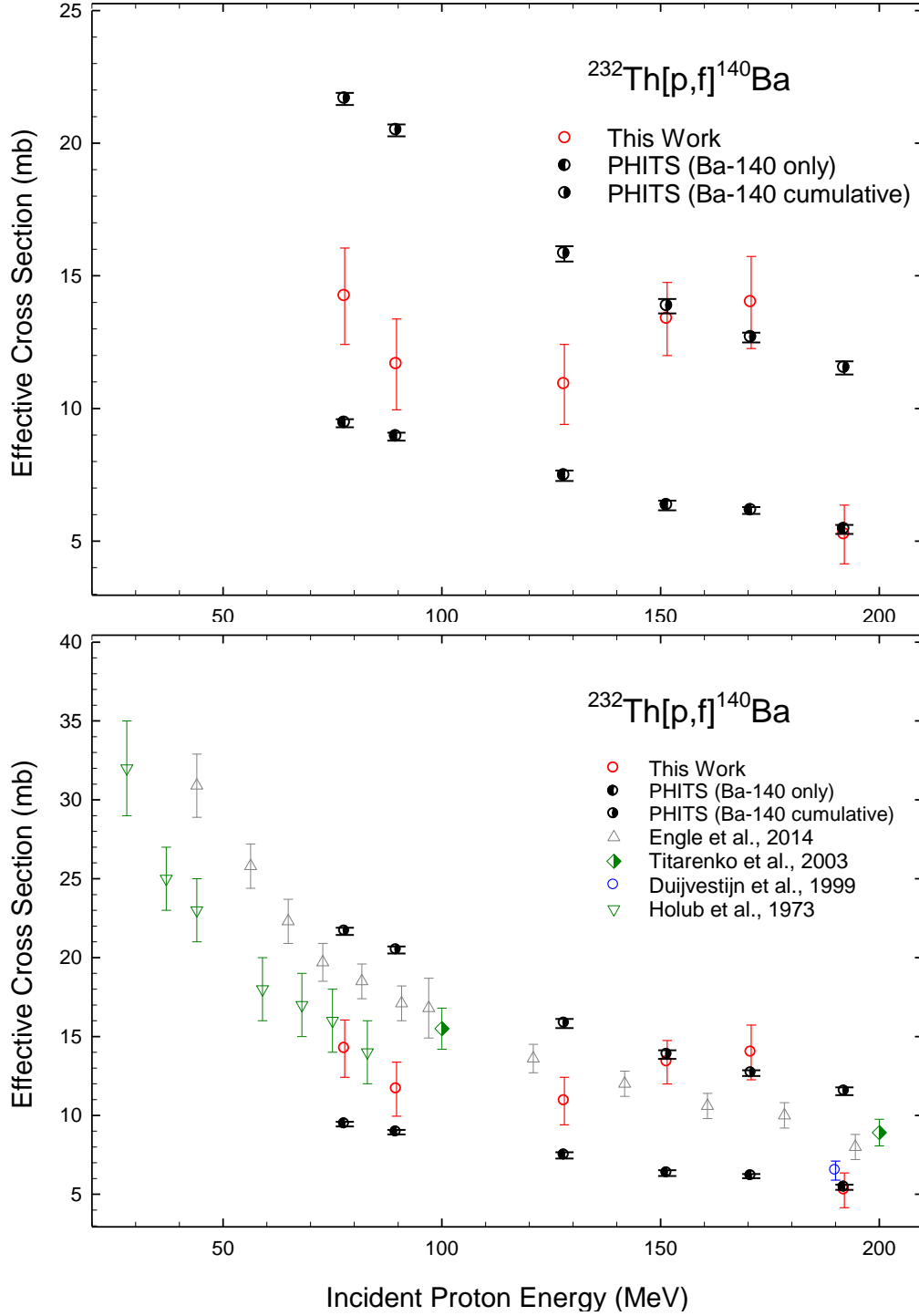
Figure 23. Experimental effective cross sections and cross sections computed with PHITS for the ^{232}Th[p,f]^{140}Ba reaction from 77 to 192 MeV (upper plot). The plotted PHITS cross sections include the independent and cumulative cross sections. Literature values for the same reaction are shown as a comparison in the lower plot.

Previously reported reaction cross sections for the ^{232}Th[p,f]^{140}Ba reaction are in excellent agreement with the cross sections reported here (Figure 23) [50, 53, 55, 56]. However, some of the cumulative simulated cross sections differ by about a factor of two. Cumulative cross section for ^{140}Ba includes the following β^- decay A = 140 isobar contributors: ^{140}I (t$_{1/2}$ = 0.86 s), ^{140}Xe (t$_{1/2}$ = 13.6 s), and ^{140}Cs (t$_{1/2}$ = 63.7 s).

As with the other long-lived nuclides mentioned previously, several of the cerium isotopes required a cool-off period for the background to subside so that the photopeaks could be measured accurately. Cerium-139 (t$_{1/2}$ = 137.6 d), ^{141}Ce (t$_{1/2}$ = 32.5 d), and ^{144}Ce were assayed in the target solution at least 90 days post EOB. With the exception of the ^{232}Th[p,f]^{139}Ce reaction, the cross sections for all of the reported ^{232}Th[p,f]Ce reactions decrease almost linearly with increasing incident proton energy (Figure 24-Figure 27).

When comparing with the results from Engle *et al.* [53], the cross sections measured in this work for the ^{232}Th[p,f]^{139}Ce reaction are in good agreement except for measurements at 128 MeV, where the results differ by a factor >2 (Figure 24). Again, this large discrepancy is likely due to the difficulty in measuring long-lived radioisotopes in the presence of many short-lived radionuclides via γ-ray spectroscopy. The cumulative simulated cross section for ^{139}Ce includes the isobars ^{139}Nd (t$_{1/2}$ = 29.7 m) and ^{139}Pr (t$_{1/2}$ = 4.4 h) that decay via electron capture. However, as seen in Figure 24, the contribution from these precursors is almost negligible as the cumulative and independent cross sections are nearly equivalent. This is the only instance in this work where the measured excitation function is consistently higher than the PHITS simulated excitation function.
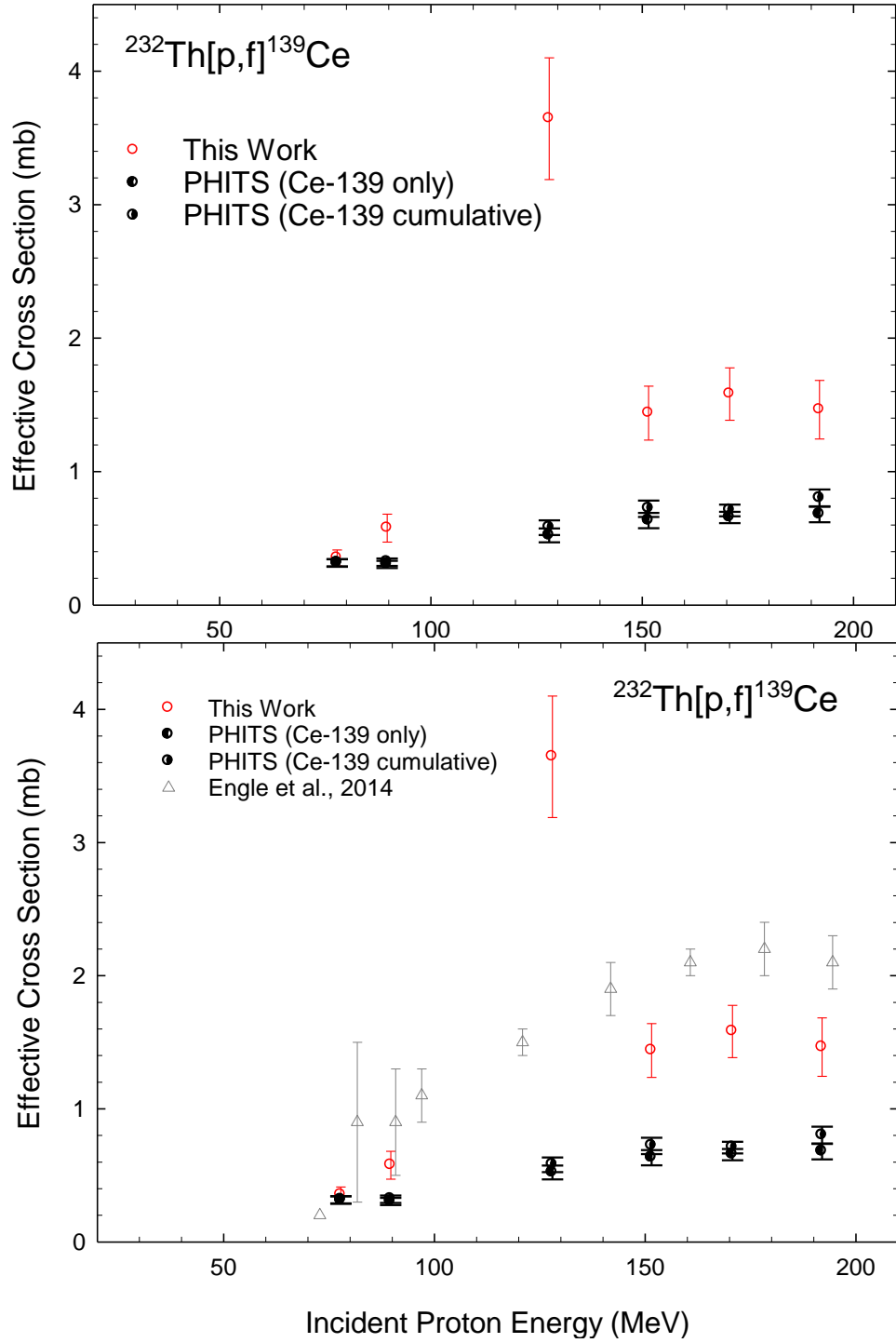
Figure 24. Experimental effective cross sections and cross sections computed with PHITS for the ^{232}Th[p,f]^{139}Ce reaction from 77 to 192 MeV (upper plot). The plotted PHITS cross sections include the independent and cumulative cross sections. Literature values for the same reaction are shown as a comparison in the lower plot.

Cross sections for the ^{232}Th[p,f]^{141}Ce reaction are generally lower than the most recent published values [50, 53] and slightly lower than the simulated cross sections (Figure 25). The cumulative simulated cross section for ^{141}Ce includes contributions from the A = 141 isobars ^{141}Cs ($t_{1/2}$ = 24.8 s), ^{141}Ba ($t_{1/2}$ = 18.2 m), and ^{141}La ($t_{1/2}$ = 3.9 h).

The values reported here for the ^{232}Th[p,f]^{143}Ce and ^{232}Th[p,f]^{144}Ce reactions also agree consistently with the literature data, except in the case of the 128 MeV cross section of ^{143}Ce where the data reported here are lower by a factor >2 than the measured cross section reported earlier [53] (Figure 26). These excitation functions also agree relatively well in shape and magnitude with the simulated cross sections. As with all of the other excitation functions reported in this work, excluding those for the production ^{139}Ce, the simulated cross sections were slightly higher in magnitude than the experimentally measured cross sections. The cumulative simulation cross section for ^{143}Ce includes the following β$^-$ decay A = 143 isobars: ^{143}Cs ($t_{1/2}$ = 1.8 s), ^{143}Ba ($t_{1/2}$ = 14.5 s), and ^{143}La ($t_{1/2}$ = 14.2 m). β$^-$ decay A = 144 isobars for the ^{232}Th[p,f]^{144}Ce reaction included ^{144}Cs ($t_{1/2}$ = 1.0 s), ^{144}Ba ($t_{1/2}$ = 11.5 s), and ^{144}La ($t_{1/2}$ = 40.8 s) (Figure 27).

As indicated, while cross sections for ^{232}Th[p,f]$^{141, 143, 144}$Ce reactions decrease with increasing incident proton energy, the cross section for ^{232}Th[p,f]^{139}Ce reaction increases with incident proton energy. An explanation for this may relate to the fact that ^{141}Ce, ^{143}Ce, and ^{144}Ce are neutron-rich nuclei, decaying with β$^-$ emission, while ^{139}Ce is proton-rich and decays via electron capture. It is also interesting to note that PHITS underestimates the production of the proton-rich isotope ^{139}Ce while it slightly overestimates the production of the neutron-rich fission products included in this work.
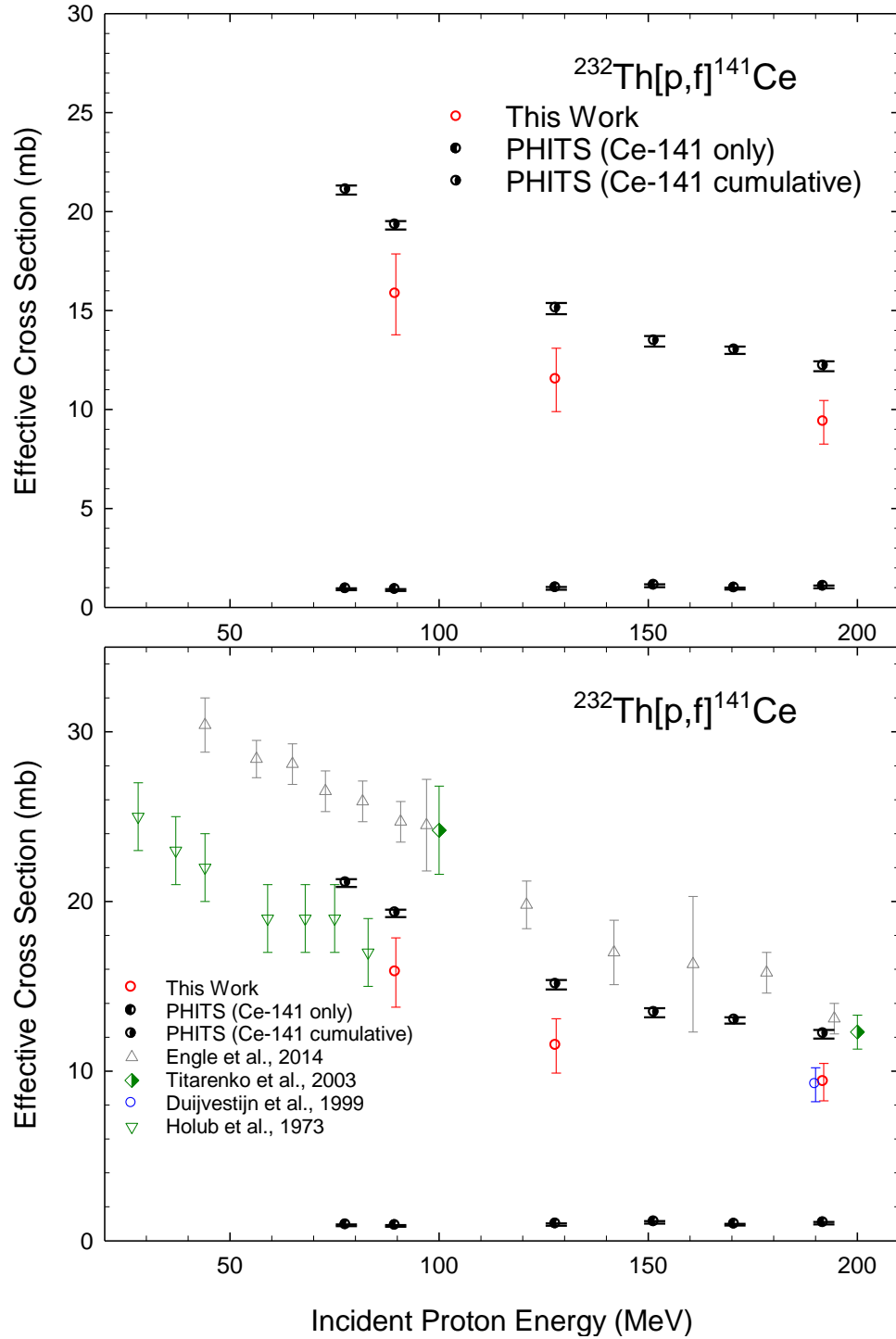
Figure 25. Experimental effective cross sections and cross sections computed with PHITS for the $^{232}Th[p,f]^{141}Ce$ reaction from 77 to 192 MeV (upper plot). The plotted PHITS cross sections include the independent and cumulative cross sections. Literature values for the same reaction are shown as a comparison in the lower plot.
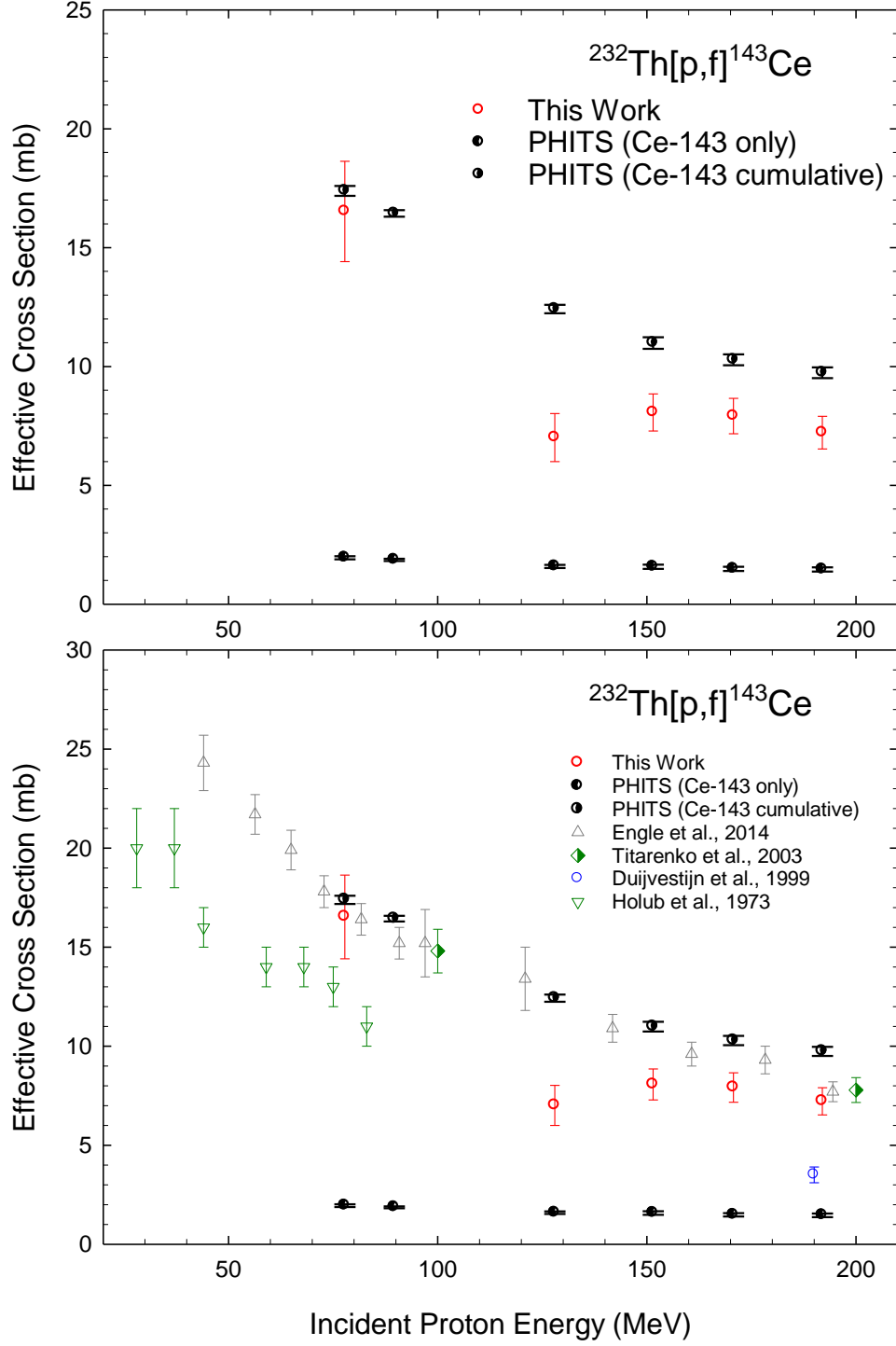
Figure 26. Experimental effective cross sections and cross sections computed with PHITS for the $^{232}Th[p,f]^{143}Ce$ reaction from 77 to 192 MeV (upper plot). The plotted PHITS cross sections include the independent and cumulative cross sections. Literature values for the same reaction are shown as a comparison in the lower plot.
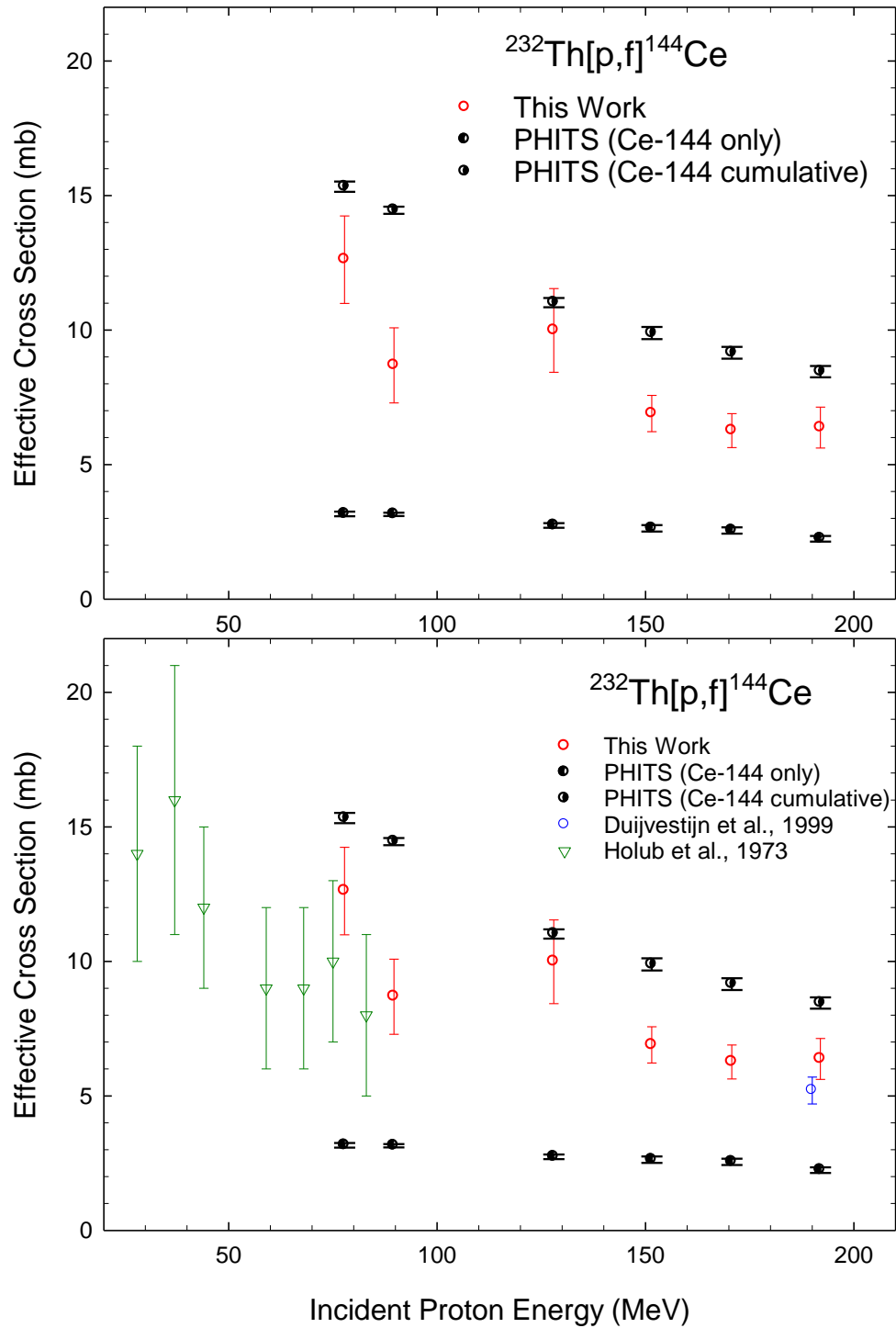
Figure 27. Experimental effective cross sections and cross sections computed with PHITS for the $^{232}Th[p,f]^{144}Ce$ reaction from 77 to 192 MeV (upper plot). The plotted PHITS cross sections include the independent and cumulative cross sections. Literature values for the same reaction are shown as a comparison in the lower plot.

3.5   Projected Yields

From the cross sections presented in this work, yields for the eleven radioisotopes were projected for beam currents and incident proton energies of 250 μA at 90 MeV for IPF and 100 μA at 192 MeV for BLIP for a continuous 10-day irradiation using a 5 g cm^{-2} thorium target. These values are similar to those of the previous irradiations performed (Table 1) except with a much thicker target. Table 11 outlines the calculated yields at EOB. Using the parameters described for IPF, the yield of ^{225}Ac is calculated to be 1.50 Ci with an ^{227}Ac/^{225}Ac ratio of 0.18%, while the total yield of all of the remaining radioisotopes reported here is 30.6 Ci. Using the BLIP irradiation parameters, the yield of ^{225}Ac is calculated to be 1.54 Ci with an ^{227}Ac/^{225}Ac ratio of 0.20%, and the total yield of the others reported is 13.0 Ci.

As indicated in Table 11 and discussed earlier, the projected yields of ^{225}Ac from the two irradiation facilities are very similar despite lower proton current at BLIP relative to IPF. This clearly reflects the fact that the effective cross section for the ^{232}Th[p,x]^{225}Ac reaction increases with increasing incident proton energy from 77 to 192 MeV by a factor of about two (Figure 16). It appears the ratio of ^{227}Ac to ^{225}Ac also remains comparable in both facilities. The physical differences between the two irradiation facilities with regard to proton current and proton energy, however, are responsible for the apparent discrepancy between the projected yield of selected fission products and actinides — excluding ^{225}Ac (summarized in Table 11). The main factor responsible for this is the change in the shape of the corresponding excitation function as a function of energy. A number of additional actinides and hundreds of fission products were also detected over the course of these experiments, but reporting the yields of these additional nuclides is beyond the scope of this work, and will be reported in the future. Accurate quantification of these unreported isotopes, however, would require further chemical separations.

Table 11. Yield calculations (at EOB) for radionuclides reported in this text, based on a 10-day irradiation of a 5 g cm^{-2} Th target.

Radionuclide	IPF Yield (250μA, 90 MeV) (Ci)	BLIP Yield (100μA, 192 MeV) (Ci)
^{225}Ac	1.50	1.54
^{226}Ac	N/M	3.20
^{227}Ac	2.7×10^{-3}	3.1×10^{-3}
^{227}Th	6.28	1.90
^{228}Th	0.22	8.0×10^{-2}
^{99}Mo	18.08	5.40
^{140}Ba (^{140}La)	3.14	0.46
^{139}Ce	1.1×10^{-2}	1.6×10^{-2}
^{141}Ce	1.42	0.35
^{143}Ce	1.38	1.57
^{144}Ce	9.0×10^{-2}	3.3×10^{-2}

[*]N/M = Not measured

3.6   Generator Results

The relevant γ-ray spectra for the each of the ^{225}Ac/^{213}Bi generators that were analyzed are shown in Figure 28-Figure 36. For better clarity, the spectra are broken up into three arbitrary energy ranges for the respective sample. It is important to note that the scale on the y-axis (CPS) decreases as the scale on the x-axis (γ-ray energy) increases. This is necessary because the efficiency of the detector declines dramatically as incident photon energy increases. Since the main goal of this experiment was the determination of the presence of unknown radionuclides on the ^{225}Ac/^{213}Bi generators, CPS in each figure is given as the raw value. In order to quantify each peak for activity, it would need to be corrected for detector efficiency and γ-ray intensity. With that being said, it is still useful to compare relative peak size within each spectrum. As outlined

in the following sections, the only observed peaks are from ^{227}Ac and its associated decay daughters. This validates the effectiveness of the chemical separation scheme employed at ORNL that is described in Section 2.2.

3.6.1   Johns Hopkins University Generator Analysis

The Johns Hopkins University generator was eluted with 6 x 0.5 mL fractions of 0.15M KI/0.1M HCl, and all fractions of the eluant were collected in one vial as described previously. Then the vial was assayed via γ-ray spectroscopy for a set 10 counts, each 10 minutes in length. As expected, the largest peak in each spectrum was the 351 keV (I_γ = 12.8 %) emission from ^{211}Bi.

Figure 28-Figure 30 compose one continuous spectrum resulting from an overnight count that was completed approximately two weeks after the original elution of the JHU generator. The only observed peaks in the overnight spectrum were from a small percentage of ^{227}Ac and its associated decay daughters that had broken through the generator. As the resin ages and more elutions are performed, it is reasonable to expect a larger degree of actinium breakthrough. Higher intensity γ-ray emissions from ^{223}Ra (154 keV, I_γ = 5.6% and 269 keV, I_γ = 13.6%) are the largest photopeaks in the spectrum followed by the largest emission from ^{211}Bi (351 keV, I_γ = 12.8%).
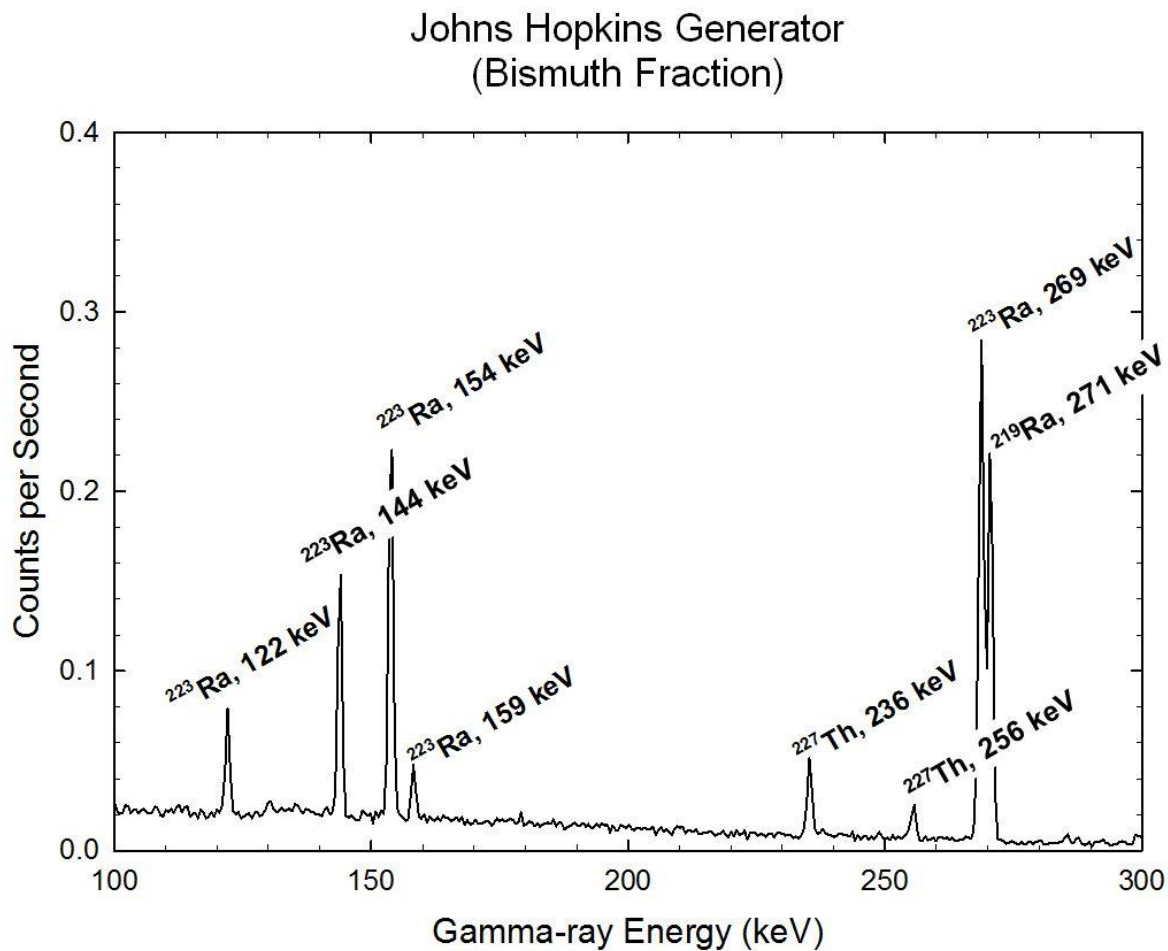
Figure 28. HPGe γ-ray spectrum of the 3 mL 0.15M KI/0.1M HCl elution (bismuth fraction) of the Johns Hopkins Generator 2 weeks after chemical separation (100-300 keV energy range).
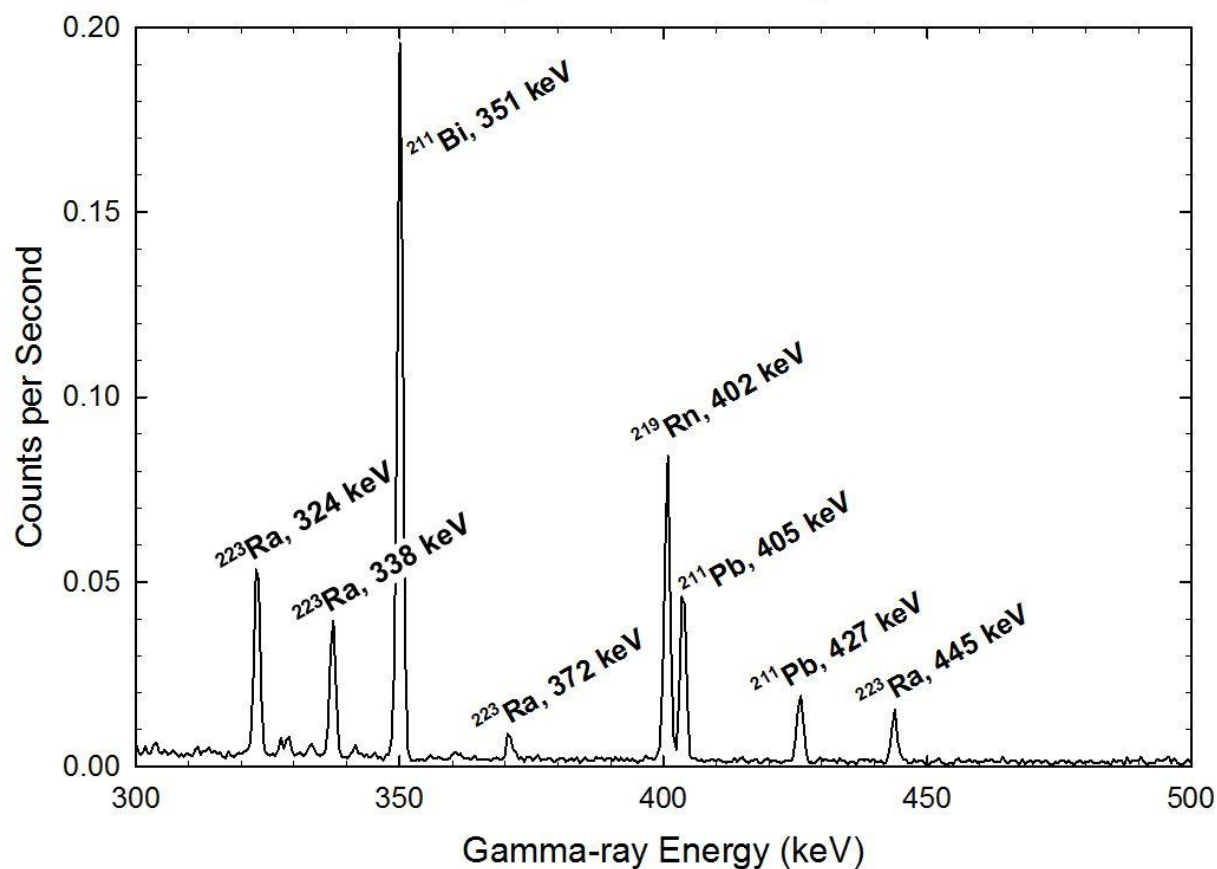
Figure 29. HPGe γ-ray spectrum of the 3 mL 0.15M KI/0.1M HCl elution (bismuth fraction) of the Johns Hopkins Generator 2 weeks after chemical separation (300-500 keV energy range).

Figure 30. HPGe γ-ray spectrum of the 3 mL 0.15M KI/0.1M HCl elution (bismuth fraction) of the Johns Hopkins Generator 2 weeks after chemical separation (500-1000 keV energy range).

3.6.2 Yeshiva University Generator Analysis

Since both of the analyzed generators were constructed in the same fashion and were produced from the same target material, radionuclidic composition was assumed to be identical. This allowed the YU generator to be analyzed in a different manner than the JHU generator. Before any chemical separation, a baseline HPGe γ-ray spectrum of the YU generator was obtained (Figure 31–Figure 33). Many of the same photopeaks are present that were identified in the JHU bismuth fraction. However, it is important to note that the ratio of ^{227}Th peaks to the other decay daughters is greatly increased compared to the spectrum of the JHU bismuth fraction. This reflects the fact that all of the ^{227}Ac daughter products are in full secular equilibrium with the ^{227}Ac precursor. This is unlike the observed spectra from the ^{211}Bi fraction where the shorter-lived daughter products (^{223}Ra and ^{211}Bi) are growing in at a much faster rate than the longer-lived ^{227}Th.

Using 6M HNO_3, all of the nuclides that compose the ^{227}Ac decay chain shown in Figure 14 were eluted from the YU generator with the exception of ^{227}Th. This elution was set aside and the YU generator was assayed overnight (15 hours) via γ-ray spectroscopy. The resulting spectrum is shown in Figure 34–Figure 36.

After the elution of the other daughter products, the 236 keV γ-ray emission from ^{227}Th is clearly the largest photopeak in the spectrum. It is important to note that the detector geometry was different in the spectrum shown in Figure 31–Figure 33 than the detector geometry in the spectrum shown in Figure 34–Figure 36. Small amounts of ingrowth from ^{223}Ra, ^{219}Bi and ^{211}Bi are also visible. However, all peaks in the spectrum can easily be identified as emissions from the ^{227}Ac decay chain. This corroborates the data shown in Figure 28–Figure 30 where all γ-ray emissions are attributed to decay daughters of ^{227}Ac.
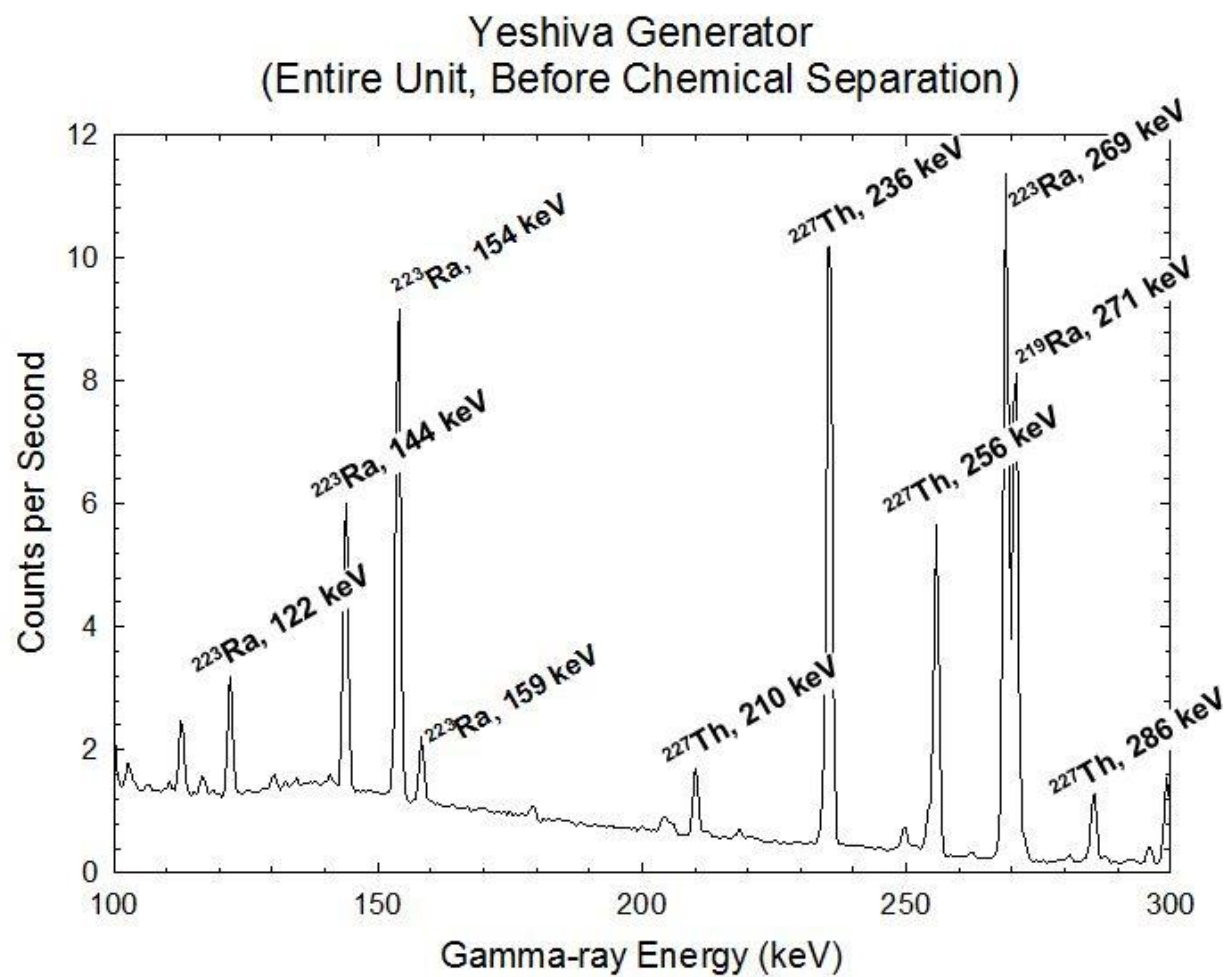
73

Figure 31. HPGe γ-ray spectrum of Yeshiva Generator before any chemical separation (100-300 keV energy range).
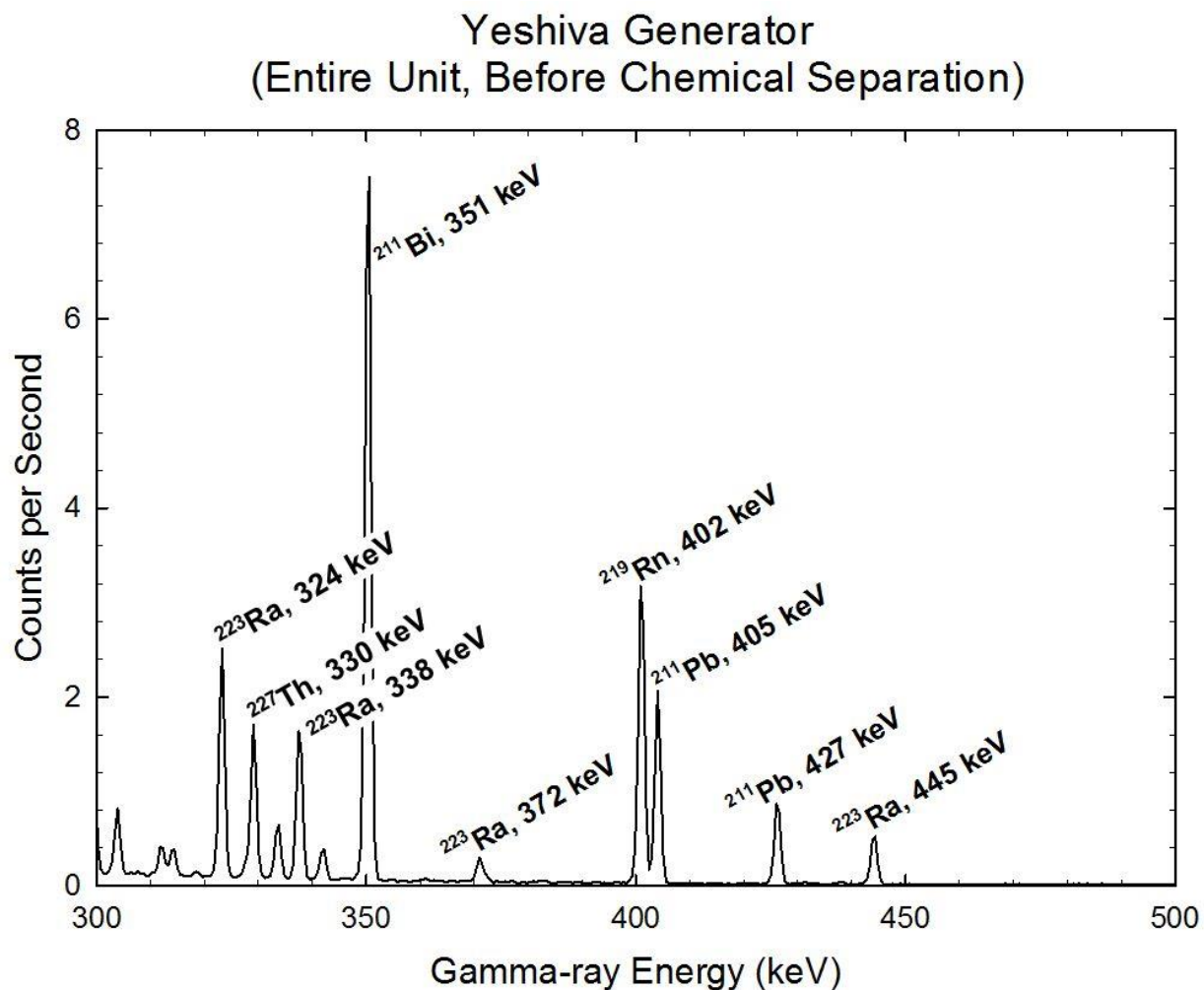
Figure 32. HPGe γ-ray spectrum of Yeshiva Generator before any chemical separation (300-500 keV energy range).
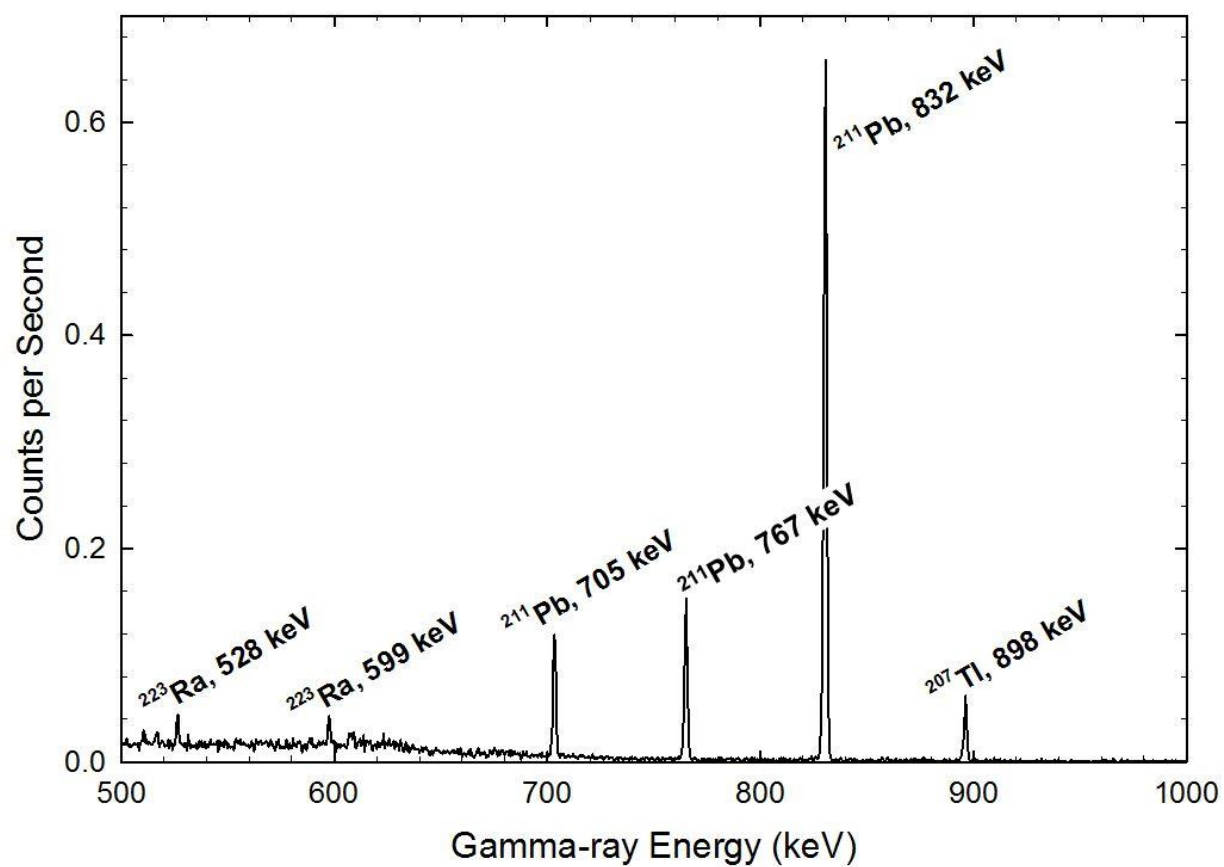
Figure 33. HPGe γ-ray spectrum of Yeshiva Generator before any chemical separation (500-1000 keV energy range).
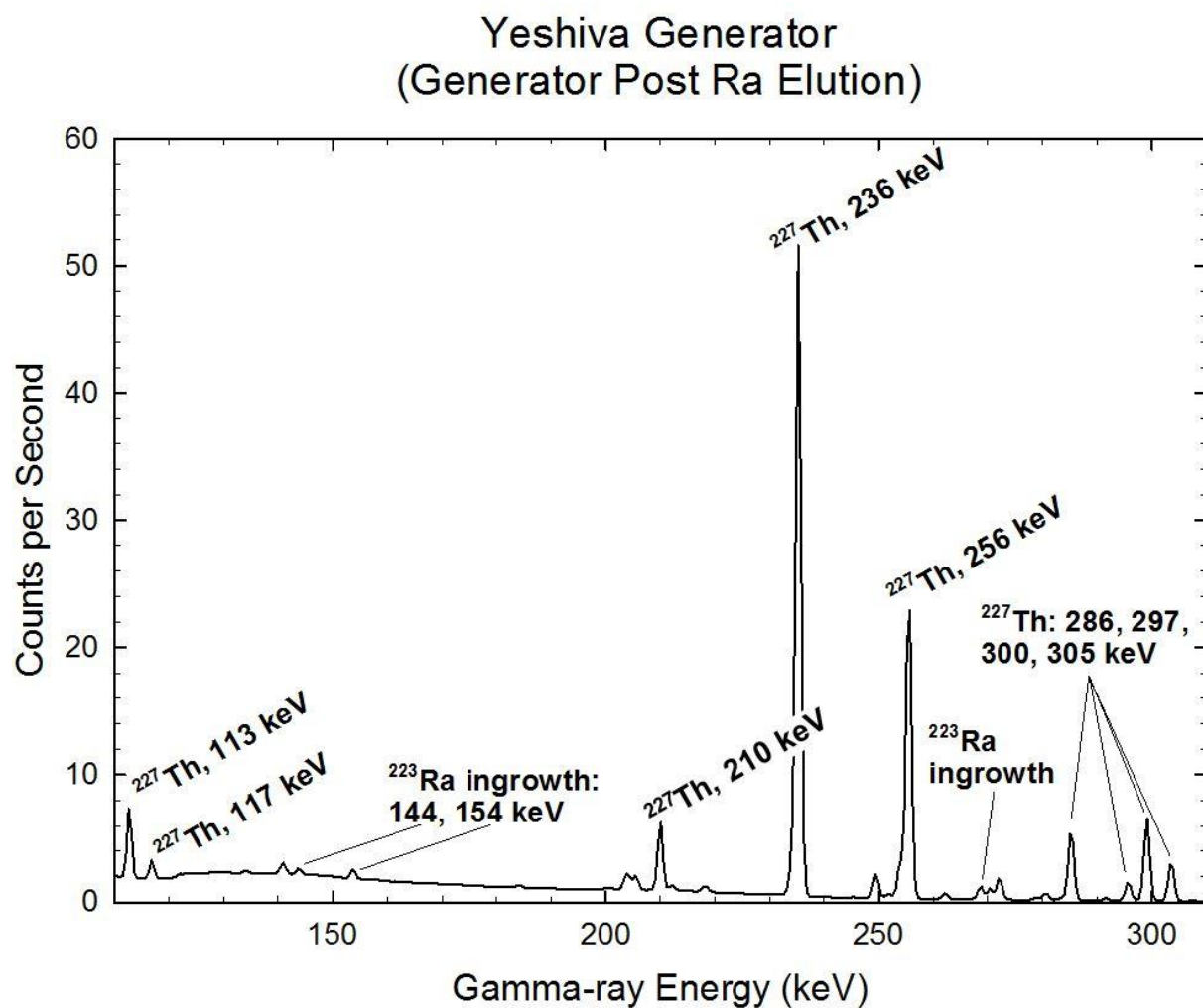
Figure 34. HPGe γ-ray spectrum of Yeshiva Generator after elution of Ra with 6M HNO₃ (100-320 keV energy range).
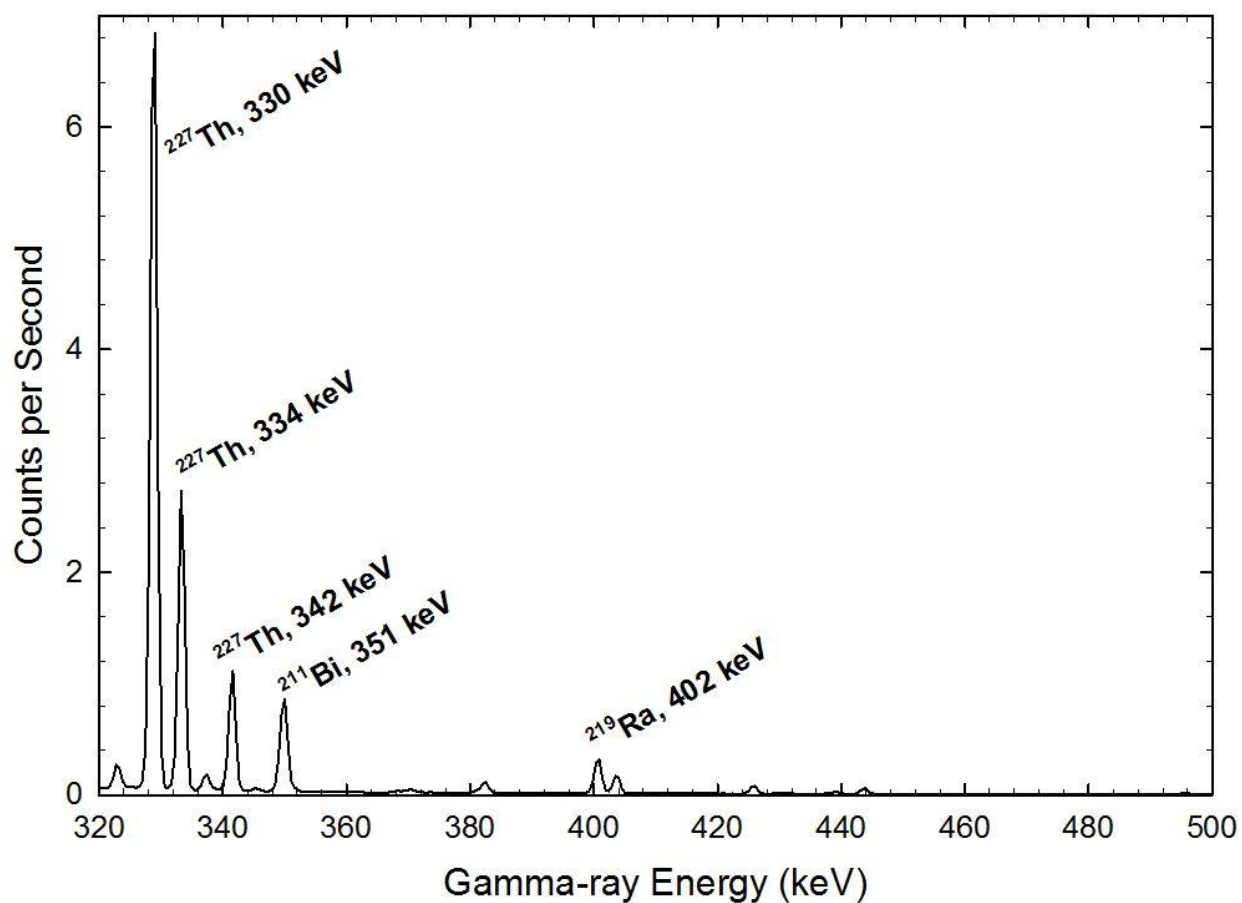
Figure 35. HPGe γ-ray spectrum of Yeshiva Generator after elution of Ra with 6M HNO₃ (320-500 keV energy range).
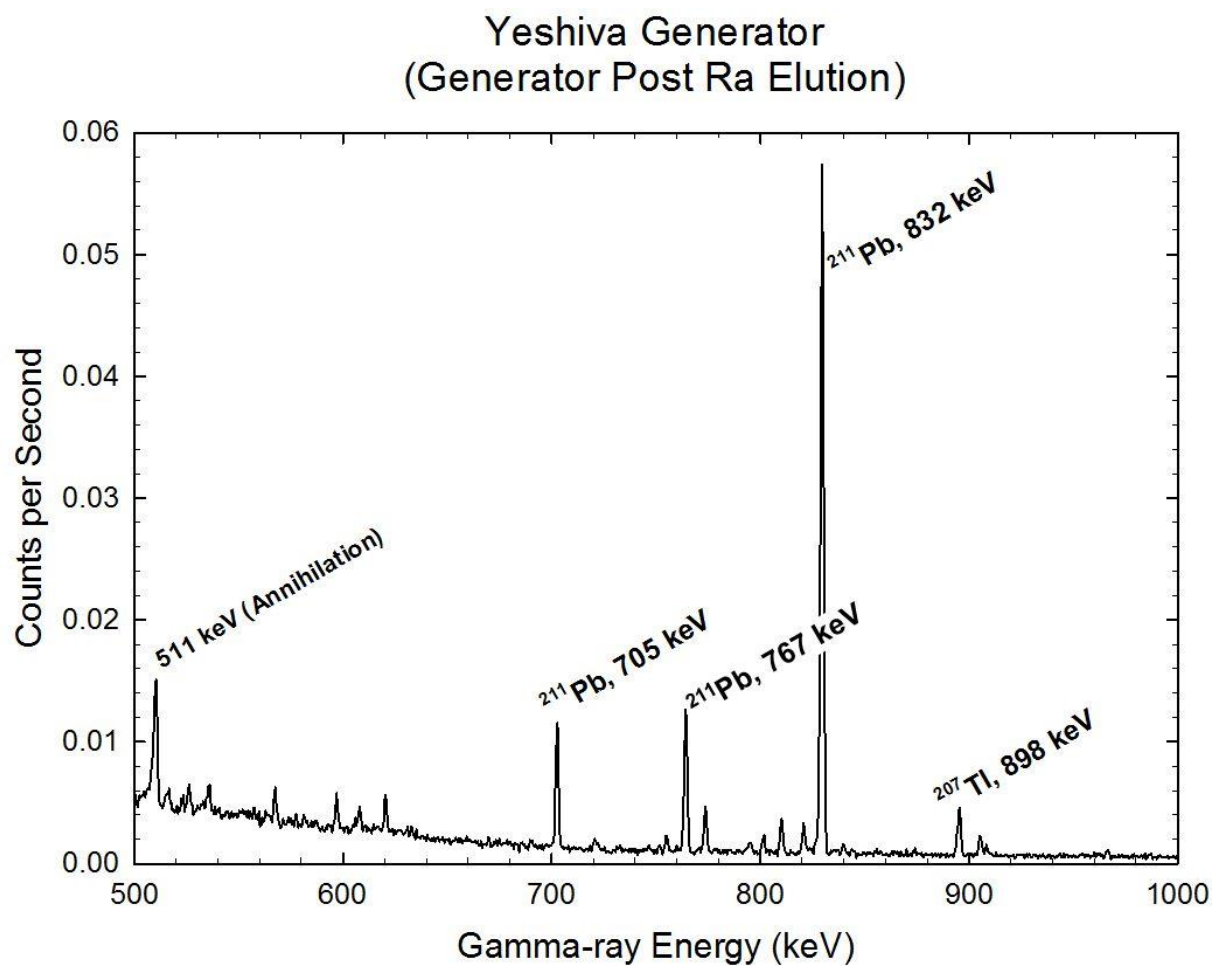
Figure 36. HPGe γ-ray spectrum of Yeshiva Generator after elution of Ra with 6M HNO₃ (500-1000 keV energy range).

4   Conclusion and Future Work

Measured cross sections are reported for eleven isotopes of actinium, thorium, molybdenum, barium, and cerium. This data set validates previously reported measurements for many of these isotopes, and greatly expands the data available for other reaction cross sections such as that for ^{99}Mo. The ^{232}Th[p,f]^{144}Ce reaction cross section between 83 and 192 MeV is reported here for the first time. Generally, PHITS simulated cross sections exhibited a close agreement to the experimentally measured cross sections. However, simulated cross sections for the ^{232}Th[p,x]Ac reactions consistently differed from the experimental data by a factor of two. As documented, curie quantities of ^{225}Ac can be produced in a ten-day irradiation of a 5 g cm^{-2} thorium target at either LANL-IPF or BNL-BLIP at proton energies between 77 and 192 MeV and proton intensities from 100 to 250 μA.

The first in-depth study of the long-lived radiocontaminants of ^{225}Ac/^{213}Bi generators produced through the high-energy proton irradiation of ^{232}Th has been performed. After thorough analysis of the bismuth fraction eluted from the generator by a method commonly used in the nuclear medicine field, no unknown radiocontaminants were observed. Only a small fraction of breakthrough ^{227}Ac and its decay products were present. Similar results were obtained through the 6 M HNO$_3$ elution of the generator; revealing only ^{227}Ac and ^{227}Th. Mass spectrometry analysis on future ^{225}Ac/^{213}Bi generators could reveal the presence of unknown contaminants, but this analysis may only confirm the efficiency of the current ^{225}Ac purification scheme employed at ORNL.

Results achieved with the physical models used in PHITS can be compared to an equivalent MCNP or GEANT4 analysis, further validating the efficacy of these useful simulation tools. In

addition, a radioactive decay and target burnup component could be added to PHITS to allow for a more accurate comparison with the effective cross sections measured in these experiments.

Although easily separable from ^{225}Ac through ion exchange chromatography, ^{233}Pa is one of the highest activity contaminants produced in the high-energy proton irradiation of ^{232}Th and can cause shipping limitations. The exact nuclear reaction pathway that produces this radionuclide is currently unknown but two possible pathways include the ^{232}Th$[p,\gamma]^{233}$Pa reaction or the ^{232}Th$[n,\gamma]^{233}$Th $(\beta^-)\rightarrow^{233}$Pa. However, both of these pathways are unlikely at high incident proton energies. If a small thorium foil were irradiated behind a thicker thorium foil and a higher specific activity of ^{233}Pa was observed in the smaller foil, a case could be made that the main nuclear pathway for the production of ^{233}Pa is through the absorption of secondary neutrons.

All data presented here will aid in the development of future irradiations of thorium and subsequent chemical purifications of ^{225}Ac on a production scale for medical applications in targeted alpha radioimmunotherapy.

List of References

1.   Essler, M., et al., Therapeutic efficacy and toxicity of [225]Ac-labelled vs. [213]Bi-labelled tumour-homing peptides in a preclinical mouse model of peritoneal carcinomatosis. European Journal of Nuclear Medicine and Molecular Imaging, 2012. **39**(4): p. 602-612.

2.   Morgenstern, A., F. Bruchertseifer, and C. Apostolidis, Bismuth-213 and Actinium-225 - Generator Performance and Evolving Therapeutic Applications of Two Generator-Derived Alpha-Emitting Radioisotopes. Current Radiopharmaceuticals, 2012. **5**(3): p. 221-227.

3.   Miederer, M., D.A. Scheinberg, and M.R. McDevitt, Realizing the potential of the Actinium-225 radionuclide generator in targeted alpha particle therapy applications. Advanced Drug Delivery Reviews, 2008. **60**(12): p. 1371-1382.

4.   Mulvey, J.J., et al., Self-assembly of carbon nanotubes and antibodies on tumours for targeted amplified delivery. Nat Nano, 2013. **8**(10): p. 763-771.

5.   NSAC. Meeting Isotope Needs and Capturing Opportunities for the Future: The 2015 Long Range Plan for the DOE-NP Isotope Program. 2015. NSAC Isotopes Subcommittee.

6.   McDevitt, M.R., et al., Radioimmunotherapy with alpha-emitting nuclides. European Journal of Nuclear Medicine, 1998. **25**(9): p. 1341-1351.

7.   Jurcic, J.G. and T.L. Rosenblat, Targeted alpha-particle immunotherapy for acute myeloid leukemia. American Society of Clinical Oncology educational book / ASCO. American Society of Clinical Oncology. Meeting, 2014: p. e126-31.

8.   McDevitt, M.R., et al., Tumor Therapy with Targeted Atomic Nanogenerators. Science, 2001. **294**(5546): p. 1537-1540.

9.   Brechbiel, M.W., Targeted α-therapy: past, present, future? Dalton Transactions, 2007(43): p. 4918-4928.

10.   McLaughlin, M.F., et al., Gold Coated Lanthanide Phosphate Nanoparticles for Targeted Alpha Generator Radiotherapy. PLOS One, 2013.

11.   IAEA. Technical Meeting on Alpha emitting radionuclides and radiopharmaceuticals for therapy. 2013.

12.   Jost, C.U., et al., Measurement of cross sections for the [232]Th(P,4n)[229]Pa reaction at low proton energies. AIP Conference Proceedings: International Conference on Application of Accelerators in Research and Industry, 2013. **1525**(1): p. 520-524.

13.   Boll, R.A., M.A. Garland, and S. Mirzadeh. Production of Thorium-229 at the ORNL High Flux Isotope Reactor. in ANS Annual Meeting: Isotopes for Medicine and Industry. 2008. Anaheim, CA: ANS.

14.   Hogle, S., et al., Reactor production of Thorium-229. Applied Radiation and Isotopes, 2016. **114**: p. 19-27.

15.   Apostolidis, C., et al., Cyclotron production of Ac-225 for targeted alpha therapy. Applied Radiation and Isotopes, 2005. **62**(3): p. 383-387.

16.   Melville, G., et al., Production of Ac-225 for cancer therapy by photon-induced transmutation of Ra-226. Applied Radiation and Isotopes, 2007. **65**(9): p. 1014-1022.

17.   Ghoshal, S.N., An Experimental Verification of the Theory of Compound Nucleus. Physical Review, 1950. **80**(6): p. 939-942.

18.   Friedlander, G., et al., Nuclear and Radiochemistry. 3rd ed. 1981, New York: John Wiley & Sons, Inc.

19.   Russell, G.J. Spallation Physics - An Overview. in International Collaboration on Advanced Neutron Sources. 1990. Tsukuba.

20.   Knoll, G.F., Radiation Detection and Measurement. 4th ed. 2010, Hoboken, NJ: John Wiley & Sons, Inc.

21.   Eriksson, M., Reliability Assessment of the LANSCE Accelerator System, in Nuclear and Reactor Physics. 1998, Royal Institute of Technology: Stockholm.

22.   Johnson, K.F., et al. Commissioning and Initial Operation of the Isotope Production Facility at the Los Alamos Neutron Science Center (LANSCE). in 9th European Particle Accelerator Conference. 2004. Lucerne.

23.   Weidner, J.W., et al., Proton-induced cross sections relevant to production of ^{225}Ac and ^{223}Ra in natural thorium targets below 200 MeV. Applied Radiation and Isotopes, 2012. **70**(11): p. 2602-2607.

24.   Wheeler, G., et al., The Brookhaven 200 MeV proton linear accelerator. Particle Accelerator, 1979. **9**: p. 1.

25.   Medvedev, D.G., et al., Development of a large scale production of ^{67}Cu from ^{68}Zn at the high energy proton accelerator: Closing the ^{68}Zn cycle. Applied Radiation and Isotopes, 2012. **70**(3): p. 423-429.

26.   Steyn, G.F., et al., Production of ^{52}Fe Via Proton-Induced Reactions on Manganese and Nickel. Applied Radiation and Isotopes, 1990. **41**(3): p. 315-325.

27.   Ziegler, J.F., J.P. Biersack, and U. Littmark, The Stopping and Range of Ions in Solids. 1985, New York: Pergamon Press.

28.   Boll, R.A., D. Malkemus, and S. Mirzadeh, Production of Actinium-225 for alpha particle mediated radioimmunotherapy. Applied Radiation and Isotopes, 2005. **62**(5): p. 667-679.

29.   Mirzadeh, S., Accelerator produced ^{225}Ac via proton spallation of ^{232}Th: a joint research program among ORNL, LANL, and BNL. 2014.

30.   Radchenko, V., et al., Application of ion exchange and extraction chromatography to the separation of actinium from proton-irradiated thorium metal for analytical purposes. Journal of Chromatography A, 2015. **1380**: p. 55-63.

31.   Canberra, Genie 2000 Spectroscopy Software: Customization Tools. 2009.

32.   Browne, E. and J.K. Tuli, Nuclear Data Sheets for A = 99. Nuclear Data Sheets, 2011. **112**(2): p. 275-446.

33.   Burrows, T.W., Nuclear Data Sheets for A = 139. Nuclear Data Sheets, 2001. **92**(3): p. 623-782.

34.   Nica, N., Nuclear Data Sheets for A = 140. Nuclear Data Sheets, 2007. **108**(7): p. 1287-1470.

35.   Nica, N., Nuclear Data Sheets for A = 141. Nuclear Data Sheets, 2014. **122**: p. 1-204.

36.   Browne, E. and J.K. Tuli, Nuclear Data Sheets for A = 143. Nuclear Data Sheets, 2012. **113**(3): p. 715-908.

37.   Sonzogni, A.A., Nuclear Data Sheets for A = 144. Nuclear Data Sheets, 2001. **93**(3): p. 599-762.

38.   Browne, E., Nuclear Data Sheets for A = 212. Nuclear Data Sheets, 2005. **104**(2): p. 427-496.

39.   Basunia, M.S., Nuclear Data Sheets for A = 213. Nuclear Data Sheets, 2007. **108**(3): p. 633-680.

40.   Kumar Jain, A., et al., Nuclear Data Sheets for A = 221. Nuclear Data Sheets, 2007. **108**(4): p. 883-922.

41.   Singh, S., A.K. Jain, and J.K. Tuli, Nuclear Data Sheets for A = 222. Nuclear Data Sheets, 2011. **112**(11): p. 2851-2886.

42.   Browne, E., Nuclear Data Sheets for A = 215,219,223,227,231. Nuclear Data Sheets, 2001. **93**(4): p. 763-1061.

43.   Artna-Cohen, A., Nuclear Data Sheets for A = 224. Nuclear Data Sheets, 1997. **80**(1): p. 227-262.

44.   Armstrong, T.W. and K.C. Chandler, SPAR, A FORTRAN Program for Computing Stopping Powers and Ranges for Muons, Charged Pions, Protons, and Heavy Ions, O.R.N. Laboratory, Editor. 1973.

45.   Sato, T., et al., Particle and Heavy Ion Transport code System, PHITS, version 2.52. Journal of Nuclear Science and Technology, 2013. **50**(9): p. 913-923.

46.   Boudard, A., et al., New potentialities of the Liege intranuclear cascade model for reactions induced by nucleons and light charged particles. Physical Review C, 2013. **87**(1): p. 014606.

47.   McDevitt, M.R., et al., An [225]Ac/[213]Bi generator system for therapeutic clinical applications: construction and operation. Applied Radiation Isotopes, 1999. **50**(5): p. 895-904.

48.   Thorek, D., Report [213]Bi – Generator delivered from Oak Ridge. 2014: Johns Hopkins University.

49.   Ermolaev, S.V., et al., Production of actinium, thorium and radium isotopes from natural thorium irradiated with protons up to 141 MeV. Radiochimica Acta, 2012. **100**(4): p. 223.

50.   Titarenko, Y.E., V. Batyaev, and E. Karpikhin, Experimental and theoretical study of the yields of residual product nuclei produced in thin targets irradiated by 100-2600 MeV protons. 2003, International Nuclear Data Committee.

51.   Gauvin, H., Reactions (p, 2pxn) sur le thorium 232 de 30 à 120 MeV. J. Phys. France, 1963. **24**(11): p. 836-838.

52. Lefort, M., G.N. Simonoff, and X. Tarrago, Spallation Reactions of Thorium by 150 and 82 MeV Protons. Nuclear Physics, 1961. **25**: p. 216-247.

53. Engle, J.W., et al., Ac, La, and Ce radioimpurities in [225]Ac produced in 40–200 MeV proton irradiations of thorium. Radiochimica Acta, 2014. **102**(7): p. 569-581.

54. Hogan, J.J., et al., Fissionability of nuclides in the thorium region at excitation energies to 100 MeV. Physical Review C, 1979. **20**(5): p. 1831-1843.

55. Duijvestijn, M.C., et al., Proton-induced fission at 190 MeV of [nat]W, [197]Au, [nat]Pb, [208]Pb, and [232]Th. Physical Review C, 1999. **59**(2): p. 776-788.

56. Holub, R. and L. Yaffe, Charge dispersion studies of heavy-mass elements in the fission of [232]Th by protons of medium energy. Journal of Inorganic and Nuclear Chemistry, 1973. **35**(12): p. 3991-4000.

57. Zhuikov, B.L., et al., Production of [225]Ac and [223]Ra by irradiation of Th with accelerated protons. Radiochemistry, 2011. **53**(1): p. 73-80.

Appendices

Appendix A: Typical PHITS Input File

[T i t l e]
    Proton irradiation of Thorium-232 foil

[Parameters]
icntl = 0   ! Main control parameter.

    rseed = 81884
    maxcas = 1000000   ! Number of calculation in each batch
    maxbch = 100   ! Number of batch

    emin(1) = 0.1   ! Energy cutoff for proton   (MeV)   (D=1.0)
    emin(2) = 0.001   !   neutron (MeV)   (D=1.0)
    emin(12) = 1.0   !   electron (MeV) (D=1.d9)
    emin(13) = 1.0   !   positron (MeV) (D=1.d9)
    emin(14) = 2.0   !   photon   (MeV) (D=1.d9)
    emin(15) = 1.0   !   deuteron (MeV/u) (D=1.d9)
    emin(16) = 1.0   !   triton   (MeV/u) (D=1.d9)
    emin(17) = 1.0   !   3He   (MeV/u) (D=1.d9)
    emin(18) = 1.0   !   Alpha   (MeV/u) (D=1.d9)
    emin(19) = 0.00001   !   Heavy Ion (MeV/u) (D=1.d9)

dmax(2) = 20.   ! Maximum E (MeV) of cross section use for n (D=emin(2))

    itall = 1.   ! Output results after each batch
    file(7) = c:/phits/data/xsdir.jnd   ! Cross section data file name
    file(14) = c:/phits/data/trxcrd.dat
    file(6) = protons192MeV_Z91_162A168.out   ! General output file name

    icrhi = 1   ! Total reac. XS for HI; 0: Shen, 1: Tripathi

    inmed = 2   ! nucleon-nucleon XS 0: free, 1: Cugnon old, 2: Cugnon new

    nevap = 3   ! Evap model 0: no, 1: DRES, 2: SDM, 3: GEM

    nspred = 1   ! Coulomb diffusion on
    ndedx = 0   ! dE/dx by 0:SPAR+NMTC, 1: ATIMA+NMTC, 2: SPAR+NMTC (D=2)
                                                        !
                      ! Using ATIMA is better than SPAR for lower energy
                      ! but it takes longer time (2 - 10 times)
                                                        !
    nedisp = 1   ! E stragg 0: no, 1: Landau, 2: ATIMA

    igamma = 3   ! 0: no gamma emitt 1: with gamma emit

    e-mode = 1   ! 0: standard, 1: event generator mode

imagnf = 1   ! Magnetic field
itstep = 0   ! Tally tracks of charged particles under magnetic field
                   ! (it is only for 2D graphical plots)

[Source]
    s-type = 1   ! Source type. 1: cylinder source
     proj = proton   ! Projectile

```
   e0 = 192      ! Energy (MeV/u)
   r0 = 0.1      ! Radius of the cylinder (cm)
   x0 = 0.0
   y0 = 0.0
   z0 = -0.1     ! Position z of one cylinder surface (cm)
   z1 = -0.1     ! Position z of another cylinder surface (cm)
   dir = 1.0     ! Direction of the beam (cos(theta_z))


[ Material ]
   mat[1] $232-Th  density = 11.724 g/cm3
        90232.50c 3.0427E-02


[ Surface ]
1 RCC 0.0 0.0 0.0 0.0 0.0 0.0125 1.45  $target dimensions
9  SPH 0.0 0.0 0.0 100.0        $ DEFINES LIMIT OF THE UNIVERSE


[ Cell ]
1 1 -11.724 -1          $ Th target
2 0 1 -9       $ rest of universe
999 -1  9      $ Outer void



$Thorium Isotopes z = 90

[ T-product ]
 part = 229Th 230Th 231Th 233Th
  mesh = reg
  reg = 1
mother = all
e-type = 3
   ne = 1
  emin = 0.0001
  emax = 100
  unit = 1
  axis = eng
  file = nuclear_Th_productsa_192MeV.out
output = nuclear
dump = -2
1 4
 x-txt = {\it En}  (MeV)
 y-txt = {\it # per source ion}
epsout = 1

[ T-product ]
 part = 227Th 228Th 226Th 225Th
  mesh = reg
  reg = 1
mother = all
e-type = 3
   ne = 1
  emin = 0.0001
  emax = 100
  unit = 1
  axis = eng
  file = nuclear_Th_productsb_192MeV.out
output = nuclear
```

```
dump = -2
1 4
 x-txt = {\it En}  (MeV)
 y-txt = {\it # per source ion}
epsout = 1

$Protactinium Isotopes z = 91

[ T-product ]
 part = 233Pa 232Pa 231Pa 230Pa 229Pa 228Pa
  mesh = reg
  reg = 1
mother = all
e-type = 3
   ne = 1
  emin = 0.0001
  emax = 10
  unit = 1
  axis = eng
  file = nuclear_Pa_products_192MeV.out
output = nuclear
dump = -2
1 4
 x-txt = {\it En}  (MeV)
 y-txt = {\it # per source ion}
epsout = 1

$Actinium Isotopes z = 89

[ T-product ]
 part = 229Ac 228Ac 227Ac 226Ac 225Ac 224Ac
  mesh = reg
  reg = 1
mother = all
e-type = 3
   ne = 1
  emin = 0.00001
  emax = 200
  unit = 1
  axis = eng
  file = nuclear_Ac_products_192MeV.out
output = nuclear
dump = -2
1 4
 x-txt = {\it En}  (MeV)
 y-txt = {\it # per source ion}
epsout = 1

$Radium Isotopes z = 88

[ T-product ]
 part = 227Ra 226Ra 225Ra 224Ra 223Ra 222Ra
  mesh = reg
  reg = 1
mother = all
e-type = 3
```

```
   ne = 1
  emin = 0.00001
  emax = 200
  unit = 1
  axis = eng
  file = nuclear_Ra_products_192MeV.out
output = nuclear
dump = -2
1 4
 x-txt = {\it En}  (MeV)
 y-txt = {\it # per source ion}
epsout = 1


$Isotopes A=162

[ T-product ]
 part = Eu162 Gd162 Tb162 Ho162 Tm162 Yb162
  mesh = reg
  reg = 1
mother = all
e-type = 3
   ne = 1
  emin = 0.00001
  emax = 200
  unit = 1
  axis = eng
  file = fission_162_products_192MeV.out
output = fission
dump = -2
1 4
 x-txt = {\it En}  (MeV)
 y-txt = {\it # per source ion}
epsout = 1


$Isotopes A=163

[ T-product ]
 part = Gd163 Tb163 Ho163 Er163 Tm163 Yb163
  mesh = reg
  reg = 1
mother = all
e-type = 3
   ne = 1
  emin = 0.00001
  emax = 200
  unit = 1
  axis = eng
  file = fission_163_products_192MeV.out
output = fission
dump = -2
1 4
 x-txt = {\it En}  (MeV)
 y-txt = {\it # per source ion}
epsout = 1


$Isotopes A=164
```

```
[ T-product ]
 part = Gd164 Tb164 Ho164 Tm164 Yb164 Lu164
  mesh = reg
  reg = 1
mother = all
e-type = 3
   ne = 1
  emin = 0.00001
  emax = 200
  unit = 1
  axis = eng
  file = fission_164_products_192MeV.out
output = fission
dump = -2
1 4
 x-txt = {\it En}  (MeV)
 y-txt = {\it # per source ion}
epsout = 1

$Isotopes A=165

[ T-product ]
 part = Gd165 Tb165 Dy165 Er165 Tm165 Yb165
  mesh = reg
  reg = 1
mother = all
e-type = 3
   ne = 1
  emin = 0.00001
  emax = 200
  unit = 1
  axis = eng
  file = fission_165_products_192MeV.out
output = fission
dump = -2
1 4
 x-txt = {\it En}  (MeV)
 y-txt = {\it # per source ion}
epsout = 1

$Isotopes A=166

[ T-product ]
 part = Tb166 Dy166 Ho166 Tm166 Yb166 Lu166
  mesh = reg
  reg = 1
mother = all
e-type = 3
   ne = 1
  emin = 0.00001
  emax = 200
  unit = 1
  axis = eng
  file = fission_166_products_192MeV.out
output = fission
```

```
dump = -2
1 4
 x-txt = {\it En}  (MeV)
 y-txt = {\it # per source ion}
epsout = 1

$Isotopes A=167

[ T-product ]
 part = Tb167 Dy167 Ho167 Tm167 Yb167 Lu167
  mesh = reg
  reg = 1
mother = all
e-type = 3
   ne = 1
  emin = 0.00001
  emax = 200
  unit = 1
  axis = eng
  file = fission_167_products_192MeV.out
output = fission
dump = -2
1 4
 x-txt = {\it En}  (MeV)
 y-txt = {\it # per source ion}
epsout = 1

$Isotopes A=168

[ T-product ]
 part = Tb168 Dy168 Ho168 Tm168 Lu168 Hf168
  mesh = reg
  reg = 1
mother = all
e-type = 3
   ne = 1
  emin = 0.00001
  emax = 200
  unit = 1
  axis = eng
  file = fission_168_products_192MeV.out
output = fission
dump = -2
1 4
 x-txt = {\it En}  (MeV)
 y-txt = {\it # per source ion}
epsout = 1
```

Appendix B: Table of All PHITS Calculated Cross Sections

*Note: Concise notation is used for brevity. Example: 76.5 (8) is equivalent to 76.5 ± 0.8.

Table B.1. PHITS simulated independent cross sections (in mb) for isotopes of Ra, Ac, Th, Pa, and A = 82 to A = 168 at 77-192 MeV.

Isotope	76.5 (8) MeV	89.9 (4) MeV	127.8 (5) MeV	152.5 (5) MeV	173.6 (5) MeV	192.1 (5) MeV
Ge-82	2.00 (7)	1.90 (5)	1.33 (8)	1.51 (9)	1.25 (8)	1.33 (8)
As-82	5.8 (1)	5.68 (8)	4.3 (2)	4.2 (1)	4.0 (1)	4.3 (2)
Se-82	9.3 (1)	9.4 (1)	8.3 (2)	8.0 (2)	8.1 (2)	8.3 (2)
Br-82	1.75 (7)	2.08 (5)	2.4 (1)	2.7 (1)	3.0 (1)	2.4 (1)
Rb-82	-	-	0.005 (5)	-	0.03 (1)	0.005 (5)
Se-83	8.2 (1)	8.2 (1)	7.2 (2)	6.6 (2)	6.3 (2)	7.2 (2)
Br-83	5.6 (1)	6.10 (9)	6.1 (2)	6.4 (2)	6.2 (2)	6.1 (2)
Rb-83	0.015 (6)	0.012 (4)	0.05 (2)	0.005 (5)	0.04 (1)	0.05 (2)
As-84	2.50 (8)	2.31 (5)	1.66 (9)	1.47 (9)	1.36 (8)	1.66 (9)
Se-84	13.6 (2)	12.7 (1)	10.4 (2)	9.7 (2)	8.7 (2)	10.4 (2)
Br-84	8.4 (1)	8.4 (1)	7.6 (2)	7.4 (2)	7.8 (2)	7.6 (2)
Rb-84	0.05 (1)	0.08 (1)	0.17 (3)	0.24 (4)	0.33 (4)	0.17 (3)
Se-85	6.5 (1)	6.14 (9)	4.7 (2)	4.3 (1)	4.0 (1)	4.7 (2)
Br-85	16.7 (2)	16.0 (1)	13.4 (3)	12.8 (3)	12.0 (3)	13.4 (3)
Kr-85	4.7 (1)	4.80 (8)	4.7 (2)	5.0 (2)	5.4 (2)	4.7 (2)
Sr-85	0.005 (3)	0.005 (2)	0.016 (9)	0.03 (1)	0.05 (2)	0.016 (9)
Se-86	5.8 (1)	5.09 (8)	3.6 (1)	3.6 (1)	3.2 (1)	3.6 (1)
Br-86	11.6 (2)	10.9 (1)	8.7 (2)	7.7 (2)	7.6 (2)	8.7 (2)
Rb-86	1.59 (6)	1.78 (5)	2.1 (1)	2.4 (1)	2.8 (1)	2.1 (1)
Br-87	12.1 (2)	11.1 (1)	8.5 (2)	8.1 (2)	7.4 (2)	8.5 (2)
Kr-87	12.9 (2)	12.8 (1)	10.4 (2)	9.8 (2)	9.7 (2)	10.4 (2)
Rb-87	6.4 (1)	6.75 (9)	6.7 (2)	7.2 (2)	7.7 (2)	6.7 (2)
Y-87	-	-	0.005 (5)	0.005 (5)	0.04 (1)	0.005 (5)
Br-88	7.3 (1)	6.53 (9)	5.1 (2)	4.2 (1)	3.9 (1)	5.1 (2)
Kr-88	18.2 (2)	16.9 (1)	13.8 (3)	12.6 (3)	11.5 (2)	13.8 (3)
Rb-88	9.2 (1)	8.9 (1)	8.4 (2)	8.5 (2)	8.5 (2)	8.4 (2)
Y-88	0.010 (5)	0.030 (6)	0.06 (2)	0.10 (2)	0.16 (3)	0.06 (2)
Zr-88	-	-	-	0.011 (7)	-	-
As-89	0.024 (8)	0.016 (4)	-	0.005 (5)	0.005 (5)	-
Se-89	0.39 (3)	0.33 (2)	0.16 (3)	0.19 (3)	0.21 (3)	0.16 (3)
Br-89	4.7 (1)	4.43 (7)	3.3 (1)	3.1 (1)	2.8 (1)	3.3 (1)
Kr-89	12.6 (2)	11.5 (1)	9.1 (2)	8.1 (2)	7.2 (2)	9.1 (2)
Rb-89	15.5 (2)	15.5 (1)	13.1 (3)	12.8 (3)	12.5 (3)	13.1 (3)
Sr-89	3.9 (1)	4.21 (7)	4.9 (2)	4.9 (2)	5.1 (2)	4.9 (2)
Se-90	0.15 (2)	0.14 (1)	0.11 (2)	0.12 (3)	0.08 (2)	0.11 (2)
Br-90	1.71 (6)	1.60 (4)	1.15 (8)	1.06 (7)	1.00 (7)	1.15 (8)
Kr-90	10.9 (2)	9.7 (1)	7.5 (2)	6.4 (2)	6.3 (2)	7.5 (2)
Rb-90	16.4 (2)	15.6 (1)	12.6 (3)	11.7 (2)	11.0 (2)	12.6 (3)

Table B.1 Continued.

Isotope	76.5 (8) MeV	89.9 (4) MeV	127.8 (5) MeV	152.5 (5) MeV	173.6 (5) MeV	192.1 (5) MeV
Sr-90	9.9 (2)	10.1 (1)	9.5 (2)	9.7 (2)	10.1 (2)	9.5 (2)
Y-90	0.92 (5)	1.03 (4)	1.43 (9)	1.67 (9)	2.1 (1)	1.43 (9)
Se-91	0.034 (9)	0.022 (5)	0.016 (9)	0.011 (7)	0.016 (9)	0.016 (9)
Br-91	0.91 (5)	0.76 (3)	0.58 (6)	0.58 (6)	0.54 (5)	0.58 (6)
Kr-91	4.6 (1)	4.42 (7)	3.3 (1)	3.0 (1)	2.7 (1)	3.3 (1)
Rb-91	17.2 (2)	15.8 (1)	12.6 (3)	11.4 (2)	10.9 (2)	12.6 (3)
Sr-91	12.7 (2)	12.2 (1)	11.2 (2)	10.5 (2)	10.2 (2)	11.2 (2)
Y-91	3.19 (9)	3.37 (6)	4.1 (1)	4.3 (1)	4.9 (2)	4.1 (1)
Se-92	0.012 (5)	0.012 (4)	0.011 (7)	0.005 (5)	0.011 (7)	0.011 (7)
Br-92	0.22 (2)	0.21 (2)	0.14 (3)	0.18 (3)	0.17 (3)	0.14 (3)
Kr-92	2.98 (8)	2.73 (6)	2.0 (1)	1.9 (1)	1.50 (9)	2.0 (1)
Rb-92	11.0 (2)	10.2 (1)	7.8 (2)	7.0 (2)	6.2 (2)	7.8 (2)
Sr-92	18.8 (2)	17.7 (1)	15.0 (3)	13.7 (3)	13.7 (3)	15.0 (3)
Y-92	6.5 (1)	6.45 (9)	6.5 (2)	7.0 (2)	7.1 (2)	6.5 (2)
Br-93	0.12 (2)	0.12 (1)	0.06 (2)	0.09 (2)	0.09 (2)	0.06 (2)
Kr-93	0.97 (5)	0.85 (3)	0.62 (6)	0.60 (6)	0.46 (5)	0.62 (6)
Rb-93	7.9 (1)	7.35 (9)	5.7 (2)	5.0 (2)	4.9 (2)	5.7 (2)
Sr-93	15.0 (2)	13.6 (1)	11.4 (2)	10.6 (2)	10.1 (2)	11.4 (2)
Y-93	12.1 (2)	12.0 (1)	11.7 (2)	11.4 (2)	11.4 (2)	11.7 (2)
Zr-93	1.92 (7)	2.14 (5)	2.8 (1)	3.4 (1)	3.7 (1)	2.8 (1)
Br-94	0.019 (7)	0.022 (5)	0.03 (1)	0.016 (9)	0.005 (5)	0.03 (1)
Kr-94	0.55 (4)	0.52 (3)	0.42 (5)	0.39 (5)	0.35 (4)	0.42 (5)
Rb-94	3.17 (9)	3.08 (6)	2.4 (1)	2.3 (1)	2.0 (1)	2.4 (1)
Sr-94	14.7 (2)	13.5 (1)	10.8 (2)	10.1 (2)	9.3 (2)	10.8 (2)
Y-94	14.6 (2)	14.1 (1)	12.5 (3)	12.6 (3)	11.6 (2)	12.5 (3)
Nb-94	0.28 (3)	0.37 (2)	0.60 (6)	0.91 (7)	0.86 (7)	0.60 (6)
Kr-95	0.14 (2)	0.15 (1)	0.08 (2)	0.07 (2)	0.05 (2)	0.08 (2)
Rb-95	2.14 (7)	1.99 (5)	1.36 (8)	1.45 (9)	1.35 (8)	1.36 (8)
Sr-95	7.2 (1)	6.58 (9)	5.4 (2)	4.8 (2)	4.7 (2)	5.4 (2)
Y-95	17.4 (2)	16.4 (1)	14.2 (3)	13.5 (3)	12.7 (3)	14.2 (3)
Zr-95	8.7 (1)	9.0 (1)	9.2 (2)	9.4 (2)	9.9 (2)	9.2 (2)
Nb-95	1.37 (6)	1.60 (4)	2.2 (1)	2.5 (1)	2.7 (1)	2.2 (1)
Br-96	0.005 (3)	0.002 (2)	-	-	0.005 (5)	-
Kr-96	0.10 (2)	0.09 (1)	0.03 (1)	0.07 (2)	0.02 (1)	0.03 (1)
Rb-96	0.80 (4)	0.69 (3)	0.57 (6)	0.55 (5)	0.46 (5)	0.57 (6)
Sr-96	5.8 (1)	5.24 (8)	4.4 (2)	4.0 (1)	4.0 (1)	4.4 (2)
Y-96	12.2 (2)	11.4 (1)	10.5 (2)	9.3 (2)	8.9 (2)	10.5 (2)
Nb-96	3.01 (9)	3.40 (6)	4.2 (1)	4.8 (2)	4.9 (2)	4.2 (1)
Kr-97	0.027 (8)	0.022 (5)	0.011 (7)	0.011 (7)	0.02 (1)	0.011 (7)
Rb-97	0.50 (3)	0.47 (2)	0.39 (5)	0.25 (4)	0.26 (4)	0.39 (5)
Sr-97	2.39 (8)	2.29 (5)	1.69 (9)	1.57 (9)	1.50 (9)	1.69 (9)
Y-97	10.8 (2)	10.2 (1)	8.4 (2)	7.9 (2)	7.5 (2)	8.4 (2)
Zr-97	13.3 (2)	12.8 (1)	12.3 (3)	11.4 (2)	11.3 (2)	12.3 (3)
Nb-97	7.3 (1)	7.6 (1)	8.5 (2)	9.1 (2)	9.5 (2)	8.5 (2)
Kr-98	0.012 (5)	0.006 (3)	0.005 (5)	0.005 (5)	0.005 (5)	0.005 (5)
Rb-98	0.18 (2)	0.17 (1)	0.10 (2)	0.09 (2)	0.11 (2)	0.10 (2)

Table B.1 Continued.

Isotope	76.5 (8) MeV	89.9 (4) MeV	127.8 (5) MeV	152.5 (5) MeV	173.6 (5) MeV	192.1 (5) MeV
Sr-98	1.69 (6)	1.62 (4)	1.16 (8)	1.11 (8)	1.19 (8)	1.16 (8)
Y-98	5.7 (1)	5.63 (8)	4.7 (2)	4.2 (1)	4.0 (1)	4.7 (2)
Zr-98	14.4 (2)	13.6 (1)	12.6 (3)	12.2 (3)	12.3 (3)	12.6 (3)
Nb-98	9.3 (2)	9.4 (1)	9.9 (2)	10.3 (2)	9.7 (2)	9.9 (2)
Rb-99	0.08 (1)	0.059 (8)	0.08 (2)	0.07 (2)	0.04 (1)	0.08 (2)
Sr-99	0.52 (4)	0.49 (2)	0.39 (5)	0.31 (4)	0.36 (4)	0.39 (5)
Y-99	5.1 (1)	4.71 (8)	4.0 (1)	3.4 (1)	3.4 (1)	4.0 (1)
Zr-99	9.9 (2)	9.4 (1)	8.0 (2)	7.8 (2)	7.4 (2)	8.0 (2)
Nb-99	13.4 (2)	13.6 (1)	13.8 (3)	13.2 (3)	13.4 (3)	13.8 (3)
Mo-99	3.8 (1)	4.19 (7)	5.2 (2)	5.7 (2)	6.4 (2)	5.2 (2)
Rb-100	0.027 (8)	0.018 (5)	0.03 (1)	0.011 (7)	0.005 (5)	0.03 (1)
Sr-100	0.34 (3)	0.34 (2)	0.31 (4)	0.28 (4)	0.24 (4)	0.31 (4)
Y-100	2.39 (8)	2.37 (5)	2.1 (1)	1.8 (1)	1.59 (9)	2.1 (1)
Zr-100	10.4 (2)	10.3 (1)	8.7 (2)	8.2 (2)	7.7 (2)	8.7 (2)
Nb-100	12.9 (2)	12.8 (1)	12.2 (3)	11.3 (2)	11.9 (2)	12.2 (3)
Tc-100	0.94 (5)	1.13 (4)	1.8 (1)	2.3 (1)	2.5 (1)	1.8 (1)
Rb-101	0.005 (3)	0.008 (3)	0.005 (5)	0.016 (9)	0.016 (9)	0.005 (5)
Sr-101	0.09 (1)	0.08 (1)	0.06 (2)	0.04 (1)	0.05 (2)	0.06 (2)
Y-101	1.40 (6)	1.32 (4)	1.05 (7)	0.90 (7)	0.93 (7)	1.05 (7)
Zr-101	5.4 (1)	5.35 (8)	4.4 (2)	4.1 (1)	3.7 (1)	4.4 (2)
Nb-101	15.3 (2)	14.7 (1)	14.0 (3)	13.9 (3)	13.1 (3)	14.0 (3)
Tc-101	3.28 (9)	3.66 (7)	5.0 (2)	5.8 (2)	6.4 (2)	5.0 (2)
Sr-102	0.060 (9)	0.07 (1)	0.05 (2)	0.04 (1)	0.02 (1)	0.02 (1)
Y-102	0.56 (3)	0.58 (4)	0.35 (4)	0.34 (3)	0.44 (5)	0.38 (4)
Zr-102	4.22 (7)	4 (1)	3.5 (1)	2.83 (9)	2.6 (1)	2.4 (1)
Nb-102	10.6 (1)	10.4 (2)	9.7 (2)	8.8 (2)	8.5 (2)	8.1 (2)
Mo-102	17.3 (1)	17.5 (2)	17.3 (3)	17.6 (2)	17.5 (3)	17.5 (3)
Tc-102	5.18 (8)	5.6 (1)	6.9 (2)	7.6 (1)	8.2 (2)	8.6 (2)
Y-103	0.27 (2)	0.24 (2)	0.18 (3)	0.17 (2)	0.16 (3)	0.11 (2)
Zr-103	1.80 (5)	1.69 (6)	1.31 (8)	1.12 (5)	1.00 (7)	1.08 (8)
Nb-103	9.9 (1)	9.8 (2)	8.5 (2)	7.8 (1)	7.7 (2)	7.4 (2)
Mo-103	13.4 (1)	12.9 (2)	12.2 (3)	12.5 (2)	12.0 (3)	11.7 (2)
Tc-103	11.0 (1)	11.6 (2)	12.9 (3)	13.6 (2)	14.3 (3)	14.8 (3)
Ru-103	1.55 (4)	1.81 (7)	2.9 (1)	3.6 (1)	4.1 (1)	4.7 (2)
Y-104	0.048 (8)	0.06 (1)	0.05 (2)	0.024 (8)	0.02 (1)	0.04 (1)
Zr-104	1.12 (4)	1.03 (5)	0.83 (7)	0.69 (4)	0.63 (6)	0.57 (6)
Nb-104	5.06 (8)	4.7 (1)	4.1 (1)	3.8 (1)	3.4 (1)	3.6 (1)
Mo-104	16.6 (1)	16.2 (2)	14.9 (3)	13.7 (2)	13.3 (3)	13.3 (3)
Tc-104	12.1 (1)	12.1 (2)	12.8 (3)	13.4 (2)	13.5 (3)	13.8 (3)
Rh-104	0.20 (2)	0.31 (3)	0.71 (6)	0.97 (5)	1.33 (8)	1.48 (9)
Zr-105	0.28 (2)	0.32 (3)	0.21 (3)	0.19 (2)	0.17 (3)	0.17 (3)
Nb-105	3.73 (7)	3.70 (9)	3.0 (1)	2.71 (8)	2.4 (1)	2.3 (1)
Mo-105	9.5 (1)	9.2 (1)	8.2 (2)	7.5 (1)	7.0 (2)	7.3 (2)
Tc-105	18.6 (1)	18.6 (2)	18.4 (3)	18.0 (2)	17.9 (3)	17.7 (3)
Ru-105	6.90 (9)	7.9 (1)	9.3 (2)	9.9 (2)	10.2 (2)	10.6 (2)
Rh-105	1.19 (4)	1.49 (6)	2.6 (1)	3.22 (9)	3.7 (1)	4.3 (1)

Table B.1 Continued.

Isotope	76.5 (8) MeV	89.9 (4) MeV	127.8 (5) MeV	152.5 (5) MeV	173.6 (5) MeV	192.1 (5) MeV
Zr-106	0.18 (1)	0.19 (2)	0.09 (2)	0.08 (1)	0.06 (2)	0.07 (2)
Nb-106	1.28 (4)	1.25 (6)	0.95 (7)	0.91 (5)	0.82 (7)	0.86 (7)
Mo-106	9.1 (1)	8.7 (1)	7.1 (2)	6.6 (1)	6.2 (2)	6.1 (2)
Tc-106	14.0 (1)	14.1 (2)	13.3 (3)	12.7 (2)	12.2 (3)	11.9 (3)
Ru-106	15.3 (1)	15.9 (2)	17.2 (3)	17.3 (2)	18.0 (3)	18.5 (3)
Rh-106	2.49 (5)	2.92 (8)	4.3 (2)	5.0 (1)	5.5 (2)	5.9 (2)
Nb-107	0.90 (3)	0.84 (4)	0.58 (6)	0.55 (4)	0.51 (5)	0.46 (5)
Mo-107	4.01 (7)	4 (1)	3.2 (1)	2.95 (9)	2.6 (1)	2.4 (1)
Tc-107	16.2 (1)	15.5 (2)	14.6 (3)	13.2 (2)	12.7 (3)	12.6 (3)
Ru-107	14.0 (1)	14.1 (2)	14.4 (3)	14.3 (2)	14.0 (3)	14.0 (3)
Rh-107	7.14 (9)	7.9 (1)	10.5 (2)	10.7 (2)	11.5 (2)	12.0 (3)
Pd-107	0.47 (2)	0.61 (4)	1.42 (9)	1.71 (7)	2.0 (1)	2.3 (1)
Nb-108	0.28 (2)	0.24 (2)	0.16 (3)	0.17 (2)	0.14 (3)	0.12 (3)
Mo-108	2.89 (6)	2.72 (8)	2.2 (1)	1.86 (7)	1.8 (1)	1.65 (9)
Tc-108	8.9 (1)	8.4 (1)	7.4 (2)	6.8 (1)	6.7 (2)	6.3 (2)
Ru-108	20.3 (2)	19.9 (2)	19.2 (3)	18.2 (2)	17.3 (3)	17.8 (3)
Rh-108	9.5 (1)	9.8 (2)	11.2 (2)	12.0 (2)	12.2 (3)	12.8 (3)
Ag-108	0.037 (7)	0.06 (1)	0.21 (3)	0.25 (3)	0.41 (5)	0.48 (5)
Mo-109	1.02 (4)	0.93 (5)	0.76 (6)	0.69 (4)	0.61 (6)	0.54 (5)
Tc-109	8 (1)	7.8 (1)	6.7 (2)	6.2 (1)	5.7 (2)	5.2 (2)
Ru-109	13.4 (1)	13.2 (2)	12.2 (3)	11.3 (2)	11.2 (2)	10.3 (2)
Rh-109	17.1 (1)	17.6 (2)	18.6 (3)	18.1 (2)	18.4 (3)	18.7 (3)
Pd-109	3.87 (7)	4.5 (1)	6.3 (2)	6.4 (1)	7.2 (2)	7.8 (2)
Cd-109	-	0.005 (3)	0.02 (1)	0.011 (5)	0.09 (2)	0.08 (2)
Nb-110	0.035 (7)	0.027 (8)	0.04 (1)	0.032 (9)	0.011 (7)	0.005 (5)
Mo-110	0.69 (3)	0.66 (4)	0.40 (5)	0.37 (3)	0.33 (4)	0.42 (5)
Tc-110	3.48 (6)	3.14 (9)	2.4 (1)	2.15 (8)	2.2 (1)	2.0 (1)
Ru-110	14.8 (1)	14.1 (2)	11.9 (3)	11.4 (2)	10.7 (2)	10.1 (2)
Rh-110	16.0 (1)	15.9 (2)	15.7 (3)	15.3 (2)	14.9 (3)	15.0 (3)
Ag-110	0.81 (3)	1.05 (5)	1.8 (1)	2.13 (7)	2.4 (1)	3.1 (1)
Tc-111	2.62 (6)	2.48 (8)	1.8 (1)	1.63 (7)	1.56 (9)	1.53 (9)
Ru-111	7.5 (1)	7.0 (1)	6.1 (2)	5.4 (1)	4.7 (2)	5.1 (2)
Rh-111	19.3 (2)	18.9 (2)	18.1 (3)	16.8 (2)	16.5 (3)	16.0 (3)
Pd-111	11.2 (1)	11.6 (2)	12.6 (3)	12.3 (2)	12.7 (3)	13.1 (3)
Ag-111	3.21 (6)	3.73 (9)	5.1 (2)	6.0 (1)	6.5 (2)	6.7 (2)
In-111	-	-	0.011 (7)	0.013 (6)	0.03 (1)	0.02 (1)
Mo-112	0.12 (1)	0.10 (2)	0.07 (2)	0.07 (1)	0.03 (1)	0.08 (2)
Tc-112	0.82 (3)	0.87 (5)	0.61 (6)	0.57 (4)	0.40 (5)	0.40 (5)
Ru-112	6.87 (9)	6.6 (1)	5.0 (2)	4.6 (1)	4.2 (1)	4.0 (1)
Rh-112	13.1 (1)	12.6 (2)	11.4 (2)	10.1 (2)	9.7 (2)	9.6 (2)
Pd-112	19.7 (2)	20.2 (2)	20.0 (3)	19.3 (2)	19.6 (3)	19.2 (3)
Ag-112	5.21 (8)	5.8 (1)	7.2 (2)	7.9 (1)	7.6 (2)	8.5 (2)
Mo-113	0.017 (5)	0.002 (2)	0.005 (5)	0.013 (6)	-	-
Tc-113	0.52 (3)	0.52 (4)	0.36 (4)	0.31 (3)	0.32 (4)	0.30 (4)
Ru-113	2.54 (6)	2.26 (7)	1.9 (1)	1.58 (6)	1.54 (9)	1.37 (8)
Rh-113	13.1 (1)	12.8 (2)	10.8 (2)	9.7 (2)	9.8 (2)	8.9 (2)

Table B.1 Continued.

Isotope	76.5 (8) MeV	89.9 (4) MeV	127.8 (5) MeV	152.5 (5) MeV	173.6 (5) MeV	192.1 (5) MeV
Pd-113	14.7 (1)	14.8 (2)	13.4 (3)	13.0 (2)	12.8 (3)	12.2 (3)
Ag-113	11.7 (1)	12.3 (2)	13.8 (3)	14.1 (2)	14.7 (3)	14.5 (3)
Tc-114	0.13 (1)	0.15 (2)	0.08 (2)	0.08 (1)	0.08 (2)	0.09 (2)
Ru-114	1.84 (5)	1.74 (6)	1.19 (8)	1.03 (5)	1.10 (8)	1.03 (7)
Rh-114	6.32 (9)	6.1 (1)	5.0 (2)	4.4 (1)	4.1 (1)	4.1 (1)
Pd-114	19.4 (2)	18.3 (2)	16.8 (3)	15.4 (2)	14.9 (3)	14.2 (3)
Ag-114	12.3 (1)	12.1 (2)	12.5 (3)	12.9 (2)	12.8 (3)	12.9 (3)
In-114	0.15 (1)	0.25 (2)	0.61 (6)	0.79 (5)	1.00 (7)	1.03 (7)
Tc-115	0.051 (8)	0.07 (1)	0.05 (2)	0.034 (9)	0.04 (1)	0.04 (1)
Ru-115	0.55 (3)	0.56 (4)	0.34 (4)	0.34 (3)	0.27 (4)	0.27 (4)
Rh-115	5.26 (8)	4.8 (1)	3.7 (1)	3.6 (1)	3.3 (1)	3.1 (1)
Pd-115	10.6 (1)	10.5 (2)	8.9 (2)	7.9 (1)	7.6 (2)	7.2 (2)
Ag-115	18.9 (2)	18.9 (2)	18.5 (3)	17.7 (2)	17.6 (3)	16.9 (3)
Cd-115	6.67 (9)	6.9 (1)	8.4 (2)	8.9 (2)	9.3 (2)	9.6 (2)
Tc-116	0.011 (4)	0.015 (6)	0.005 (5)	0.005 (4)	0.005 (5)	0.005 (5)
Ru-116	0.35 (2)	0.31 (3)	0.17 (3)	0.16 (2)	0.19 (3)	0.15 (3)
Rh-116	2.06 (5)	1.88 (7)	1.54 (9)	1.40 (6)	1.21 (8)	1.16 (8)
Pd-116	10.9 (1)	10.8 (2)	8.6 (2)	7.8 (1)	7.2 (2)	7.2 (2)
Ag-116	14.5 (1)	14.1 (2)	12.9 (3)	12.2 (2)	11.9 (3)	12.1 (3)
In-116	1.92 (5)	2.39 (8)	3.3 (1)	3.7 (1)	4.0 (1)	4.5 (2)
Pd-117	4.49 (7)	4.4 (1)	3.1 (1)	3.12 (9)	2.8 (1)	2.5 (1)
Ag-117	16.8 (1)	16.3 (2)	14.5 (3)	13.1 (2)	12.7 (3)	11.7 (2)
Cd-117	12.4 (1)	12.4 (2)	12.9 (3)	12.4 (2)	11.7 (2)	12.1 (3)
In-117	5.45 (8)	6.1 (1)	7.7 (2)	8.1 (1)	8.2 (2)	9.1 (2)
Sn-117	0.29 (2)	0.45 (3)	0.99 (7)	1.20 (6)	1.26 (8)	1.64 (9)
Sb-117	0.004 (2)	-	0.03 (1)	0.07 (1)	0.08 (2)	0.17 (3)
Ag-118	9.5 (1)	9.0 (1)	7.6 (2)	6.9 (1)	6.3 (2)	6.2 (2)
Cd-118	18.7 (2)	18.6 (2)	17.2 (3)	16.3 (2)	16.2 (3)	15.0 (3)
In-118	7.33 (9)	7.6 (1)	8.4 (2)	8.9 (2)	9.0 (2)	9.4 (2)
Sb-118	0.015 (4)	0.022 (7)	0.14 (3)	0.14 (2)	0.37 (4)	0.37 (4)
Ag-119	8.3 (1)	7.8 (1)	6.4 (2)	5.8 (1)	5.0 (2)	4.9 (2)
Cd-119	12.0 (1)	11.4 (2)	10.0 (2)	9.6 (2)	9.3 (2)	8.8 (2)
In-119	13.8 (1)	13.5 (2)	14.6 (3)	14.5 (2)	14.0 (3)	13.7 (3)
Sb-119	0.12 (1)	0.26 (3)	0.58 (6)	0.69 (4)	1.00 (7)	1.27 (8)
Te-119	0.001 (1)	-	0.016 (9)	0.005 (4)	0.07 (2)	0.06 (2)
Ag-120	4.12 (7)	3.68 (9)	3.0 (1)	2.51 (8)	2.4 (1)	2.2 (1)
Cd-120	14.7 (1)	13.8 (2)	11.7 (2)	10.6 (2)	9.4 (2)	9.1 (2)
In-120	12.2 (1)	12.0 (2)	11.5 (2)	11.2 (2)	10.7 (2)	10.4 (2)
Sb-120	0.42 (2)	0.54 (4)	1.09 (8)	1.31 (6)	1.7 (1)	1.9 (1)
In-121	16.4 (1)	15.4 (2)	14.3 (3)	13.4 (2)	12.7 (3)	12.7 (3)
Sn-121	7.8 (1)	8.0 (1)	8.5 (2)	8.2 (1)	8.2 (2)	8.8 (2)
Te-121	0.023 (5)	0.05 (1)	0.23 (3)	0.25 (3)	0.36 (4)	0.48 (5)
I-121	-	-	-	0.008 (5)	0.016 (9)	0.04 (1)
In-122	10.6 (2)	10.9 (2)	9.1 (2)	8.2 (2)	7.9 (1)	7.5 (2)
Sb-122	2.97 (8)	3.36 (9)	4.4 (2)	4.5 (2)	5.0 (1)	5.1 (2)
I-122	-	-	0.011 (7)	0.02 (1)	0.05 (1)	0.07 (2)

Table B.1 Continued.

Isotope	76.5 (8) MeV	89.9 (4) MeV	127.8 (5) MeV	152.5 (5) MeV	173.6 (5) MeV	192.1 (5) MeV
Xe-122	-	-	-	-	0.003 (3)	-
In-123	11.6 (2)	11.2 (2)	9.2 (2)	8.4 (2)	7.4 (1)	7.1 (2)
Sn-123	11.0 (2)	10.7 (2)	9.5 (2)	9.3 (2)	8.5 (1)	8.1 (2)
I-123	0.017 (6)	0.022 (7)	0.06 (2)	0.16 (3)	0.27 (3)	0.36 (4)
Xe-123	-	-	-	-	0.003 (3)	-
Cd-124	2.34 (8)	2.05 (7)	1.64 (9)	1.33 (8)	1.23 (6)	1.17 (8)
In-124	6.5 (1)	6.0 (1)	4.8 (2)	4.5 (2)	3.8 (1)	3.7 (1)
Sb-124	7.4 (1)	7.7 (1)	7.6 (2)	7.9 (2)	7.7 (1)	7.9 (2)
I-124	0.05 (1)	0.07 (1)	0.25 (4)	0.38 (4)	0.50 (4)	0.58 (6)
Cd-125	0.81 (4)	0.76 (4)	0.51 (5)	0.39 (5)	0.43 (3)	0.32 (4)
In-125	5.9 (1)	5.6 (1)	4.2 (1)	3.4 (1)	3.36 (9)	3.2 (1)
Sn-125	9.3 (1)	8.8 (1)	7.3 (2)	6.2 (2)	6.2 (1)	5.8 (2)
Sb-125	12.1 (2)	11.9 (2)	11.7 (2)	11.3 (2)	11.2 (2)	10.3 (2)
I-125	0.29 (3)	0.46 (3)	0.99 (7)	1.21 (8)	1.44 (6)	1.7 (1)
Xe-125	-	0.005 (3)	0.03 (1)	0.03 (1)	0.04 (1)	0.08 (2)
Ag-126	0.034 (9)	0.024 (8)	0.03 (1)	0.016 (9)	0.011 (5)	0.011 (7)
Cd-126	0.59 (4)	0.60 (4)	0.37 (4)	0.33 (4)	0.27 (3)	0.29 (4)
In-126	2.89 (8)	2.57 (8)	2.0 (1)	1.65 (9)	1.56 (6)	1.41 (9)
Sn-126	10.7 (2)	9.9 (2)	7.4 (2)	7.1 (2)	6.1 (1)	5.9 (2)
Sb-126	10.0 (2)	9.8 (2)	8.7 (2)	8.2 (2)	7.7 (1)	7.3 (2)
I-126	0.80 (4)	0.97 (5)	1.64 (9)	2.0 (1)	2.00 (7)	2.4 (1)
In-127	2.21 (7)	2.23 (7)	1.39 (9)	1.24 (8)	1.11 (5)	1.12 (8)
Sn-127	6.2 (1)	5.4 (1)	4.3 (1)	3.5 (1)	3.26 (9)	3.2 (1)
Sb-127	13.5 (2)	12.8 (2)	10.3 (2)	9.7 (2)	9.2 (2)	8.6 (2)
Te-127	7.4 (1)	7.1 (1)	7.0 (2)	7.0 (2)	6.8 (1)	6.8 (2)
Xe-127	0.08 (1)	0.07 (1)	0.24 (4)	0.27 (4)	0.35 (3)	0.49 (5)
Cs-127	-	-	0.005 (5)	0.011 (7)	0.04 (1)	0.04 (1)
In-128	1.01 (5)	0.78 (4)	0.60 (6)	0.57 (5)	0.39 (3)	0.42 (5)
Sn-128	6.1 (1)	5.3 (1)	3.9 (1)	3.4 (1)	3.15 (9)	3.0 (1)
Sb-128	9.5 (2)	8.9 (1)	7.1 (2)	6.0 (2)	5.8 (1)	5.2 (2)
I-128	3.32 (9)	3.67 (9)	4.2 (1)	4.6 (2)	4.8 (1)	5.2 (2)
Cs-128	-	0.007 (4)	0.02 (1)	0.05 (2)	0.08 (1)	0.11 (2)
Sn-129	2.78 (8)	2.54 (8)	1.8 (1)	1.52 (9)	1.38 (6)	1.31 (8)
Sb-129	11.4 (2)	10.0 (2)	7.9 (2)	6.9 (2)	6.3 (1)	5.7 (2)
Te-129	9.6 (2)	9.5 (2)	7.8 (2)	7.1 (2)	6.5 (1)	6.8 (2)
I-129	6.7 (1)	7.1 (1)	7.3 (2)	7.2 (2)	7.2 (1)	7.1 (2)
Cs-129	0.022 (7)	0.031 (9)	0.15 (3)	0.19 (3)	0.23 (2)	0.31 (4)
Ba-129	-	-	-	0.011 (7)	0.013 (6)	0.011 (7)
In-130	0.16 (2)	0.11 (2)	0.11 (2)	0.08 (2)	0.07 (1)	0.07 (2)
Sn-130	2.26 (7)	2.06 (7)	1.40 (9)	1.17 (8)	1.01 (5)	0.97 (7)
Sb-130	7.6 (1)	6.5 (1)	4.7 (2)	4.3 (1)	3.9 (1)	3.3 (1)
Te-130	14.1 (2)	12.9 (2)	10.4 (2)	9.0 (2)	8.7 (2)	7.7 (2)
I-130	6.9 (1)	6.8 (1)	6.4 (2)	6.3 (2)	6.4 (1)	6.5 (2)
Cs-130	0.08 (1)	0.15 (2)	0.41 (5)	0.48 (5)	0.58 (4)	0.62 (6)
Sb-131	7.0 (1)	6.4 (1)	4.3 (2)	3.6 (1)	3.5 (1)	3.0 (1)
Te-131	10.8 (2)	9.7 (2)	7.1 (2)	6.9 (2)	6.2 (1)	5.5 (2)

Table B.1 Continued.

Isotope	76.5 (8) MeV	89.9 (4) MeV	127.8 (5) MeV	152.5 (5) MeV	173.6 (5) MeV	192.1 (5) MeV
I-131	11.4 (2)	11.4 (2)	9.7 (2)	9.1 (2)	8.7 (2)	8.1 (2)
Cs-131	0.42 (3)	0.56 (4)	0.82 (7)	1.11 (8)	1.44 (6)	1.42 (9)
Ba-131	0.007 (4)	0.012 (5)	0.05 (2)	0.09 (2)	0.17 (2)	0.21 (3)
La-131	-	-	-	0.005 (5)	0.005 (4)	0.005 (5)
Sb-132	3.28 (9)	2.86 (8)	2.0 (1)	1.65 (9)	1.65 (7)	1.45 (9)
Te-132	13.2 (2)	12.1 (2)	8.9 (2)	7.7 (2)	6.9 (1)	6.4 (2)
I-132	10.7 (2)	10.1 (2)	8.2 (2)	7.6 (2)	7.1 (1)	6.8 (2)
Cs-132	0.95 (5)	1.14 (5)	1.50 (9)	1.54 (9)	1.72 (7)	1.68 (9)
La-132	-	-	-	0.011 (7)	0.016 (6)	0.011 (7)
Te-133	7.7 (1)	7.1 (1)	5.4 (2)	4.7 (2)	4.0 (1)	3.5 (1)
I-133	15.6 (2)	14.9 (2)	11.7 (2)	9.8 (5)	9.5 (2)	8.8 (2)
Xe-133	7.1 (1)	6.7 (1)	6.0 (2)	6.0 (2)	5.5 (1)	5.3 (2)
Ba-133	0.15 (2)	0.22 (2)	0.43 (5)	0.70 (6)	0.77 (5)	0.78 (6)
La-133	-	0.005 (3)	0.04 (1)	0.04 (1)	0.08 (1)	0.10 (2)
Ce-133	-	-	-	-	0.003 (3)	0.005 (5)
Te-134	6.5 (1)	5.5 (1)	3.9 (1)	3.2 (1)	3.16 (9)	2.8 (1)
I-134	13.3 (2)	12.1 (2)	8.9 (2)	7.7 (2)	7.1 (1)	6.4 (2)
Cs-134	3.37 (9)	3.42 (9)	3.2 (1)	3.2 (1)	3.20 (9)	3.1 (1)
La-134	0.015 (6)	0.015 (6)	0.07 (2)	0.19 (3)	0.15 (2)	0.27 (4)
Ce-134	-	-	-	0.005 (5)	0.003 (3)	0.03 (1)
I-135	14.0 (2)	12.3 (2)	9.3 (2)	8.0 (2)	7.4 (1)	6.5 (2)
Xe-135	12.9 (2)	11.7 (2)	9.3 (2)	8.5 (2)	7.5 (1)	6.8 (2)
Cs-135	6.2 (1)	6.2 (1)	5.4 (2)	5.6 (2)	5.3 (1)	5.3 (2)
La-135	0.05 (1)	0.09 (1)	0.25 (4)	0.44 (5)	0.42 (3)	0.62 (6)
Ce-135	-	-	0.005 (5)	0.02 (1)	0.013 (6)	0.03 (1)
I-136	5.3 (1)	4.8 (1)	3.3 (1)	2.7 (1)	2.73 (8)	2.7 (1)
Xe-136	17.3 (2)	16.0 (2)	11.6 (2)	10.6 (2)	9.8 (2)	8.9 (2)
Cs-136	7.9 (1)	7.5 (1)	6.2 (2)	6.0 (2)	5.4 (1)	5.7 (2)
La-136	0.22 (2)	0.28 (3)	0.53 (5)	0.46 (5)	0.66 (4)	0.68 (6)
Ce-136	0.002 (2)	0.002 (2)	0.08 (2)	0.11 (2)	0.08 (1)	0.18 (3)
Pr-136	-	-	-	-	0.003 (3)	0.005 (5)
I-137	4.3 (1)	3.9 (1)	2.8 (1)	2.4 (1)	2.18 (8)	1.9 (1)
Xe-137	8.9 (1)	8.3 (1)	5.9 (2)	5.1 (2)	4.7 (1)	4.2 (1)
Cs-137	13.5 (2)	12.8 (2)	10.0 (2)	8.9 (2)	8.5 (1)	7.9 (2)
La-137	0.69 (4)	0.84 (5)	1.12 (8)	1.33 (8)	1.24 (6)	1.43 (9)
Ce-137	0.012 (5)	0.019 (7)	0.11 (2)	0.18 (3)	0.22 (2)	0.26 (4)
Pr-137	-	-	-	0.005 (5)	0.016 (6)	0.005 (5)
Xe-138	9.5 (2)	8.7 (1)	5.9 (2)	5.4 (2)	4.9 (1)	4.5 (2)
Cs-138	9.4 (2)	8.8 (1)	6.8 (2)	5.6 (2)	5.4 (1)	5.1 (2)
La-138	1.24 (5)	1.37 (6)	1.49 (9)	1.43 (9)	1.51 (6)	1.48 (9)
Pr-138	0.002 (2)	-	0.016 (9)	-	0.013 (6)	0.03 (1)
Xe-139	4.5 (1)	4 (1)	2.9 (1)	2.3 (1)	2.28 (8)	2.1 (1)
Cs-139	12.2 (2)	10.9 (2)	7.7 (2)	7.4 (2)	6.7 (1)	5.9 (2)
Ba-139	6.2 (1)	5.9 (1)	4.5 (2)	4.2 (1)	4.2 (1)	3.8 (1)
Ce-139	0.31 (3)	0.30 (3)	0.52 (5)	0.63 (6)	0.66 (4)	0.68 (6)
Pr-139	0.002 (2)	0.017 (6)	0.06 (2)	0.09 (2)	0.04 (1)	0.12 (3)

Isotope	76.5 (8) MeV	89.9 (4) MeV	127.8 (5) MeV	152.5 (5) MeV	173.6 (5) MeV	192.1 (5) MeV
Nd-139	-	-	-	-	0.008 (5)	-
I-140	0.39 (3)	0.32 (3)	0.19 (3)	0.21 (3)	0.19 (2)	0.18 (3)
Xe-140	3.70 (9)	3.28 (9)	2.5 (1)	2.3 (1)	1.85 (7)	1.60 (9)
Cs-140	8.1 (1)	7.9 (1)	5.7 (2)	5.0 (2)	4.5 (1)	4.3 (2)
Ba-140	9.4 (2)	8.9 (1)	7.5 (2)	6.3 (2)	6.2 (1)	5.4 (2)
La-140	2.55 (8)	2.48 (8)	2.1 (1)	2.3 (1)	2.16 (8)	2.1 (1)
Nd-140	-	-	0.005 (5)	0.016 (9)	0.021 (7)	0.05 (2)
Cs-141	7.6 (1)	6.9 (1)	5.2 (2)	4.2 (1)	4.1 (1)	3.7 (1)
Ba-141	8.0 (1)	7.2 (1)	5.2 (2)	4.8 (2)	4.5 (1)	4.3 (2)
La-141	4.6 (1)	4.3 (1)	3.8 (1)	3.3 (1)	3.39 (9)	3.2 (1)
Ce-141	0.91 (5)	0.87 (5)	0.96 (7)	1.09 (8)	0.95 (5)	1.03 (7)
Nd-141	-	0.002 (2)	0.005 (5)	0.05 (2)	0.07 (1)	0.05 (2)
Pm-141	-	-	-	-	0.003 (3)	0.005 (5)
Cs-142	4.1 (1)	3.67 (7)	2.61 (8)	2.5 (1)	2.1 (1)	2.0 (1)
Ba-142	9.4 (2)	8.7 (1)	6.5 (1)	5.8 (2)	5.4 (2)	4.9 (2)
La-142	4.8 (1)	4.48 (7)	3.6 (1)	3.4 (1)	3.2 (1)	2.9 (1)
Pr-142	0.21 (2)	0.29 (2)	0.37 (3)	0.40 (5)	0.38 (4)	0.45 (5)
Cs-143	2.93 (8)	2.76 (6)	2.03 (7)	1.51 (9)	1.51 (9)	1.45 (9)
Ba-143	5.7 (1)	5.24 (8)	3.8 (1)	3.3 (1)	3.1 (1)	2.8 (1)
La-143	6.8 (1)	6.57 (9)	5.0 (1)	4.6 (2)	4.2 (1)	4.0 (1)
Ce-143	1.95 (7)	1.86 (5)	1.59 (6)	1.58 (9)	1.49 (9)	1.46 (9)
Pr-143	0.51 (4)	0.58 (3)	0.60 (4)	0.68 (6)	0.47 (5)	0.61 (6)
Pm-143	-	-	0.008 (5)	0.005 (5)	0.016 (9)	0.04 (1)
Cs-144	1.24 (5)	1.11 (4)	0.76 (4)	0.71 (6)	0.58 (6)	0.58 (6)
Ba-144	5.3 (1)	4.97 (8)	3.5 (1)	3.0 (1)	2.8 (1)	2.6 (1)
La-144	5.7 (1)	5.23 (8)	4.0 (1)	3.6 (1)	3.2 (1)	3.1 (1)
Ce-144	3.16 (9)	3.15 (6)	2.73 (8)	2.6 (1)	2.5 (1)	2.2 (1)
Pr-144	0.62 (4)	0.62 (3)	0.69 (4)	0.72 (6)	0.50 (5)	0.66 (6)
Nd-144	0.15 (2)	0.15 (1)	0.20 (2)	0.31 (4)	0.25 (4)	0.28 (4)
La-145	6.4 (1)	5.84 (8)	4.4 (1)	3.9 (1)	3.8 (1)	3.3 (1)
Ce-145	2.94 (8)	2.82 (6)	2.36 (8)	2.2 (1)	2.0 (1)	2.0 (1)
Pr-145	1.13 (5)	1.07 (4)	0.99 (5)	1.04 (7)	1.04 (7)	0.98 (7)
Pm-145	0.010 (5)	0.019 (5)	0.05 (1)	0.11 (2)	0.09 (2)	0.11 (2)
Sm-145	-	-	-	0.005 (5)	0.005 (5)	0.02 (1)
Ce-146	4.4 (1)	4.31 (7)	3.36 (9)	3.1 (1)	3.0 (1)	2.9 (1)
Pr-146	1.15 (5)	1.13 (4)	1.01 (5)	0.88 (7)	0.83 (7)	0.94 (7)
Pm-146	0.017 (6)	0.037 (7)	0.07 (1)	0.11 (2)	0.11 (2)	0.10 (2)
Sm-146	-	-	0.011 (5)	0.011 (7)	0.03 (1)	0.03 (1)
Pr-147	1.85 (7)	1.80 (5)	1.53 (6)	1.50 (9)	1.57 (9)	1.50 (9)
Nd-147	0.34 (3)	0.39 (2)	0.39 (3)	0.40 (5)	0.36 (4)	0.35 (4)
Pm-147	0.06 (1)	0.09 (1)	0.13 (2)	0.19 (3)	0.20 (3)	0.16 (3)
Sm-147	0.005 (3)	0.002 (2)	0.024 (8)	0.03 (1)	0.03 (1)	0.03 (1)
Eu-147	-	-	-	-	0.005 (5)	0.005 (5)
Pr-148	1.79 (7)	1.69 (5)	1.44 (6)	1.29 (8)	1.21 (8)	1.13 (8)
Pm-148	0.10 (2)	0.12 (1)	0.16 (2)	0.18 (3)	0.24 (4)	0.16 (3)
Sm-148	0.007 (4)	0.007 (3)	0.06 (1)	0.06 (2)	0.11 (2)	0.07 (2)

Table B.1 Continued.

Isotope	76.5 (8) MeV	89.9 (4) MeV	127.8 (5) MeV	152.5 (5) MeV	173.6 (5) MeV	192.1 (5) MeV
Eu-148	-	-	0.003 (3)	0.005 (5)	0.005 (5)	0.005 (5)
Pr-149	2.44 (8)	2.37 (5)	1.80 (7)	1.8 (1)	1.8 (1)	1.61 (9)
Nd-149	0.61 (4)	0.56 (3)	0.61 (4)	0.54 (5)	0.57 (5)	0.48 (5)
Pm-149	0.21 (2)	0.19 (2)	0.25 (3)	0.24 (4)	0.23 (3)	0.27 (4)
Eu-149	-	-	0.005 (4)	0.011 (7)	0.02 (1)	0.011 (7)
Ce-150	1.71 (6)	1.56 (4)	1.19 (6)	0.92 (7)	1.00 (7)	0.80 (6)
Pr-150	1.83 (7)	1.63 (4)	1.33 (6)	1.13 (8)	1.12 (8)	1.01 (7)
Nd-150	1.15 (5)	1.05 (4)	0.95 (5)	0.97 (7)	0.72 (6)	0.67 (6)
Pm-150	0.18 (2)	0.21 (2)	0.22 (2)	0.18 (3)	0.22 (3)	0.23 (3)
Eu-150	-	0.004 (2)	0.003 (3)	0.03 (1)	0.03 (1)	0.03 (1)
Gd-150	-	-	0.003 (3)	-	-	-
Pr-151	1.89 (7)	1.86 (5)	1.36 (6)	1.26 (8)	1.12 (8)	1.07 (8)
Nd-151	0.98 (5)	0.91 (3)	0.67 (4)	0.65 (6)	0.62 (6)	0.67 (6)
Pm-151	0.30 (3)	0.38 (2)	0.35 (3)	0.28 (4)	0.33 (4)	0.31 (4)
Sm-151	0.04 (1)	0.064 (9)	0.12 (2)	0.11 (2)	0.09 (2)	0.10 (2)
Gd-151	-	-	0.003 (3)	0.005 (5)	-	-
Nd-152	1.27 (6)	1.17 (4)	1.05 (5)	0.78 (6)	0.97 (7)	0.82 (7)
Pm-152	0.34 (3)	0.33 (2)	0.33 (3)	0.23 (3)	0.21 (3)	0.36 (4)
Eu-152	0.010 (5)	0.015 (4)	0.034 (9)	0.04 (1)	0.05 (2)	0.03 (1)
Gd-152	-	-	-	0.011 (7)	0.02 (1)	0.016 (9)
Nd-153	0.79 (4)	0.76 (3)	0.61 (4)	0.49 (5)	0.61 (6)	0.42 (5)
Pm-153	0.57 (4)	0.55 (3)	0.36 (3)	0.43 (5)	0.40 (5)	0.45 (5)
Sm-153	0.11 (2)	0.12 (1)	0.13 (2)	0.11 (2)	0.14 (3)	0.13 (3)
Gd-153	-	0.002 (2)	0.003 (3)	0.005 (5)	0.011 (7)	0.03 (1)
Tb-153	-	-	-	-	-	0.005 (5)
Nd-154	0.67 (4)	0.63 (3)	0.48 (4)	0.43 (5)	0.37 (4)	0.36 (4)
Pm-154	0.47 (3)	0.43 (2)	0.38 (3)	0.33 (4)	0.32 (4)	0.28 (4)
Eu-154	0.031 (9)	0.045 (7)	0.06 (1)	0.04 (1)	0.07 (2)	0.05 (2)
Tb-154	-	-	0.003 (3)	0.005 (5)	0.005 (5)	-
Pm-155	0.42 (3)	0.42 (2)	0.40 (3)	0.30 (4)	0.35 (4)	0.27 (4)
Sm-155	0.14 (2)	0.15 (1)	0.16 (2)	0.11 (2)	0.09 (2)	0.17 (3)
Eu-155	0.06 (1)	0.073 (9)	0.08 (1)	0.06 (2)	0.06 (2)	0.05 (2)
Tb-155	-	-	-	0.016 (9)	-	0.011 (7)
Nd-156	0.20 (2)	0.16 (1)	0.19 (2)	0.12 (3)	0.08 (2)	0.11 (2)
Pm-156	0.29 (3)	0.26 (2)	0.21 (2)	0.15 (3)	0.17 (3)	0.15 (3)
Sm-156	0.20 (2)	0.19 (1)	0.17 (2)	0.14 (3)	0.16 (3)	0.20 (3)
Eu-156	0.04 (1)	0.050 (8)	0.07 (1)	0.04 (1)	0.07 (2)	0.02 (1)
Tb-156	-	0.001 (1)	0.003 (3)	-	0.005 (5)	0.005 (5)
Pm-157	0.23 (2)	0.21 (2)	0.17 (2)	0.09 (2)	0.11 (2)	0.15 (3)
Sm-157	0.15 (2)	0.15 (1)	0.12 (2)	0.14 (3)	0.14 (3)	0.09 (2)
Eu-157	0.08 (1)	0.08 (1)	0.04 (1)	0.06 (2)	0.07 (2)	0.08 (2)
Tb-157	0.002 (2)	0.002 (2)	0.011 (5)	0.03 (1)	-	0.03 (1)
Nd-158	0.024 (8)	0.021 (5)	0.024 (8)	0.016 (9)	0.02 (1)	0.02 (1)
Pm-158	0.10 (2)	0.09 (1)	0.05 (1)	0.05 (2)	0.06 (2)	0.04 (1)
Sm-158	0.13 (2)	0.14 (1)	0.12 (2)	0.13 (3)	0.05 (2)	0.11 (2)
Eu-158	0.09 (1)	0.062 (9)	0.05 (1)	0.04 (1)	0.04 (1)	0.04 (1)

Table B.1 Continued.

Isotope	76.5 (8) MeV	89.9 (4) MeV	127.8 (5) MeV	152.5 (5) MeV	173.6 (5) MeV	192.1 (5) MeV
Tb-158	0.010 (5)	0.002 (2)	0.021 (7)	0.005 (5)	0.02 (1)	0.005 (5)
Sm-159	0.09 (1)	0.08 (1)	0.06 (1)	0.07 (2)	0.04 (1)	0.02 (1)
Eu-159	0.11 (2)	0.08 (1)	0.06 (1)	0.07 (2)	0.05 (2)	0.03 (1)
Gd-159	0.022 (7)	0.013 (4)	0.018 (7)	0.02 (1)	0.04 (1)	0.03 (1)
Dy-159	-	-	0.005 (4)	-	0.011 (7)	0.005 (5)
Sm-160	0.05 (1)	0.044 (7)	0.032 (9)	0.02 (1)	0.03 (1)	0.011 (7)
Eu-160	0.04 (1)	0.040 (7)	0.04 (1)	0.02 (1)	0.016 (9)	0.03 (1)
Tb-160	0.005 (3)	0.011 (4)	0.011 (5)	0.03 (1)	0.03 (1)	0.011 (7)
Ho-160	-	-	-	-	-	0.005 (5)
Eu-161	0.022 (7)	0.035 (7)	0.018 (7)	0.02 (1)	0.03 (1)	0.04 (1)
Gd-161	0.031 (9)	0.017 (5)	0.008 (5)	0.016 (9)	0.005 (5)	0.02 (1)
Tb-161	0.019 (7)	0.016 (4)	0.016 (6)	0.016 (9)	0.04 (1)	0.005 (5)
Ho-161	-	-	-	-	-	0.005 (5)
Eu-162	0.010 (5)	0.018 (5)	0.008 (5)	0.013 (6)	0.005 (5)	0.011 (7)
Gd-162	0.022 (7)	0.019 (5)	0.018 (7)	0.013 (6)	0.005 (5)	-
Tb-162	0.024 (8)	0.018 (5)	0.018 (7)	0.008 (5)	-	0.005 (5)
Ho-162	-	-	-	0.003 (3)	0.011 (7)	-
Gd-163	0.002 (2)	0.007 (3)	0.008 (5)	0.005 (4)	0.005 (5)	-
Tb-163	0.012 (5)	0.011 (4)	0.011 (5)	0.011 (5)	0.011 (7)	0.011 (7)
Ho-163	-	-	-	0.003 (3)	0.005 (5)	0.005 (5)
Gd-164	0.010 (5)	0.005 (2)	0.013 (6)	0.005 (4)	-	-
Tb-164	0.005 (3)	0.005 (2)	0.003 (3)	0.005 (4)	0.005 (5)	0.011 (7)
Ho-164	-	0.006 (3)	0.008 (5)	0.008 (5)	0.005 (5)	-
Gd-165	-	0.002 (2)	0.005 (4)	-	-	-
Tb-165	0.002 (2)	0.004 (2)	0.003 (3)	0.003 (3)	0.005 (5)	-
Dy-165	0.002 (2)	0.001 (1)	0.003 (3)	0.003 (3)	0.005 (5)	-
Er-165	-	-	0.003 (3)	0.003 (3)	0.011 (7)	-
Tb-166	0.002 (2)	0.001 (1)	0.003 (3)	0.003 (3)	-	0.005 (5)
Dy-166	0.005 (3)	0.004 (2)	0.008 (5)	0.003 (3)	0.02 (1)	0.005 (5)
Ho-166	0.005 (3)	0.001 (1)	0.005 (4)	-	0.011 (7)	0.005 (5)
Tm-166	-	-	-	0.003 (3)	-	0.005 (5)
Tb-167	-	0.004 (2)	0.008 (5)	-	-	-
Dy-167	0.002 (2)	0.001 (1)	-	0.005 (4)	0.005 (5)	0.005 (5)
Ho-167	-	0.001 (1)	0.005 (4)	-	0.005 (5)	0.005 (5)
Tm-167	-	-	-	0.003 (3)	-	-
Tb-168	-	0.001 (1)	-	-	-	-
Dy-168	-	-	-	-	-	0.005 (5)
Ho-168	0.002 (2)	0.002 (2)	-	0.005 (4)	-	-
Ra-222	0.53 (4)	2.13 (5)	4.7 (1)	6.3 (1)	7.6 (2)	8.6 (2)
Ra-223	0.87 (5)	2.09 (5)	3.6 (1)	4.9 (1)	5.9 (2)	6.4 (2)
Ra-224	1.77 (7)	2.43 (5)	4.1 (1)	5.6 (1)	6.4 (2)	7.1 (2)
Ac-224	7.5 (1)	8 (1)	20.8 (2)	23.5 (2)	24.1 (4)	24.1 (4)
Ra-225	1.21 (5)	1.37 (4)	2.76 (9)	3.7 (1)	4.1 (1)	4.9 (2)
Ac-225	7.8 (1)	11.8 (1)	26.0 (3)	28.4 (3)	28.2 (4)	28.2 (4)
Th-225	5.4 (1)	5.72 (8)	5.2 (1)	4.6 (1)	4.2 (1)	3.5 (1)
Ra-226	1.05 (5)	1.18 (4)	2.86 (9)	3.9 (1)	4.7 (2)	4.8 (2)

Isotope	76.5 (8) MeV	89.9 (4) MeV	127.8 (5) MeV	152.5 (5) MeV	173.6 (5) MeV	192.1 (5) MeV
Ac-226	7.4 (1)	12.6 (1)	21.8 (2)	23.0 (2)	22.8 (3)	22.9 (3)
Th-226	24.7 (2)	21.2 (2)	17.8 (2)	15.3 (2)	14.2 (3)	13.1 (3)
Ra-227	0.34 (3)	0.47 (2)	1.58 (6)	2.24 (8)	2.7 (1)	2.9 (1)
Ac-227	12.2 (2)	17.1 (1)	25.6 (3)	26.2 (3)	26.3 (4)	25.3 (4)
Th-227	37.6 (3)	31.5 (2)	25.6 (3)	22.1 (2)	19.6 (3)	18.1 (3)
Ac-228	12.2 (2)	14.8 (1)	19.3 (2)	19.3 (2)	19.2 (3)	18.5 (3)
Th-228	80.3 (4)	65.9 (3)	51.9 (4)	44.7 (3)	39.8 (5)	37.2 (4)
Pa-228	9.3 (1)	6.97 (9)	4.6 (1)	3.8 (1)	3.2 (1)	3.0 (1)
Ac-229	16.6 (2)	18.2 (1)	22.0 (2)	21.5 (2)	21.4 (3)	21.2 (3)
Th-229	81.7 (4)	66.8 (3)	51.9 (4)	45.0 (3)	40.9 (5)	38.0 (4)
Pa-229	24.0 (2)	17.8 (1)	11.7 (2)	9.1 (2)	7.9 (2)	6.9 (2)
Th-230	135.5 (6)	111.7 (4)	89.0 (5)	78.6 (5)	72.4 (6)	67.9 (6)
Pa-230	33.3 (3)	25.2 (2)	16.4 (2)	12.7 (2)	11.2 (2)	10.1 (2)
Th-231	170.1 (6)	143.4 (4)	122.3 (6)	111.1 (5)	105.1 (7)	100.5 (7)
Pa-231	43.1 (3)	32.3 (2)	21.3 (2)	16.8 (2)	15.0 (3)	13.1 (3)
Pa-232	14.9 (2)	10.6 (1)	6.7 (1)	5.8 (1)	4.9 (2)	4.2 (1)
Th-233	3.34 (9)	2.87 (6)	1.06 (5)	1.12 (5)	0.98 (7)	1.22 (8)
Pa-233	0.010 (5)	0.010 (3)	-	0.013 (6)	0.005 (5)	0.005 (5)

Appendix C: Example Efficiency Curve

A typical efficiency calibration is shown in Figure C.1. The points are experimentally measured efficiencies and a solid curve was generated via a 5th order polynomial function. The function of the curve is provided, and the constants for this specific efficiency curve are shown in Table C.1. It is important to note that the efficiency measured is the absolute efficiency. The absolute efficiency takes into account intrinsic peak efficiency as well as geometric efficiency.
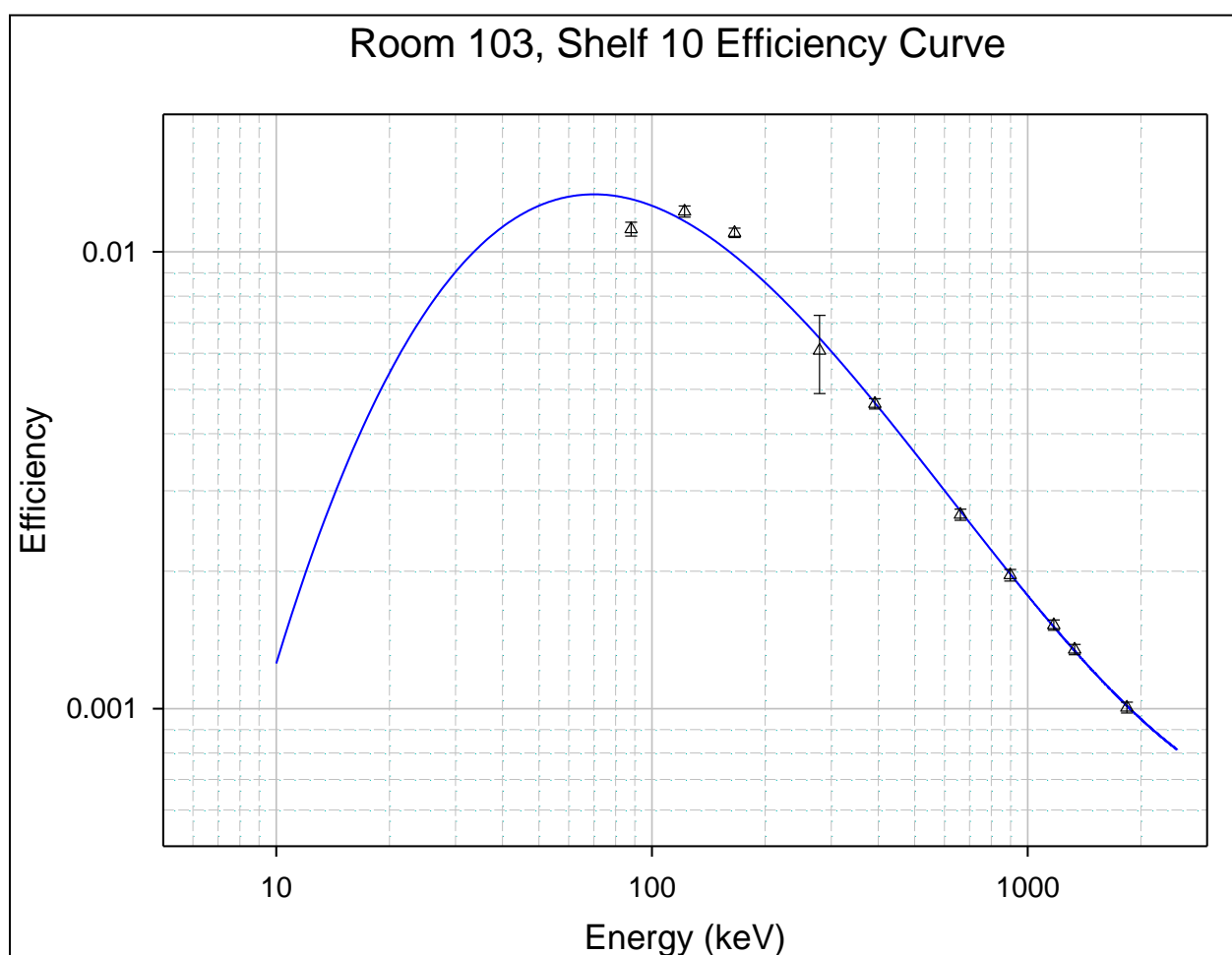

Figure C.1. Typical efficiency curve for HPGe detector used in this work.

$$efficiency = exp[a + b * ln(E) + c * ln(E)^2 + d * ln(E)^3] \quad \textit{Equation C.1}$$

Table C.1. Constants used in efficiency function. E is the incident photon energy.

a	B	c	d
-18.63	8.059	-1.415	0.073

Vita

Justin Griswold was born in Knoxville, Tennessee in 1990. He graduated from Farragut High School in Knoxville in 2008. He then attended the University of Tennessee and received his Bachelor of Science in Nuclear Engineering in 2012. He continued his education at the University of Tennessee where he received his Master of Science in Nuclear Engineering in May 2014. This dissertation completed the requirements for his Doctor of Philosophy in Nuclear Engineering. He began working as an undergraduate research assistant at Oak Ridge National Laboratory in 2010, where his research interests include isotope production, ion exchange chromatography, and gamma-ray spectroscopy.